Aus der neurologischen Klinik und Poliklinik
Klinikum der Ludwig-Maximilians-Universität München
Direktorin: Univ. Prof. Dr. med. Marianne Dieterich

Analysis of Pain Intensity Encoding in Chronic Pain Patients using Functional Magnetic Resonance Imaging

Analyse der Schmerzintensitätskodierung bei chronischen Schmerzpatienten mit funktioneller Magnetresonanztomographie

Dissertation
zum Erwerb des Doktorgrades der Naturwissenschaften
an der Medizinischen Fakultät der
Ludwig-Maximilians-Universität München

Astrid Mayr
2021

Mit Genehmigung der Medizinischen Fakultät
der Ludwig-Maximilians-Universität München

Betreuer: Prof. Dr. rer. nat. Olaf Dietrich

Zweitgutachter: Prof. Dr. Guillaume Landry

Dekan: Prof. Dr. med. Thomas Gudermann

Tag der mündlichen Prüfung: 02.05.2022

Publications

During the three years of this thesis, the following manuscripts have been created:

- **Mayr, A.** and Jahn, P., Stankewitz, A., Deak, B., Winkler, A., and Witkovsky, V., Eren, O., Straube, A. and Schulz, E. (2020). "Chronic Pain Patients Exhibit Individually Unique Cortical Signatures of Pain" *bioRxiv: https://doi.org/10.1101/2020.09.05.284117. Manuscript submitted and under review.*

- **Mayr, A.**, Jahn, P., Deak, B., Stankewitz, A., Devulapally, V., Witkovsky, V., Dietrich, O. and Schulz, E. (2021). "Individual cortical connectivity patterns in chronic pain patients using fMRI." *osf.io: https://doi.org/10.1101/2021.06.30.450553. Manuscript submitted, preprint available online.*

- Jahn, P., and Deak, B., **Mayr, A.**, Stankewitz, A., Keeser, D., Griffanti, L., Witkovsky, V., Irving, S. and Schulz, E. (2021). "Intrinsic Network Activity Reflects the Ongoing Experience of Chronic Pain" *bioRxiv: https://doi.org/10.1101/2021.06.30.450604. Manuscript submitted, preprint available online.*

- Deak, B., and Eggert, T., **Mayr, A.**, Stankewitz, A., Filippopulos, F., Jahn, P., Witkovsky, V., Straube, A. and Schulz, E. (2021). "Intrinsic Network Activity Reflects the Fluctuating Experience of Tonic Pain" *bioRxiv: https://doi.org/10.1101/2021.06.30.450591. Manuscript submitted, preprint available online.*

- **Mayr, A.**, Stankewitz, A., Irving, S., Witkovsky, V. and Schulz, E. (2021). "Pain and the Emotional Brain: Affective Rather than Cognitive Processes Drive the Cortical Encoding of Pain" *bioRxiv: https://doi.org/10.1101/2021.06.30.450586. Manuscript submitted, preprint available online.*

Contents

1 Abstract

Chronic pain diseases are characterized by a persistent, ongoing and fluctuating endogenous pain experience with different levels of pain intensity. However, it still remains to be elucidated how pain intensity and the dynamics of pain including rising as well as falling pain levels are encoded in the brain of chronic pain patients. Additionally, the corresponding dynamics of functional cortical connections have not yet been clarified and lack reliable investigations across different chronic pain cohorts.

This thesis addresses this shortage by considering and analyzing the continuous oscillating pain experience in two different pain cohorts of chronic back pain (CBP) and chronic migraine (CM) patients. In four repeated functional magnetic resonance imaging (fMRI) sessions of 25 minutes patients were asked to continuously rate the intensity of their endogenous pain without external stimuli. Particular focus included investigations of the group as well as of the individual experience of pain patients. In three different analysis approaches, blood-oxygen-level-dependent (BOLD) activations in brain areas, their dynamic functional co-activations over time, as well as the stability of the patients' pain indications were investigated to evaluate the relationship between brain activity and the amplitude of chronic pain patients' endogenous pain.

In a first step, a voxelwise blood-oxygen-level-dependent signal analysis identified clusters of voxels which showed increased or decreased brain activation upon high and low pain states as well as rising or falling pain intensity. A sliding-window approach was applied which shifted the pain rating data against the cortical data to account for timing differences in brain activations. Voxel-wise linear mixed effects (LME) models were used to disentangle cortical processes related to pain intensity, pain intensity changes, as well as pure motor activity.

In a second approach, the functional dynamics of the brain activity were investigated based on the acquired fMRI and pain data. Parcellation of the brain subdivided the whole brain into 408 regions, followed by a principal component analysis (PCA), from which the first principal component (PC) was extracted. A ten second sliding-window connectivity analysis computed the pair-wise and time-varying co-activation (functional connectivity (FC)) between all brain regions across the entire recording period of 25 minutes. Linear mixed effects models were fitted for each pair of connected brain regions to explore the relationship between cortical connectivity and the indicated time course of the patients' fluctuating endogenous pain. Functional connectivity between two brain regions and the pain rating was evaluated based on a connectivity scheme which focused on mostly positive or negative connections.

The third step aimed at assessing the stability of the pain ratings of the patients both within and between fMRI sessions based on a supervised machine learning approach. A linear regression and XGBoost model were investigated to predict a constant relationship between brain activity based on all parcellated regions and pain intensity level. Stability of the relationship was investigated by cross-validation schemes using within- and between-session data i.e. if

the relationship learned in one fMRI session can be used to predict brain activity in a different session. Both between- and within-session approaches were pursued on a group and single subject-level separately leading to four different analysed settings. Performance of both models were compared to a featureless model and evaluated based on the absolute performance metric of the root mean squared error (RMSE) and the squared correlation coefficient R^2 as a relative measure.

In the first approach, at group-level, the intensity of pain in chronic back pain patients is mainly encoded in the anterior insular cortex, the frontal operculum, and the pons; the change of pain in chronic back pain and chronic migraine patients is mainly encoded in the anterior insular cortex. At the individual level, a more complex picture was identified, where each patient exhibited their own signature of endogenous pain encoding.

Connectivity analysis revealed that periods of high pain as well as increasing pain were predominantly related to low cortical connectivity. For the chronic back pain cohort this applies to the pain intensity-related connectivity for limbic and cingulate areas, and for the precuneus. The change of pain intensity was encoded by connections in left parietal opercular regions, right insular regions, as well as large parts of the parietal, cingular and motor cortices. The change of pain intensity direction in chronic migraine was reflected by decreasing connectivity between the anterior insular cortex and orbitofrontal areas, as well as between the posterior cingulate cortex (PCC) and frontal and anterior cingulate cortex (ACC) regions. Positive and negative relationships between pain perception correlated brain regions were revealed, but no effect for anticorrelated (i.e. suppressing) brain regions was found.

Overall, in the third analysis step, the supervised machine learning models were not able to predict the pain intensity based on the BOLD brain activity. Performance estimates were poor for all four pursued variants for chronic back pain patients and chronic migraineurs, but especially in CM patients. Still, the within-session approach achieved greater accuracy than the between-session approach, and learning on single subject-level revealed better results than learning on group-level for CBP patients. The maximum of $R^2 = 0.46$ was obtained in the subject-level within-session setting in the CBP cohort.

This is the first investigation of a sliding-window whole-brain BOLD and dynamic functional connectivity approach with a continuous, stimuli-free pain rating fMRI paradigm both in CBP and CM patient cohorts. With this more naturalistic fMRI design greater real-world relevance is achieved enabled through methodological advances including the combination of a non-binarised pain intensity rating, a sliding-window approach to resolve the unknown dynamics of the functional connections, a dynamic functional connectivity analysis, linear mixed-effects models and a correction for multiple comparisons with surrogate data. Additionally, special attention was given to the implementation of the continous pain-level rating of the subjects as well as on repeated and extended fMRI acquisitions for robust analysis.

The observed diversity of the individual cortical signatures of chronic pain encoding results bridges between clinical observations and neuroimaging: Clinicians often encounter patients with a unique composition of characteristics, personality traits, various combinations of symptoms, and therefore a wide range of individual responses to treatment. Machine learning approaches to predict pain intensity levels solely based on BOLD activations cannot replace

patients' indications yet, but improved solutions may be introduced in the clinical setting in the future in a complementary way. The obtained cortical signatures of chronic pain encoding add to the understanding of chronic pain as a complex and multifaceted disease supporting recent developments for a more personalized medicine.

2 Zusammenfassung

Chronische Schmerzerkrankungen sind durch ein anhaltendes, kontinuierliches und fluktuierendes endogenes Schmerzerleben mit unterschiedlicher Schmerzintensität gekennzeichnet. Wie die Schmerzintensität und die Dynamik des Schmerzes, einschließlich steigender und fallender Schmerzwerte, im Gehirn chronischer Schmerzpatienten verarbeitet werden, ist jedoch noch nicht geklärt. Darüber hinaus ist der zeitliche Zusammenhang zwischen der Aktivität zweier verschiedener Hirnareale während des Schmerzerlebens in chronischen Schmerzpatienten unzureichend erforscht und es fehlt an zuverlässigen Studienergebnissen in verschiedenen chronischen Schmerzkohorten.

Die vorliegende Arbeit adressiert diesen Mangel, indem sie das kontinuierlich oszillierende Schmerzerleben in zwei verschiedenen Schmerzkohorten in wiederholten funktionellen Magnetresonanztomographie (fMRT)-Messungen von 25 Minuten Dauer betrachtet und analysiert. Während vier fMRT-Sitzungen wurden 20 Patienten mit chronischen Rückenschmerzen (CBP) und 20 Patienten mit chronischer Migräne (CM) gebeten, die Intensität ihrer endogenen Schmerzen ohne die Einwirkung äußerer Reize kontinuierlich zu bewerten. Ein besonderer Fokus lag dabei auf der Untersuchung der Gruppen- sowie der individuellen Perspektive von Schmerzpatienten. In drei verschiedenen Analyseansätzen wurden BOLD-Aktivierungen ('blood oxygenation level dependent', also abhängig vom Blutsauerstoffgehalt) in Hirnarealen, deren dynamische funktionelle Koaktivierungen, sowie die Stabilität der Schmerzangaben der Patienten untersucht, um den Zusammenhang zwischen Hirnaktivität und der Amplitude des endogenen Schmerzes chronischer Schmerzpatienten zu erforschen.

In einem ersten Schritt wurden in fMRT-Aufnahmen mit BOLD-Kontrast Voxelcluster identifiziert, die bei hohen und niedrigen Schmerzzuständen sowie bei steigender oder fallender Schmerzintensität eine erhöhte oder verringerte neuronale Aktivität aufwiesen. Es wurde ein 'Schiebefenster'-Verfahren ('Sliding-Window') angewandt, bei dem die Daten zur Schmerzbewertung gegen die kortikalen Daten verschoben wurden, um zeitliche Unterschiede in den Hirnaktivierungen zu berücksichtigen. Voxelweise Modelle mit linearen gemischten Effekten wurden verwendet, um kortikale Prozesse im Zusammenhang mit der Schmerzintensität, Änderungen der Schmerzintensität und reiner motorischer Aktivität zu identifizieren.

In einem zweiten Ansatz wurde die funktionelle Dynamik der Hirnaktivität zwischen verschiedenen Hirnregionen auf der Grundlage der gewonnenen fMRT- und Schmerzdaten untersucht. Durch Parzellierung des Gehirns wurde das gesamte Gehirn in 408 Regionen unterteilt, gefolgt von einer Hauptkomponentenanalyse, aus der die erste Hauptkomponente extrahiert wurde. Eine 'Sliding-Window'-Konnektivitätsanalyse mit zehnsekündigen Schiebefenstern berechnete die paarweise und zeitlich variierende Koaktivierung zwischen allen Hirnregionen über die gesamte Aufzeichnungszeit von 25 Minuten. Lineare Modelle mit gemischten Effekten wurden für jedes Paar verbundener Hirnregionen angepasst, um die Beziehung zwischen kortikaler Konnektivität und dem angegebenen zeitlichen Verlauf der fluktuierenden endogenen Schmerzen der Patienten zu untersuchen. Die funktionelle Konnektivität zwischen zwei Hirnregionen und

der Schmerzbewertung wurde anhand eines Konnektivitätsschemas bewertet, welches sich auf überwiegend positive oder negative Verbindungen konzentrierte.

Der dritte Schritt zielte darauf ab, die Stabilität der Schmerzbewertungen der Patienten sowohl innerhalb als auch zwischen fMRT-Sitzungen auf der Grundlage eines überwachten maschinellen Lernansatzes zu bewerten. Es wurden ein lineares Regressions- und ein XGBoost-Modell untersucht, um eine konstante Beziehung zwischen der Gehirnaktivität auf der Grundlage aller parzellierten Regionen und der Schmerzintensität vorherzusagen. Die Stabilität der Beziehung wurde durch Kreuzvalidierungsverfahren innerhalb und zwischen den Sitzungen untersucht, d.h. ob die in einer fMRT-Sitzung gelernte Beziehung zur Vorhersage der Hirnaktivität in einer anderen Sitzung verwendet werden kann. Sowohl der Lernansatz zwischen den Sitzungen ('between-session') als auch innerhalb einer Sitzung ('within-session') wurden auf Gruppen- und Einzelsubjektebene getrennt betrachtet, was zusammen zu vier verschiedenen analysierten Varianten führte. Die Leistungsschätzungen beider Modelle wurde mit einem Null-Modell verglichen und anhand der absoluten Leistungsmetrik des mittleren quadratischen Fehlers (Root Mean Squared Error, RMSE) und des quadrierten Korrelationskoeffizienten R^2 als relatives Maß bewertet.

Im ersten voxelbasierten Ansatz auf Gruppenebene wird die Schmerzintensität bei chronischen Rückenschmerzpatienten im anterioren insulären Kortex, im frontalen Operculum und im Pons kodiert; die Veränderung des Schmerzes bei chronischen Rückenschmerzen und chronischer Migräne wird hauptsächlich im anterioren insulären Kortex kodiert. Auf individueller Ebene wurde ein komplexeres Muster identifiziert, bei dem jeder Patient seine eigene Signatur der endogenen Schmerzverarbeitung aufwies.

Die Konnektivitätsanalyse ergab, dass Zeitintervalle mit starken wie auch mit zunehmende Schmerzen überwiegend mit einer niedrigen kortikalen Konnektivität verbunden waren. Für die Kohorte der chronischen Rückenschmerzen gilt dies für die schmerzintensitätsbezogene Konnektivität für limbische und zinguläre Areale sowie für den Precuneus. Die Änderung der Schmerzintensität wurde durch Verbindungen in linken parietalen operculären Regionen, rechten insulären Regionen sowie großen Teilen des parietalen, cingulären und motorischen Kortex kodiert. Die Intensitätsänderung des Schmerzes bei Patienten mit chronischer Migräne spiegelte sich in einer abnehmenden Konnektivität zwischen dem anterioren insulären Kortex und orbitofrontalen Bereichen sowie zwischen dem posterioren cingulären Kortex (PCC) und frontalen und anterioren cingulären Kortexregionen (ACC) wider. Es wurden positive und negative Beziehungen zwischen der Schmerzwahrnehmung und korrelierten Hirnaktivitäten aufgedeckt, aber kein Effekt für antikorrelierte (d.h. unterdrückende) Hirnregionen gefunden.

Insgesamt waren die überwachten maschinellen Lernmodelle im dritten Analyseschritt nicht in der Lage, die Schmerzintensität auf der Grundlage der BOLD-Gehirnaktivität vorherzusagen. Die Leistungsschätzungen der beiden untersuchten Regressionsmodelle waren für alle vier untersuchten Varianten bei chronischen Rückenschmerzpatienten und chronischen Migränepatienten, insbesondere aber bei CM-Patienten, schlecht. Dennoch erreichte der 'within-session'-Ansatz eine höhere Genauigkeit als der 'between-session'-Ansatz, und das Lernen auf Einzelpersonenebene zeigte bessere Ergebnisse als das Lernen auf Gruppenebene für CBP-Patienten. Das Maximum von $R^2 = 0.46$ wurde in der CBP-Kohorte auf Subjektebene innerhalb einer Sitzung erzielt.

Dies ist die erste Studie eines kombinierten Sliding-Window-BOLD- und dynamischen funktionellen Konnektivitätsansatzes mit einem kontinuierlichen, reizfreien fMRT-Paradigma zur Schmerzbewertung sowohl bei chronischen Rückenschmerz- als auch bei chronischen Migränepatienten. Mit diesem naturalistischerem fMRT-Design wird eine größere Alltagsrelevanz erreicht, die durch methodische Fortschritte ermöglicht wird, einschließlich der Kombination einer nicht-binarisierten Schmerzintensitätsbewertung, eines Sliding-Window-Ansatzes zur Auflösung der unbekannten Dynamik der neuronalen Prozesse, einer dynamischen funktionellen Konnektivitätsanalyse, linearer Mixed-Effects-Modelle und einer Korrektur für Mehrfachvergleiche mit Surrogat-Daten. Darüber hinaus wurde besonderes Augenmerk auf die Ausführung der Schmerzbewertung der Probanden sowie auf wiederholte und erweiterte fMRT-Akquisitionen zur robusten Analyse gelegt.

Die beobachtete Vielfalt der individuellen kortikalen Signaturen der chronischen Schmerzkodierung deckt sich mit klinischen Beobachtungen: Ärzte haben es oft mit Patienten zu tun, die eine einzigartige Zusammensetzung von Charakteristiken, Persönlichkeitsmerkmalen und verschiedenen Kombinationen von Symptomen aufweisen und daher sehr unterschiedlich auf eine Behandlung reagieren. Ansätze des maschinellen Lernens zur Vorhersage der Schmerzintensität allein auf der Grundlage von BOLD-Aktivierungen können die persönlichen Angaben der Patienten noch nicht ersetzen, aber verbesserte Lösungen könnten in Zukunft ergänzend in den klinischen Bereich eingeführt werden. Die gewonnenen kortikalen Signaturen der chronischen Schmerzkodierung tragen zum Verständnis des chronischen Schmerzes als komplexe und vielschichtige Erkrankung bei und unterstützen die jüngsten Entwicklungen für eine stärker personalisierte Medizin.

3 Introduction

Medical imaging methods such as functional magnetic resonance imaging (fMRI) as well as electroencephalography (EEG) or magnetoencephalography (MEG) allow for a non-invasive investigation of the human brain structure [216]. fMRI is sensitive to changes in blood-oxygen-level-dependent (BOLD) signal, which is indicative of neuronal activation. Activity changes in response to internal or external stimuli as well as tasks can therefore be detected and assigned to specific brain regions or functional networks. Patterns of coherent brain activity, referred to as functional connectivity (FC), are investigated to probe the large-scale connections and networks of brain activity. Over the last few decades, fMRI alongside structural imaging, has thus been seen as a general mapping tool to explore brain function and organization [50, 161, 183, 198, 237, 302].

Neuroimaging provides the possibility to identify the basis of brain metabolism, the neuronal processing, as well as alterations due to diseases and e.g. pain disorders. Studies investigating the neuronal underpinnings of pain primarily focus on brain activity related to external stimulation and the identification of changes within specific pain conditions compared to healthy controls. Although brain regions associated with pain have been investigated since the late 1970s the exact pathophysiology has not been elucidated yet. One of the reasons may be that pain is predominantly considered as a symptom and not as a disease itself. Especially for chronic pain diseases which manifest in altered functional processing as well as structural changes in brain areas, the chronification process as well as the cause and neuronal mechanisms of the maladaptive cortical processing are all still unknown [90]. This despite the fact that chronic pain is one of the largest medical health problems in the world which affects approximately 20 % of the adult population [284]. While the management and treatment of acute pain is reasonably good, the needs for chronic pain patients are largely unmet, creating an enormous burden on the individual and the society. It is estimated that in Europe 200 billion euro are spent on chronic pain per year. A huge step forward has been the classification of chronic pain as a disease itself by the International Classification of Diseases (ICD) in 2018, but improvements in the individual diagnostic, assessment and treatment are still needed [285]. Additionally, as pain is a subjective experience by nature, several factors shape the "brain in pain" for each individual, incorporating personal experience, learned strategies to deal or avoid pain and external influences. This diversity complicates the search for a universal neuronal representation of pain leading to interindividual variability in treatment outcome for patients. Only by combining different methodological approaches which measure BOLD activation as well as functional communication across several brain regions in brain networks, the neuronal basis and its alterations can be understood [207, 252].

In addition to hypothesis-driven statistical approaches, many machine learning (ML) applications have been applied to neuroimaging in recent years to decode different aspects of the diseased brain. ML methods are especially useful, when different patterns of multiple brain regions distributed over the whole brain are involved in the cortical processing as e.g. in the pain experience. Imaging combined with ML algorithms could provide a direct, objective mea-

sure of pain intensity without the need of self-report. Patterns of neuronal activity thus could serve as potential objective biomarkers to detect disorders or subtypes of diseases for clinical practice [74, 198, 295].

The purpose of this thesis is the investigation of the continuous, real-time, endogenous pain experience and its neuronal representation within the brain in two chronic pain cohorts with fMRI. Although the fluctuating pain intensity represents an important daily life experience of chronic pain patients, this phenomenon is barely investigated. The functional underpinnings of patients with chronic migraine (CM) and chronic back pain (CBP) are investigated in a whole-brain analysis in three consecutive steps: first with BOLD activity analysis to identify active regions during the pain rating task. Subsequently, the interaction patterns between these regions are analyzed with a FC analysis and finally, the stability of pain ratings as well as the potential to predict pain intensity levels based on BOLD activity are tested with a supervised ML approach.

Following a short introduction into the neuroscience of pain (Chapter 4) an overview of the current state of the literature is given in subsection 4.3.2. The principles of magnetic resonance imaging (MRI) (Section 5.1) as basis for functional magnetic resonance imaging (Section 5.2) and preprocessing techniques (Section 5.3) are then covered. The statistical (Chapter 6) and machine learning (Chapter 7) basics conclude the first part of this thesis with theoretical and methodological foundations and the state of the literature. The objectives alongside the hypotheses of this work are given in Chapter 8 before the three consecutive studies are presented in Chapter 9. The joint materials and methods of the three different analysis approaches are covered in Sections 9.1 and 9.2, followed by the individual specific analyses and results of the BOLD (Section 9.3), connectivity (Section 9.4) and machine learning approach (Section 9.5). An overall summary with a future outlook concludes this thesis (Chapter 10).

4 Neuroscience of pain

This chapter gives an introductory overview of the most relevant processes involved in the human pain experience. Pain is considered an adaptive response, alerting the organism to avoid potential harmful situations or actual sources of pain. Generally, pain is divided into several subtypes depending on involved symptoms and mechanisms [313]. A simplified description from nociception to two chronic pain disorders, which are topics of further detail in this work, are given; more detailed information on the medical background and general brain structures, including, e.g. the neurochemistry of brain signal transduction, can be obtained in Schmidt et al. [249] or Schneider et al. [250]. An overview of the current state of the literature concludes this chapter before the foundations of fMRI are covered in chapter 5.

4.1 Nociception and pain pathways

The encoding of actual or potential painful stimuli is referred to as human nociception and includes, e.g., mechanical or thermal stimuli and its resulting signal transmission to the brain [301]. Nociceptors are for example found on the skin and are part of peripheral sensory neurons. In the human brain, approximately 86 billion connected neurons process and transmit information through electrical and chemical signals [22]. When these so-called (afferent) nociceptors are activated by the detection of a potential noxious input, the signal is first relayed to the dorsal horn (DH) in the spinal cord via the myelinated Aδ-fibers with comparably fast conduction velocity (30 m/s) and unmyelinated, and therefore slow conducting (2 μm/s), C-fibers. From there, the signals are transmissioned to the brain by the central nervous system (CNS). In this way, the combined integrated signals of neurons and their coordinated activity carry the signal from the peripheral source to the spinal cord and further to the brain which then leads to a sensation of pain [129, 313].

Ascending and descending pathways
Two major general directions of pathways have been identified for signal transmissions: ascending and descending pathways. Ascending signals originating from the DH primarily project to the thalamus and then further to the somatosensory cortex mostly via the spinothalamic tract. Ascending pathways and several brain regions (see below and Figure 4.1) are activated by nociceptive input and participate in the processing of pain. Although the spinothalamic tract is responsible for most transmissions, no 'hard-wired' path between the original (peripheral) nociceptive neurons and the final cortical representation of input has been identified – instead, multiple ascending (bottom-up) as well as descending (top-down) modulatory circuits, with enhancing or diminishing effects on the signal at numerous regions, constitute the ultimate experience of pain [46].

Besides the main ascending pathway via the spinothalamic tract, there are also direct connections to the medulla (part of the midbrain) and brain stem via the spinoreticular and spinomesencephalic tracts as well as to the hypothalamus via the spinohypothalamic tract.

Thus, ascending information also integrates the periaqueductal gray (PAG) and rostral ventral medulla (RVM) in the descending feedback systems, in order to modulate the output signal from the spinal cord. The existence of a descending pain modulatory system was postulated in 1911 [122] and improved later with the gate control theory in 1965 [192] and 1976 [186] with the concept of a descending analgesic system. The descending pain modulatory pathway is a highly organized network that enables top-down regulation of afferent nociceptive information. Brain regions associated with the descending pain modulatory pathway include the hypothalamus, ACC, insula, amygdala, and the frontal lobe. These regions then project to the PAG where top-down projections from higher brain centers as well as bottom-up nociceptive input from the dorsal horn are processed. The core hub of the descending pathway is the RVM, serving as the prime output node, communicating with the PAG and DH. The exact number and extent of involvement of specific brain regions are variable and controversial across neuroimaging studies. A simplified depiction of the pathways is given in Figure 4.1 [1, 231, 264, 285, 301, 315].

Nociception vs Pain
Pain is not simply an expression of nociception but comprises a multidimensional experience that can be modulated by, e.g., negative emotions, anxiety, depression, attentional focus or anticipation, affecting the perception of pain or pain intensity. Hence, pain and nociception often occur in conjunction, one leading to the other with a bi-directional influence, but are not exclusively bound to one another and must be differentiated. Pain is defined by the International Association for the Study of Pain as "an unpleasant sensory and emotional experience associated with actual or potential tissue damage, or described in terms of such damage" [193]. This definition implies the involvement of not only sensory-discriminative features (intensity, quality, location), but also cognitive and emotional factors (memory, motivation, attention) contributing to the processing of pain perception [42, 53, 74, 285]. Therefore, pain is considered a complex, multifactorial and subjective experience, which results from a combination of both peripheral and CNS interactions, involving several brain systems for which simple subjective self-report is currently the gold standard for assessment [15, 42, 53, 198, 260, 267, 285].

4.2 Pain in the brain

The representation of the complexity of the multifactorial, subjective experience of pain in the brain is distributed over neuronal networks of brain regions that include a multitude of cortical and subcortical areas which all encode some distinct aspects of pain. In the past, this network structure of pain regions has been referred to as the "pain matrix" or "neuromatrix of pain" [133, 191]. Nowadays, it is more appropriately referred to as "pain connectome" [152]. Rather than looking for activity in one specific cortical area or dedicated "pain centers" within the brain, pain is associated with activity in many brain areas that belong to different functional brain systems and the interactions between all these regions sum up to a net result of perceived pain [1].

Neuroimaging studies have most consistently revealed the following cortical areas associated with the perception of pain: primary and secondary somatosensory cortices (S1 and S2), insular cortex (IC), anterior cingulate cortex, thalamus (Th), and prefrontal cortex (PFC) [28]. Further subcortical areas include the cerebellum, amygdala, nucleus accumbens and periaqueductal gray commonly reported in pain studies. Based on the projection sites from the thalamic

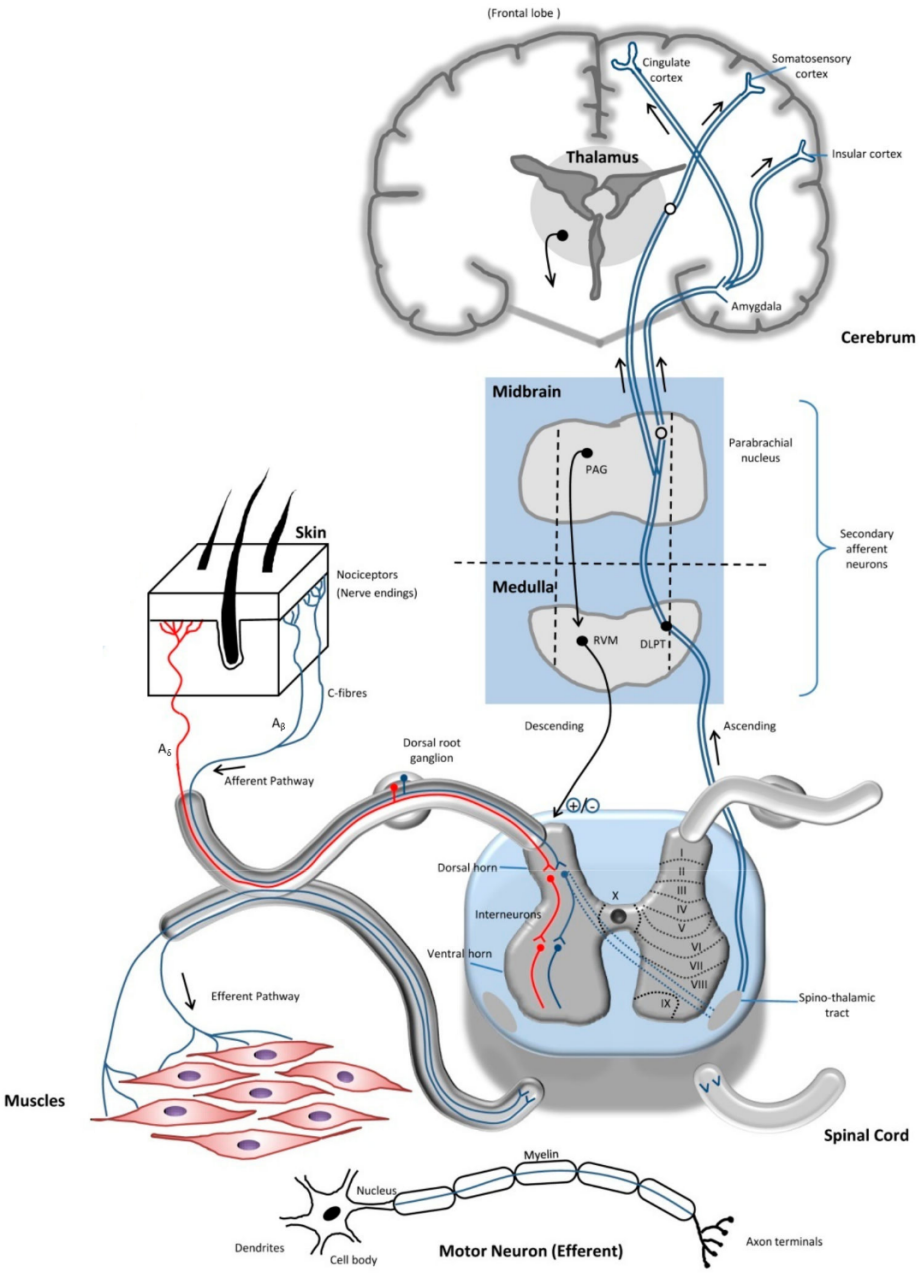

Figure 4.1: Pain pathways: ascending (blue) and descending (black) pathways from noxious stimuli; adapted from [313].

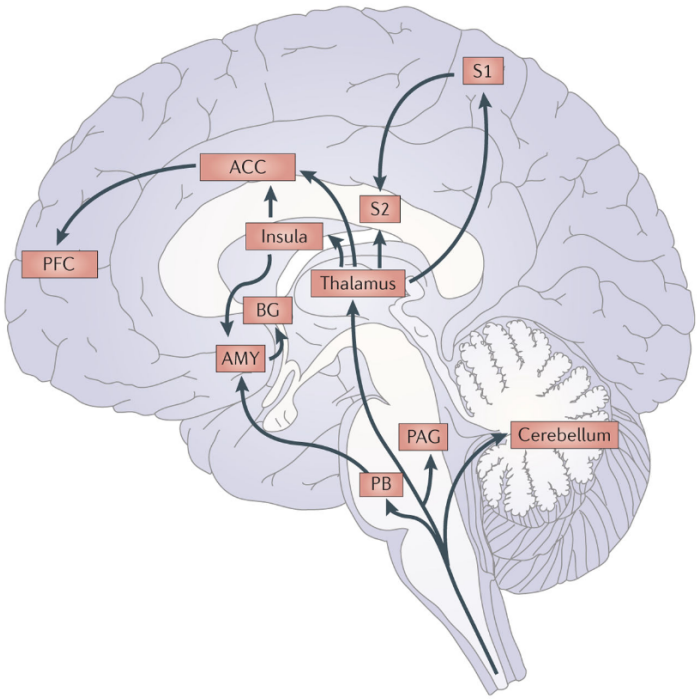

Figure 4.2: Brain regions involved in the pain connectome include the primary (S1) and secondary somatosensory (S2) cortices, the thalamus, insula, anterior cingulate cortex (ACC) and prefrontal cortex (PFC) as well as the amygdala (AMY), basal ganglia (BG), parabrachial nucleus (PB), periaqueductal gray (PAG) and the cerebellum; adapted from [53].

structures to the cortex, these structures can be simplified into two systems with regard to their primary role within the processing of nociceptive information: the medial and lateral pain system. The lateral pain system foremost encodes the sensory-discriminative features of pain in somatosensory regions and parts of the thalamus as well as of the cerebellum. Contrary, the medial pain system encodes the affective-motivational aspects of pain, mainly located in the cingulate, prefrontal areas and the insula [15, 53]. Even subdivisions of the individual regions with their contributions to pain experience have been found, e.g., activations in the posterior IC are more related to sensory aspects of pain, whereas the anterior IC may be more important in emotional, cognitive, and memory-related aspects of pain perception [285].

None of the described features or depicted regions in Figure 4.2 are pain-specific or pain exclusive, but participate in various other sensory and emotional states. Nociceptive stimuli can trigger a variety of processes not specific to pain but which are, nonetheless, part of the multidimensional nature which determines the pain experience. For instance, a previous study [295] included regions of the visual system (occipital lobe, fusiform gyrus) in their investigation of a brain signature ("neurological pain signature" (NPS)) specific to (thermal) pain [15, 42, 53, 74, 198, 285].

4.3 Chronic pain

Pain is foremost a survival mechanism and acts as a warning system for threats to the organism. However, in chronic pain conditions, pain persists even in the absence of acute tissue damage. When pain persists longer than three to six months, it is referred to as chronic pain. It is defined as "pain that is present every day for more than 3 months (or is present on $\geq$ 50 % of days for six months) or beyond the expected period of healing and does not have the warning function anymore that acute pain does" [286]. Chronic pain is considered as a disorder of the central nervous system (CNS) as it encompasses various brain networks, involving behavioral, cognitive, emotional and sensory components to produce the pain experience. Patients often suffer from an enormous reduction of life quality, as they experience steady or fluctuating, spontaneous, ongoing, stimulus-independent pain on a daily basis [74, 315].

Functional as well as anatomical changes with disrupted large-scale properties have been observed across several chronic pain disorders, including fibromyalgia [151], migraine [143] or chronic regional pain syndrome (CRPS) [32], but the exact underlying pathophysiology of chronic pain remains poorly understood. It is seen as a complex multidimensional disease, affecting the CNS and modifying several potential brain pathways involved in endogenous pain control. Compared to acute pain, chronic pain patients have reported distinct, abnormal activation patterns in pain regulation regions when external pain stimuli were applied, indicating that chronic pain alters the functional connections in the processing of pain. Several brain regions, e.g. the thalamus, cingulate cortex, dorsolateral and medial prefrontal cortices, as well as regions in the limbic system, have been assigned a significant role in the chronic pain experience (Figure 4.3). However, disease-related alterations are often specific to the chronic pain condition and most likely to the investigated population or even individual and do not generalize well to other ones [12, 13].

On the biological level, a central sensitization [310] with an increased activity of pain pathways or lack of inhibition/excitation at the cortical level, as well as an impaired functioning of the descending modulatory pain system, is thought to be at the center of chronic pain [217, 227]. Thus, pathways involved in endogenous pain control are thought to be modified in chronic pain, making self-regulation of pain challenging [183]. The nature of abnormal cerebral pain processing in chronic pain conditions is far from established but the findings suggest a profound alteration due to long-lasting pain in the brain – whether these changes are the cause or the consequence of the disease is still unclear as well [15, 42, 53, 74, 90, 130, 198, 231, 267, 285].

Two of the most common chronic pain conditions are chronic back pain (CBP) and chronic migraine (CM), which are investigated in this thesis and therefore mostly focused on from here on.

4.3.1 Chronic back pain and chronic migraine

Chronic back pain (CBP) is defined by the IASP criteria (The International Association for the Study of Pain [194]), which includes a disease duration of more than six months. CBP is one of the most common health problems around the world today with far-reaching social and economic consequences and severely impacting the lives of the individuals who suffer from it [48]. The population prevalence of chronic back pain in Germany is 15.5 % and is significantly higher in women (18.5 %) than in men (12.4 %) [166].

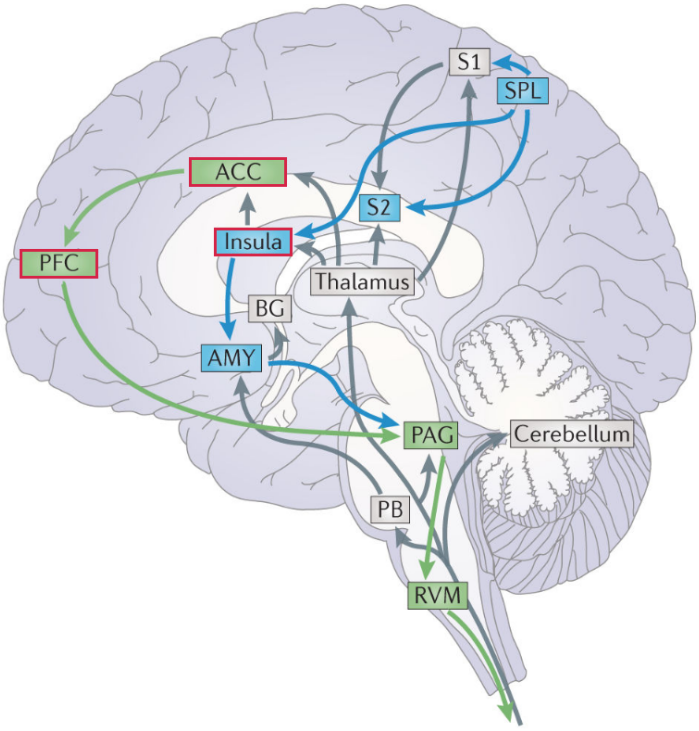

Figure 4.3: Brain regions involved in the chronic pain network: Regions that most consistently show changes in chronic pain diseases are the anterior cingulate cortex (ACC), prefrontal cortex (PFC) and insula (red outlined frame). Grey arrows show ascending pain pathways. Attention and emotion alter pain via different descending modulatory systems. Emotions activate circuitry involving the anterior cingulate cortex (ACC), prefrontal cortex (PFC) and periaqueductal grey (PAG) (shown in green), whereas attention activates circuitry involving projections from the superior parietal lobe (SPL) to the primary somatosensory cortex (S1) and insula (shown in blue). Grey regions show parts of the ascending pain pathways: amygdala (AMY), basal ganglia (BG), parabrachial nucleus (PB), rostroventral medulla (RVM) and secondary somatosensory cortex (S2); adapted from [53].

Chronic migraine is defined by the ICHD-3 (Headache Classification Committee of the International Headache Society (IHS) 2018), as a "headache occurring on at least 15 days per month for more than three months, which, on at least eight days per month, has the features of migraine headache" [215]. CM usually develops from episodic migraine (EM) (2.5 %), which is one of the most prevalent neurological disorders [139]. In a survey of 2020, a total of 57.5 % of women and 44.4 % of men in Germany reported that they had at least one headache in the last twelve months – 14.8 % of women and 6.0 % of men were affected by migraine. 1.2 % of participants had CM and 9.6 % had EM [228]. Migraine is an episodic, recurrent, genetically determined dysfunction of brain excitability that leads to an activation and sensitization of the trigeminovascular pain pathway, with the exact origin or migraine "generator" still unknown [88]. Migraine is characterized by episodic headaches associated with nausea, vomiting, hy-

persensitivities to somatosensory as well as visual or auditory stimuli and cutaneous allodynia (CA) [258], defined as "pain due to a stimulus that does not normally provoke pain" [159, 263].

To investigate chronic pain diseases, mainly fMRI designs with different methodological strategies and approaches, involving resting-state investigations as well as e.g. arterial spin labeling (ASL) or structural diffusion-tensor-imaging (DTI) measurements have been pursued to elucidate the different consequences and manifestations of the diseases, both functional and structural in nature. The following sections give an overview of the state of the art of chronic pain disease research.

4.3.2 State of the current literature

The majority of neuroimaging studies have applied noxious stimuli to chronic pain patients in order to investigate functional processing alterations. Functional neurological changes have been reported across several individual brain regions, whereas varying paradigms reveal different abnormalities, dependent on the investigated tasks, regions and patient populations.

Functional imaging of regional changes with experimental pain and resting-state designs in patients with chronic pain
External noxious stimuli are mostly applied through heat, i.e. thermal stimulation, or mechanically induced pain, as well as chemical or electric stimulation. Through experimental application of various exogenous pain stimuli, cortical regions involved in acute pain processing were found to mainly coincide with regions found to be active in the processing of chronic pain (i.e. S1, S2, Th, IC, CE, and ACC) [15, 25, 88, 101, 107, 177, 288].

Although activation of many regions overlap with the processing of acute pain, several key regions were consistently found to show functional activity alterations in chronic pain states. Altered pain intensity processing was attributed to changes in the posterior insula and primary somatosensory cortex in e.g. patients with chronic back pain and fibromyalgia [291]. As these regions are typically associated with the encoding of pain intensity, changes in these regions suggest altered intensity processing in chronic pain. Additionally, regions within the PFC, as well as within the parietal cortex (precuneus, PCC, temporoparietal junction (TPJ)) show functional changes. The PFC regions were found to mediate the relationship between cognitive processes and chronic pain, whereas the parietal cortex includes regions which are mainly associated with introspection as well as self centering thoughts and may reflect the increase in contemplation and rumination around the chronic pain disease. Emotional processing regions such as hippocampus and amygdala show abnormal functional involvement in different chronic pain states, representing the psychological facet often accompanying the underlying disorder [17, 153].

Overall, the evaluation of brain responses to experimental pain have suggested that the accompanied sensitivity to noxious stimuli reported by chronic pain patients is effectively accompanied by enhanced brain responses [110] and impaired functioning of the descending modulatory pain system. These studies therefore indicate that the augmentation of central processing of pain, disruption in the pain modulatory system, and/or an "overload" of the latter due to the ongoing chronic pain are all plausible and possible mechanisms underlying the pathophysiology of chronic pain.

However, as the neuronal response to pain is greatly dependent on the specific characteristics of the subject, unique activation patterns of brain regions are assumed to shape the experience of pain [152, 285]. The intensity of the perceived pain is suggested to depend on the individual as well as neuronal responses to pain, changing more to one's perception than to the absolute value of external stimuli [198, 255]. Externally applied pain to chronic pain patients thus may not be able to accurately capture the natural behavior of individual chronic pain patients.

The exact opposite to external noxious stimuli designs are resting-state approaches. Resting-state fMRI designs investigate the brain at rest or explicitly without the performance/execution of a specific task during the fMRI scan.
Resting-state studies identified increased activation in specific individual brain areas, i.e. the mPFC [25, 120], cingulate cortex [148], amygdala [26], and insula [277] in chronic back pain patients. Decreased activity was also reported in the PAG, indicating disrupted regulatory control of the pain experience [182].
In the search for a migraine "generator", specific individual regions have been investigated, e.g., the hypothalamus (part of the descending pain modulating network) and the pons, which are suggested to be a driving force of migraine attacks [159]. Functional imaging studies reported increased activity as well as altered functional coupling of the hypothalamus during the preictal phase [253]. Even different subparts of the hypothalamus have been distinguished to play a part in migraine attacks as well as the chronification process of migraine; e.g., the anterior hypothalamus is crucially involved in the abnormal functional physiology of chronic migraine [66], whereas the posterior hypothalamus was distinctly related to the acute state of a migraine attack [88, 252]. Similarly, the dorsal pons showed increased activations during spontaneous migraine attacks as well as during and outside the headache phases in CM. Thus the pons has been attributed a central role both in the generation of migraine attacks as well as the transition from acute towards chronic pain [88].

Imaging Brain Connectivity in Patients with chronic pain
In addition to individual brain region alterations, changes in larger scale networks with functional or structural connected brain areas have been investigated with external stimuli, visual tasks, but mainly with resting-state approaches. A large number of studies have demonstrated that the presence of chronic pain affects the functional connectivity among interacting brain regions.

Network specific alterations have been found across several chronic pain states and systems, e.g., the sensory-motor system (including S1, S2 and M1) [147, 148, 298], the attention network [163] and the salience network [74]. Different studies have investigated the brain structures associated with the emotional aspects of pain and showed changes in the connections of the reward system, including the mPFC and nucleus accumbens, as well as FC changes between the PAG and ACC [25, 26, 120]. The majority of resting-state investigations so far have focused on the default mode network (DMN), which is active during rest and internal self-reflection [26, 108, 288]. The DMN, including the medial prefrontal, posterior cingulate and lateral temporal cortices, the hippocampal formation, and inferior parietal lobule, which are frequently observed as deactivated during attention-demanding tasks and have extensive overlap with regions that are thought to be involved in self-referential cognitive processing, were foremost reported to show an intrinsic whole-network disruption in chronic pain patients, especially with higher pain

intensities. Higher pain intensities were also related to greater connectivity between the DMN and the insular cortex [150, 169, 277]. This leads to a consensus assumption that the "chronic pain brain" is never truly at rest and that with increased pain (intensity) a greater disruption of a "resting brain" takes place, hindering the patient's daily life.

More specifically, studies have shown alterations in DMN connectivity in patients with CBP [26, 169] and fibromyalgia (FM) [206]. One study [206] demonstrated that FM patients exhibit greater connectivity between DMN and IC and S2 and that the strength of connectivity between DMN and insula predicted spontaneous pain. Interestingly, a very similar association between DMN-insula connectivity and clinical pain has also been found in patients with chronic low back pain, using imaging [169]. The observation that a common neuroimaging metric appears to encode clinical pain in different patient populations raises the intriguing possibility that such measures may reflect a general feature of chronic pain, which can be used to identify the disease.

In particular, CBP patients, compared to healthy subjects, showed increased FC in regions including S1 and S2, lateral orbitofrontal cortex, inferior parietal lobe, and the cerebellum [100, 101] as well as in the PCC and insula [146]. During thermal stimulation, a negative correlation between mPFC and DLPFC for high pain states and a strong connectivity between nucleus accumbens and mPFC cortex was found [31].
CM-patient-specific altered functional activation of combined brain structures include the salience network, the DMN, regions involved in the sensory-discriminative and affective aspects of pain (insula, anterior cingulate, prefrontal, and somatosensory cortex) as well as the executive control, and dorsal-attention network. Overall, this points towards a central sensitization with impaired facilitatory and inhibitory network activity, where patients with CM exhibit lower pain thresholds to external stimuli and altered attentional processing of non-painful or painful situations [9, 10, 21, 39, 70, 88].

Structural changes
In addition to changes in brain activity and functional coupling between specific brain regions, structural changes in the brain of chronic pain patients have been observed. The first study [14] reporting structural alterations in the brain of a chronic pain condition observed a reduction in grey matter density in the prefrontal cortex and thalamus in a cohort of patients with chronic back pain. Since then, several other studies have reported morphological changes in cortical thickness for an abundance of chronic pain disorders, including FM [151], migraine [143] or CRPS [32] but with diverse results. While many studies suggest the presence of structural changes, the specific brain regions associated with such changes and even the direction of these changes vary between studies.

Structural changes include grey matter density reduction in several pain related regions, e.g., in the DLPFC and mPFC, the ACC, the IC or the primary somatosensory cortex, as well as in the hippocampus and amygdala for e.g., chronic back pain [14, 27]. Several other brain areas are reported to have changed global grey matter volume, though very inconsistent results are reported. Both increased as well as decreased volume was found for the following regions: putamen, caudate nucleus, thalamus, pons, S2, and cerebellum. These conflicting results in both directions of volume changes indicate a fundamental change in the brain structure of chronic back pain patients most likely due to the long-term exposure to pain, but further re-

search needs to clarify the exact changes. Additionally, linear relationships between structural brain changes and behavioral parameters, e.g. the duration of chronic pain, have been found indicating that extended changes happen over time [14, 27, 184].

Specifically for CM, some studies [40, 71, 208, 259] compared healthy controls to chronic migraine patients and reported structural changes across various brain regions which are known to take part in the diverse aspects of pain modulation and processing: Both increases in grey matter volume as well as a reduction in grey matter volume were found in the amygdala, basal ganglia, brainstem, cerebellum, frontal, temporal, and occipital areas [88].

However, results from a study investigating the cortical thickness before and after successful treatment of CBP patients indicate increased cortical thickness in e.g. the DLPFC after compared to before treatment [265]. These findings suggest that both altered brain function and structure may be reversible leading to the intriguing possibility that through proper feedback training a redirection of maladaptive brain communications to that of a healthy brain can be achieved.

Investigations of clinical pain

The great majority of imaging studies investigating the underpinnings of the pain experience have focused on evaluating the response to controlled stimulation from externally applied pain. In contrast, very few studies have attempted to evaluate the neuronal correlates of clinical pain, specifically, spontaneous pain in the absence of external stimuli [28, 118, 119, 185]. Although this is at the center of every chronic pain patient's daily life, it has been barely investigated as such [159, 177]. Methodological difficulties hinder the unraveling of the true underlying neuronal processes of chronic pain, as, unlike experimental pain, chronic pain is fluctuating over different timescales and thus can not be shaped into a balanced experimental design with "on" and "off" states, making the investigations of chronic pain diseases as such more complicated.

The majority of the few studies mentioned above have utilized an experimental approach of continuously evaluating the spontaneously fluctuating pain without external stimulation in CBP patients. They reported higher activity in the medial prefrontal cortex for high pain compared to low pain intensity. When periods of increasing pain were contrasted to periods of stable or decreasing pain, effects in the right anterior and posterior insula, S1 and S2, the middle cingulate cortex, and the cerebellum were reported [28]. Similarly, looking at other imaging modalities, higher pain intensities were related to larger amplitudes of neuronal gamma oscillations at frontocentral electrode sites in EEG measurements [185]. Clearly, there is a lack of investigations into the underpinnings of clinical pain without the additional application of external noxious stimuli of any kind, investigating the true underlying processing of the chronic pain experience.

All in all, for CBP, the exact underlying pathophysiological mechanisms as well as the exact chronification process are still unclear, although regions involved in processing emotions have been associated with the chronification of pain. Previous studies found the amygdala, the mPFC, and the nucleus accumbens to be important in the transition from subacute to chronic back pain [120, 176]. Due to the huge variety of disease manifestations alongside sev-

eral comorbidities (e.g., depression, anxiety), approaches (e.g., resting-state, noxious stimuli) and methods (e.g., BOLD activity, structural imaging), the investigation of chronic pain lacks a ground-truth and many contradicting results can be found in the literature. Nevertheless, a majority of neuroimaging studies indicate that a deactivation in pain-related regions, as occurs in healthy controls, is not exhibited in patients with CBP, most likely related to the widespread changes in the brain due to long-lasting pain [24, 267, 282].

The same applies to CM where the neuronal or pathophysiological mechanisms responsible for migraine chronification have not been fully elucidated yet. The few imaging studies so far which have investigated chronic migraine patients have used resting-state fMRI designs and external applied stimuli as well as structural imaging and compared their findings with healthy control groups to investigate functional and structural alterations. Whether structural changes and functional reconnections pose a predisposition for the transition from acute to chronic pain or are part of the brain's coping mechanism and are the consequence of the prolonged suffering from pain has not yet been elucidated. Some studies attribute the hypothalamus a differentiating role between episodic and chronic migraineurs [252]. Comparisons between episodic and chronic migraine patients show more psychiatric comorbidities in the chronic migraine cohort which make the disentanglement of the specific underlying cause even more challenging [52]. Difficulties in interpreting the findings additionally result from the variety of timepoints in the migraine cycle of each patient in which they were measured, i.e. with or without headache during the examination, with or without migrainous features, interictal or ictal phase when compared to episodic migraineurs [88]. Although multiple factors promoting migraine chronification, such as, e.g. medication overuse have been identified [240], one of the biggest challenges remains the identification of the brain circuitry sub-serving and encoding the clinical perception of pain in this highly disabling disorder of brain function [159, 263].

Overall, patients diagnosed with CBP and CM have shown to have altered activation patterns as well as functional connectivity and fundamental structural changes in the brain compared to healthy controls. Although several brain regions and networks contributing to the pain experience were investigated and have shown alterations compared to healthy subjects, so far no clear pattern representing the pain encoding with its several modulatory processes of increasing or decreasing pain in CBP and CM has been identified [25, 146, 277].

5 Functional magnetic resonance imaging

This chapter starts with the basic theoretical foundations on the most important properties and processes of magnetic resonance imaging in section 5.1, followed by the basic principles of fMRI and, the BOLD effect in section 5.2. The background on the preprocessing pipeline of fMRI data is given in section 5.3. More detailed information can be found in Callaghan et al. [56] or Haacke et al. [114].

5.1 Magnetic resonance imaging (MRI) basics

5.1.1 MRI physics

An atomic nucleus with an odd number of protons and/or neutrons possesses a non-vanishing angular momentum $\boldsymbol{I}$ in its ground state, which is also referred to as nuclear spin. The nuclear spin of an atomic nucleus results from the vector sum of the intrinsic and orbital angular momenta of its constituent nucleons (protons and neutrons). The value I of the spin thus depends on both the mass and atomic number and is quantised, taking only zero, discrete positive integer or half-integer values. The net spin angular momentum is always associated with a magnetic moment $\boldsymbol{\mu}$ which provides the foundation of MRI. The relationship between the nuclear magnetic moment $\boldsymbol{\mu}$ and the nuclear spin $\boldsymbol{I}$ is given by

$$\boldsymbol{\mu} = \gamma \boldsymbol{I} \tag{5.1}$$

where the constant of proportionality γ is known as gyromagnetic ratio and is nucleus-specific. In clinical practice the nucleus of the hydrogen atom ^{1}H (spin quantum number of $I = 1/2$ and $\gamma = 2.675\times\ 10^8$ rad $\mathrm{T}^{-1}\mathrm{s}^{-1}$) is almost exclusively used [116, 236, 275].

5.1.2 Nucleus in a magnetic field and macroscopic magnetization

If no magnetic field is present, all magnetic moments in a macroscopic sample are randomly oriented due to their thermal motion. In contrast, if the magnetic moments are exposed to an external magnetic field $\boldsymbol{B_0}$, they tend to align parallel to the external magnetic field to minimize the potential energy of the system. However, if a sample magnet (such as an atomic nucleus) possesses an angular momentum, it cannot align parallel to the external field due to the conservation law of angular momentum. In this case, it experiences a torque

$$\boldsymbol{\tau} = \boldsymbol{\mu} \times \boldsymbol{B_0} \tag{5.2}$$

which is perpendicular to both the direction of the magnetic field $\boldsymbol{B_0}$ and the angular momentum $\boldsymbol{I}$. This results in a precession of the magnet on a cone about the direction of the external $\boldsymbol{B_0}$ field [236].
Looking at the change of angular momentum over time, $d\boldsymbol{I}/dt$, one obtains with equation 5.1, the fundamental equation of motion for the magnetic moment in the presence of an external field $\boldsymbol{B_0}$

$$\frac{d\boldsymbol{\mu}}{dt} = \gamma \boldsymbol{\mu} \times \boldsymbol{B_0}. \tag{5.3}$$

Solving this equation for a static magnetic field $\boldsymbol{B_0}$, one finds that the magnetic moment is precessing around the field direction with the Larmor frequency ω_0 being proportional to the strength of the magnetic field $\boldsymbol{B_0}$

$$\omega_0 = \gamma B_0. \tag{5.4}$$

Typical field strengths in clinical settings range from 1.5 – 3 T corresponding to a Larmor frequency of 64 – 128 MHz [236].

Volume elements (voxels) acquired in MR imaging are large enough to contain huge amounts of protons, each having its own spin and associated magnetic moment. In each voxel, a dynamic equilibrium exists in which the proton spins can be regarded to occupy different possible energy states, characterized by the quantum number m. The slightly different population of these $(2I + 1)$ levels (for a system with spin quantum number I) is given by the Boltzmann statistic (with Boltzmann constant k) and results in a macroscopic magnetization

$$M = \frac{N\gamma\hbar}{V} \cdot \frac{\sum_{m=-I}^{m=+I} m \cdot \exp(\gamma\hbar m B_0/kT)}{\sum_{m=-I}^{m=+I} \exp(\gamma\hbar m B_0/kT)} \tag{5.5}$$

with N nuclear spins in a volume V. Due to the little difference in occupation numbers of the spin states a magnetic moment along the direction of the $\boldsymbol{B_0}$ field is obtained. The summation of a large number of nuclear magnetic moments per unit volume V then leads to a macroscopic magnetization $\boldsymbol{M}$ with its magnitude in thermal equilibrium approximated by

$$|\boldsymbol{M}| = M = \frac{1}{V}\sum_{i=1}^{N}(\mu_z)_i = \frac{N}{V} \cdot \frac{\gamma^2\hbar^2 I(I+1)B_0}{3kT} \tag{5.6}$$

where N is the total number of nuclei in the sample, T the absolute temperature of the sample, and $\rho = N/V$ the so-called spin density.
Replacing the magnetic moment $\boldsymbol{\mu}$ with the net macroscopic magnetization $\boldsymbol{M}$, equation 5.3 now becomes

$$\frac{d\boldsymbol{M}}{dt} = \gamma\boldsymbol{M} \times \boldsymbol{B_0} \tag{5.7}$$

and describes the time evolution of the net macroscopic magnetization in an external magnetic field $\boldsymbol{B_0}$ [56, 117, 213, 236, 275].

5.1.3 Radiofrequency excitation

The initial dynamic equilibrium of the spin system, where $\boldsymbol{M}$ is aligned with the static $\boldsymbol{B_0}$-field, can be perturbed by a magnetic radiofrequency (RF) field $\boldsymbol{B_1}(t)$ with a frequency ω_{rf} equal to the Larmor frequency ω_0, which influences the angle between $\boldsymbol{M}$ and $\boldsymbol{B}_0$. The $\boldsymbol{B_1}(t)$ field is given by

$$\boldsymbol{B_1}(t) = B_1\cos(\omega_{rf}t)\hat{\boldsymbol{i}} - B_1\sin(\omega_{rf}t)\hat{\boldsymbol{j}} \tag{5.8}$$

where $\hat{\boldsymbol{i}}$, $\hat{\boldsymbol{j}}$, $\hat{\boldsymbol{k}}$ are unit vectors along the x-,y-, and z-axes, respectively. The net magnetization vector now precesses about $\boldsymbol{B_1}$ described by

$$\frac{d\boldsymbol{M}(t)}{dt} = \gamma\boldsymbol{M}(t) \times (\boldsymbol{B_1}(t) + \boldsymbol{B_0}) = \gamma\boldsymbol{M}(t) \times (B_1(\cos(\omega_{rf}t)\hat{\boldsymbol{i}} - \sin(\omega_{rf}t)\hat{\boldsymbol{j}}) + B_0\hat{\boldsymbol{k}}). \tag{5.9}$$

After transformation in the rotating frame of reference ($x' = x\cos(\omega_{rf}t) + y\sin(\omega_{rf}t)$, $y' = -x\sin(\omega_{rf}t) + y\cos(\omega_{rf}t)$, $z' = z$), the above equation becomes

$$\frac{d\boldsymbol{M}(t)}{dt} = \gamma \boldsymbol{M}(t) \times (B_1 \hat{\boldsymbol{i}}' + (B_0 - \frac{\omega_{rf}}{\gamma})\hat{\boldsymbol{k}}) \tag{5.10}$$

which simplifies to

$$\frac{d\boldsymbol{M}(t)}{dt} = \gamma \boldsymbol{M}(t) \times B_1 \hat{\boldsymbol{i}}' \tag{5.11}$$

when the resonance condition, $\omega_{\mathrm{rf}} = \omega_0$, is met.
For the three components the equations and solutions for the initial condition $\boldsymbol{M}(\mathrm{t}) = M_0\hat{\boldsymbol{k}}$, are given with $\omega_1 = \gamma B_1$ by:

$$\begin{aligned}
\frac{dM_x}{dt} &= \gamma[M_y B_0 + M_z B_1 \sin(\omega_0 t)] & M_x(t) &= M_0 \sin(\omega_1 t)\sin(\omega_0 t) \\
\frac{dM_y}{dt} &= \gamma[M_z B_1 \cos(\omega_0 t) - M_x B_0] & M_y(t) &= M_0 \sin(\omega_1 t)\cos(\omega_0 t) \\
\frac{dM_z}{dt} &= \gamma[-M_x B_1 \sin(\omega_0 t) - M_y B_1 \cos(\omega_0 t)] & M_z(t) &= M_0 \cos(\omega_1 t)
\end{aligned} \tag{5.12}$$

This shows that the magnetization simultaneously precesses about $\boldsymbol{B_0}$ at the Larmor frequency ω_0 and about the RF field $\boldsymbol{B_1}$ at ω_1.
Depending on the duration Δt of the RF field (RF-pulse), the magnetization can be rotated by an arbitrary angle (flip angle $\alpha = \gamma B_1 \Delta t$) away from the longitudinal direction. An important example is the 90° pulse, which rotates the complete magnetization into the transverse plane [56, 114, 236, 275].

5.1.4 Relaxation

After the excitation RF-pulse has rotated the magnetization into the transverse plane, it will relax back until its equilibrium state $\boldsymbol{M}_0$, along the direction of the static $\boldsymbol{B_0}$-field, is restored. Here, one distinguishes between two different relaxation processes:
(1) The relaxation of the longitudinal magnetization M_z, which is characterized by the longitudinal or spin-lattice relaxation time T_1: To restore the equilibrium of $\boldsymbol{M_0}$ directed along the longitudinal $\boldsymbol{B_0}$-field, the magnetic moments constantly try to align with the external field through the exchange of energy with the surroundings, mostly by transferring energy to the object. This process is described as

$$\frac{dM_z}{dt} = \frac{M_0 - M_z}{T_1} \tag{5.13}$$

The solution to this equation is:

$$M_z(t) = M_0 + (M_z(0) - M_0)\exp(-t/T_1) \tag{5.14}$$

(2) The relaxation of the transverse magnetization M_{xy}, which is characterized by the transverse or spin-spin relaxation time T_2: All excited spins of the transverse magnetization M_{xy} point toward the same direction right after the excitation. Afterwards, however, some spin packets precess faster than others around the direction of the $\boldsymbol{B_0}$-field, because interactions between spins induce additional local fluctuating magnetic fields, which ultimately lead to a loss of

phase coherence, resulting in a decay of the transverse magnetization. The characterization of the overall rate of reduction in transverse magnetization is given by

$$\frac{dM_{xy}}{dt} = \frac{-M_{xy}}{T_2} \tag{5.15}$$

with solution

$$M_{xy}(t) = M_{xy}(0)\exp(-t/T_2). \tag{5.16}$$

In practice, magnetic field inhomogeneities due to technical deficiencies of the external field $\boldsymbol{B_0}$ also contribute to the process of transverse relaxation. This leads to an additional dephasing of the magnetization, characterized by a different decay time T_2'. The overall relaxation time T_2^*, considering all dephasing effects, is then always equal to or shorter than the real transverse relaxation time T_2 and given by

$$\frac{1}{T_2^*} = \frac{1}{T_2} + \frac{1}{T_2'}. \tag{5.17}$$

The loss of transverse magnetization due to T_2' is recoverable. The intrinsic T_2 losses are not recoverable as they are related to local, random, time-dependent field variations [56, 114, 236, 275].

5.1.5 Bloch equations

The Bloch equation, describing the evolution of the magnetization in the presence of a magnetic field, is obtained by combining the previous equations 5.7, 5.13 and 5.15:

$$\frac{d\boldsymbol{M}(t)}{dt} = \gamma \boldsymbol{M}(t) \times \boldsymbol{B_{ext}} + \frac{1}{T_1}(\boldsymbol{M_0} - \boldsymbol{M_z}) - \frac{1}{T_2}\boldsymbol{M_{xy}} \tag{5.18}$$

The complete set of solutions for the three components is given by:

$$\begin{aligned} M_x(t) &= \exp(-t/T_2)\ (M_x(0)\ \cos(\omega_0 t) + M_y(0)\ \sin(\omega_0 t)) \\ M_y(t) &= \exp(-t/T_2)\ (M_y(0)\ \cos(\omega_0 t) + M_x(0)\ \sin(\omega_0 t)) \\ M_z(t) &= M_0 + (M_z(0) - M_0)\ \exp(-t/T_1) \end{aligned} \tag{5.19}$$

The equilibrium solutions for each component of the magnetization are given for $t \to \infty$ by $M_x(\infty) = M_y(\infty) = 0$ and $M_z(\infty) = M_0$. The sinusoidal terms in the general solutions correspond to the precessional motion, previously explained in section 5.1.2; the prefactor characterizing the transverse relaxation effect is described in the section above [114, 236].

5.1.6 Spin echo and gradient echo sequences

In an MR experiment, the RF signal that is eventually measured comes from the transverse magnetization $M_{xy}(t)$. As it precesses in the magnetic field, it induces a signal which is measured in the receiver coils and ultimately forms a tomographic image. The observed oscillatory signal is called 'free induction decay' (FID), describing the decay of the transverse magnetization. Different MR experiments vary in the way the system is excited and prepared by means of RF pulses before the signal is read. A defined sequence of RF pulses is called a pulse sequence, which is usually repeated many times during the experiment [236].

Spin Echo

The classical spin-echo pulse sequence (Figure 5.1 left) utilizes the fact that the dephasing of the transverse magnetization $M_{xy}(t)$ caused by $\boldsymbol{B_0}$ inhomogeneities is reversible, whereas the influence of the fluctuating local magnetic fields is irreversible: Immediately after the 90° pulse, all components of the transverse magnetization $M_{xy}(t)$ point along the y-axis. Afterwards, different components precess faster or slower around the direction of the $\boldsymbol{B_0}$ field. In this way the initial phase coherence is lost [236].

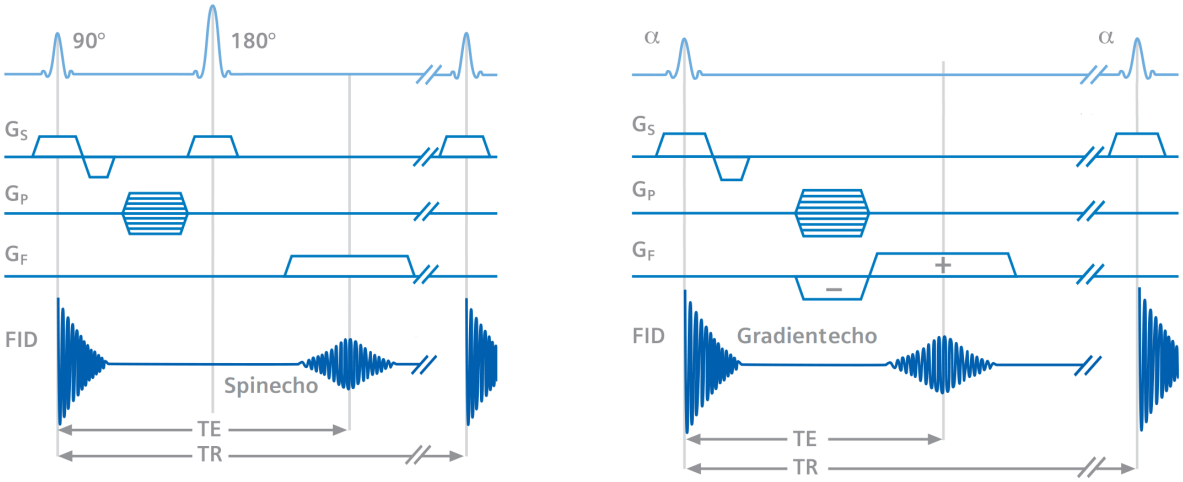

Figure 5.1: Schematic spin echo and gradient echo sequence: Left: Spin echo sequence with a pulse sequence of $90° - 180° - ACQ$. Right: Gradient echo sequence with a pulse sequence of $90° - G - ACQ$. G_S, G_P, G_F represent the slice-, phase-, and frequency-encoding gradient, respectively; adapted from [174].

When looking at this situation from a rotating frame, the different components of the magnetization fan out. If a 180° pulse is applied after a time delay $\frac{TE}{2}$ along the x-axis, the magnetization components will be mirrored with respect to the x-axis: the rotational direction of the components stays the same, but due to the inversion, faster components now follow slower ones. At a time $TE = 2 \cdot \frac{TE}{2}$, all magnetization components again point in the same direction. The important effect of the 180°-RF-pulse is thus a rephasing of the dephased transverse magnetization, which causes the MR signal to increase and to generate eventually a spin echo [236].

Gradient Echo

Images in which the acquired signal is directly the FID signal are often referred to as gradient echo (GRE) images [54]. In contrast to spin echo, only one RF pulse is used and the FID signal is manipulated by a magnetic field

$$\Delta B(x) = Gx, \tag{5.20}$$

which is superimposed onto the static magnetic field for the generation of a gradient echo. This gradient causes a calibrated change in local magnetic fields and hence alters the precession frequencies across the subject, resulting in an accelerated dephasing. A rephasing gradient is applied with the same strength but opposite polarity to the dephasing gradient, reversing the

phase scramble and generating a gradient echo. The gradient reversal refocuses only those spins that have been dephased by action of the gradient itself, i.e. phase shifts resulting from local magnetic field inhomogeneities or static tissue susceptibility gradients are not refocused and lead to signal decay governed by T_2^*. Thus, GRE images are generally more prone to artifacts. However, T_2^*-sensitivity of GRE imaging can also be beneficial and used to generate T_2^*-contrast used in functional MRI (fMRI) where changes in blood oxygenation, which lead to alterations in T_2^*, are used to analyze brain activation (see section 5.2) [180, 275].
GRE echo-planar-imaging (EPI) sequences in the single-shot mode are one of the most used sequences to acquire T_2^*-weighted images of functional changes in brain activity. A schematic depiction of a gradient echo sequence with the EPI readout is given in Figure 5.2. After the RF-pulse, the frequency-encoding gradient is applied with negative polarity, leading to dephasing of the spins, followed by the same gradient with opposite polarity. This reverses the dephasing and the spins get rephased again, leading to an echo formation. In EPI readout, the polarity of the frequency-encoding gradient is continuously alternated for the readout of the signal. With EPI sequences the total information required to reconstruct a 2D image can be sampled in the order of 50 ms, making it particularly suitable for imaging brain dynamics indicated by BOLD changes [56].

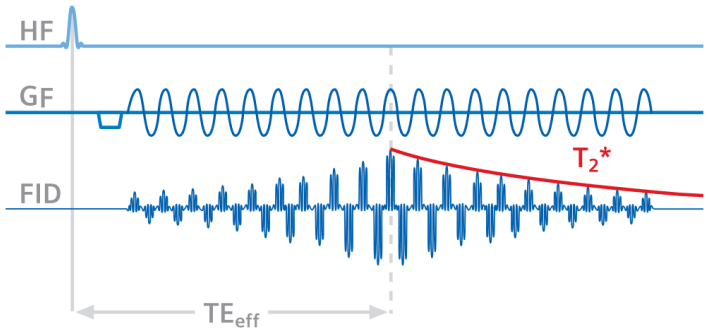

Figure 5.2: Schematic echo planar imaging (EPI) with the EPI-readout train in the frequency-encoding gradient; adapted from [174].

5.1.7 Imaging

The task of MR *imaging* now is to allocate the single signal contribution from the overall detected signal to each small volume element of the imaged object and present it in form of sectional images, referred to as tomograms. This is usually done with the help of additional magnetic gradient fields which are superimposed onto the homogeneous magnetic field $\boldsymbol{B_0}$. For spatial encoding these magnetic fields show a well-defined dependence on the spatial position. For selective excitation of the nuclear spins in a partial volume of interest, a slice selection gradient is applied. For position encoding within this slice two gradients in the other two directions have to be present so that the exact position of the image can be obtained in all three directions in space. This can be achieved by frequency and phase encoding of the MR signal. In this way, the Larmor frequency of the MR signal becomes a function of space and the spatial images can be collected to reconstruct the final image. Typical values for the magnitude of the imaging gradients are between 1 and 50 mT/m.
The concepts of spatial encoding techniques and image reconstruction for MRI can be found in e.g. Callaghan et al. [56].

5.2 The BOLD hemodynamic response

5.2.1 BOLD effect basics

The underlying effects of the BOLD signal generation involves several physiological quantities but depend primarily on the changes in local deoxyhemoglobin (Hb) concentration, changes of cerebral blood flow (CBF) and volume (CBV) as well as the cerebral metabolic rate of oxygen ($CMRO_2$). The BOLD signal generation is a complex interaction of different effects on the physiological level and the involved physics [214]. Therefore, the BOLD signal is only an indirect measure of the neuronal response conveyed by the hemodynamic response and consequently, only indirect conclusions about the underlying neuronal activation can be drawn from fMRI measurements [54, 63, 214].

For the brain to function, an uninterrupted supply of oxygen and glucose must be provided, which is ensured by a consistent CBF. When a specific brain region is active, the increased neuronal activity leads to an increased glucose and oxygen demand. As a result, the correlated blood flow and volume increase as well to satisfy the needs of the metabolism. Most oxygen in the blood is bound to the hemoglobin molecule which carries the oxygen (HbO_2).
Depending on the CBF through tissue and the amount of extracted and metabolized oxygen, the oxygenation state of blood changes. At rest, an equilibrium between the CBF and the fraction of extracted oxygen is established in the brain, which is disturbed upon activation. The net oxygen extraction fraction (OEF) describes the balance between oxygen supply (CBF of arterial O_2, $[O_2]_{art}$) and demand ($CMRO_2$) is defined as follows,

$$OEF = \frac{rate\ of\ consumption}{rate\ of\ delivery} = \frac{CMRO_2}{CBF[O_2]_{art}} \tag{5.21}$$

With increased neuronal activity, the metabolic rate of oxygen in the brain region increases as well, resulting in a local increase in CBF, which is referred to as the hemodynamic response. For reasons not fully understood yet, oxygen supply exceeds demand, which results in a net increase in local oxygenation for several seconds: As an overall result, when the blood flow increases, the OEF (equation 5.21) decreases. Increased blood oxygenation in areas of brain activation as a final net result then arises from the imbalance of an increased amount of oxygen distributed by the blood flow while less oxygen is extracted.

The blood oxygenation is determined by the ratio of the oxygen carrying oxyhemoglobin [HbO_2] and deoxygenated hemoglobin [dHb] from which the oxygen was extracted:

$$[dHb] = OEF \cdot [Hb] \tag{5.22}$$

The BOLD contrast, measured in fMRI, depends on the total amount of deoxygenated hemoglobin present in a brain region. Oxyhemoglobin has no unpaired electrons, is therefore weakly diamagnetic and indistinguishable from brain tissue. When hemoglobin transits to deoxyhemoglobin, which has four unpaired electrons exposed at each iron center, it becomes strongly paramagnetic, changing the susceptibility χ of blood,

$$\Delta\chi \propto [dHb] \tag{5.23}$$

which in turn induces local gradients ΔB in the magnetic field whose strength depends on the susceptibility changes induced by the deoxygenated hemoglobin concentration [104]:

$$\Delta B \propto \Delta\chi \cdot B_0 \tag{5.24}$$

This has the effect of dephasing the signal, causing destructive interference in the observed MR signal: relaxation times T2 and T2* decrease as the fraction of deoxyhemoglobin increases. The BOLD signal is seen as an increase in the MR signal that corresponds to a decrease in the concentration of deoxyhemoglobin. Consequently, T2- or T2*-weighted MRI sequences are able to capture the BOLD contrast and thereby indirectly visualize neuronal activity driven by the hemodynamic response [54, 63, 104, 129, 225]. Since changes in the vascular susceptibility modify $1/T_2'$ but not $1/T_2$, activation induced changes in T_2^* are the primary nuclear magnetic resonance effect of blood oxygenation and can be entirely expressed by changes in $1/T_2'$,

$$\Delta R_2^* = \Delta R_2' \tag{5.25}$$

with R_2^* and R_2' being the reciprocal of the relaxation times, the relaxation rates [54, 104].

Susceptibility differences between blood vessels and the surrounding tissue create local magnetic field distortions, which in turn modulate the signal of intravascular as well as extravascular compartments. Thus, BOLD contrast induced by [dHb] arises jointly from both components in and around blood vessels [63].
Looking at extravascular spins in the absence of spin diffusion, this causes intravoxel dephasing and is most prominent near larger veins. These effects scale linearly with the magnitude of the field perturbations ΔB [63],

$$\Delta R_2' = k \cdot V \cdot \Delta B \tag{5.26}$$

where k is a proportionality constant and V is the vascular volume fraction CBV. If spin diffusion is present, the simple dependency of R_2' changes to

$$\Delta R_2' = k \cdot V \cdot (\Delta B)^\beta \tag{5.27}$$

where $\beta = 1.5$ is accounting for a mixture between static dephasing ($\beta = 1$) and diffusing spins ($\beta = 2$). The proportionality constant k is now dependent on the tissue structure, vessel sizes inside and the geometry [23, 63].

5.2.2 BOLD model by Davis

In 1998, Davis et al. [75] introduced a model for the BOLD effect that relates the underlying physiological variables to the observed signal change. Let

$$S = S_0 \cdot e^{-TE \cdot R_2^*} \tag{5.28}$$

be the modeled MR signal with R_2^* being the transverse relaxation rate and let the subscripts 'a' and 'b' describe the activated and baseline conditions, respectively. Assuming that, compared to baseline (S_b), with activation (S_a) equation 5.25 holds, i.e. $\Delta R_2^* = \Delta R_2'$, the BOLD signal change can be written as

$$\frac{\Delta S}{S_b} = \frac{S_a - S_b}{S_b} = e^{-\Delta R_2' \cdot TE} - 1 \approx -\Delta R_2' \cdot TE \tag{5.29}$$

Combining all previous effects, the BOLD signal can be modeled in one single equation,

$$\begin{aligned} \frac{\Delta S}{S_b} &\approx -k \cdot TE(V_a \cdot [B_0 \cdot OEF_a]^\beta - V_b \cdot [B_0 \cdot OEF_b]^\beta) = \\ &= K \left[1 - \frac{V_a}{V_b} \cdot \left(\frac{OEF_a}{OEF_b}\right)^\beta\right] \\ &with \quad K = k \cdot TE \cdot V_b \cdot [B_0 \cdot OEF_b]^\beta \end{aligned} \tag{5.30}$$

describing the signal change due to the neuronal activation.

5.2.3 Properties of the hemodynamic response function (HRF)

A typical course of a hemodynamic response to a brief stimulus is displayed in Figure 5.3 and follows a distinct series of phases: The first phase (not shown in Figure 5.3) is called the 'initial dip' or 'pre-undershoot' and is of 1–2 s duration resulting in a negative observed BOLD response which has been attributed to an initial increase in the amount of deoxygenated hemoglobin. In fMRI analysis this is usually ignored when modeling the HRF. After 1–2 s an increased inflow of oxygenated blood accompanied by the overcompensation in blood flow dilutes the deoxyhemoglobin concentration and shifts the balance towards oxyhemoglobin rising to a peak in BOLD signal at about 5 s after a stimulus. After its peak, the BOLD signal decreases in amplitude below the baseline level. This 'post stimulus-undershoot' can last as long as 30 s and arises due to a combination of biophysical and metabolic effects.

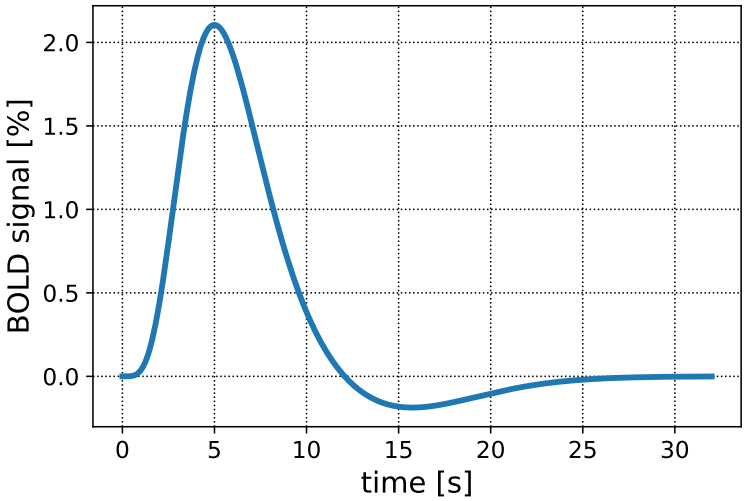

Figure 5.3: Typical shape of an HRF with a peak at about 5 s.

Intrinsic properties of the hemodynamic response, and therefore also of the BOLD signal, include the following features: First, as can be seen in Figure 5.3, the hemodynamic response is rather sluggish and therefore acts as a low pass filter. Whereas neuronal activity may only last milliseconds, the increase in blood flow that follows this activity takes about 5 s to reach its maximum. The temporal resolution of fMRI is therefore ultimately limited by the hemodynamic response time, blurring the temporal profiles of the underlying processes. Whereas neuronal responses occur within tens of milliseconds after a sensory stimulus, the hemodynamic response always lags the event. Second, the overall magnitude of the signal change is very small, i.e. 0.1–5 %. Third, to a first approximation, the hemodynamic response can be characterized by a linear, time-invariant system with the following three properties: Scaling (amplitude changes are proportional to the (presumed) amplitude changes of neuronal activity), superposition (the responses to two individual stimuli applied together will be sum of the individual responses) and time-invariance (if a stimulus is shifted by an time τ, then the response must also be shifted by exactly τ) [128, 211].

To create an estimated time course of hemodynamic signals which would be expected given

some particular experimental time course of neuronal activity, the stimulus function $s(t)$ must be convolved with the HRF. This estimated response is then later used in the analysis pipeline as a task-related regressor in the design matrix of the statistical model (see Chapter 6). Various models for the hemodynamic response function have been proposed, e.g., gamma-variate functions, 'Volterra' kernels, 'Balloon' model or 'Windkessel'-based models [95]. Most commonly in fMRI analysis, the hemodynamic response $h(t)$ is taken as a canonical hemodynamic response function (Figure 5.3) modeled by a gamma-variate [63, 81, 165, 219, 239]. Therefore, the relationship between the stimulus and BOLD response is given as follows, where the signal $y(t)$ at time t, is modeled as the convolution of two functions, i.e., a stimulus function $s(t)$ and the hemodynamic response $h(t)$,

$$y(t) = s(t) * h(t) \tag{5.31}$$

with $h(t)$ often being a linear combination of two Gamma functions,

$$h(t) = A\left(\frac{t^{\alpha_1-1}\beta_1^{\alpha_1}e^{-\beta_1 t}}{\Gamma(\alpha_1)} - c\frac{t^{\alpha_2-1}\beta_2^{\alpha_2}e^{-\beta_2 t}}{\Gamma(\alpha_2)}\right) \tag{5.32}$$

where $\alpha_1 = 6$, $\alpha_2 = 16$, $\beta_1 = \beta_2 = 1$ and c $= 1/6$ are parameters shaping the specific form of the HRF, e.g., broader peak, no undershoot etc. Here Γ represents the gamma function, which acts as a normalizing parameter, and the only unknown parameter in the model is the amplitude A [104, 129, 144, 211, 225, 234, 241].

Departures from the linearity assumption have been observed when the stimuli occur extremely rapidly, i.e., the interstimulus interval (ISI) is smaller than 2–5 s. Then the hemodynamic response has an overall lower amplitude and its peak is shifted, occurring slightly after the typical 5–6 s, compared to a single, isolated stimulus [49, 128, 211, 294]. Nonlinearity in BOLD responses can come from a number of sources which are still incompletely understood today. The two presumed dominant sources of nonlinearity include the intrinsic vascular properties of the blood vessels as well as neuronal processes, such as the adaptive behavior of neuronal activity. Adaptive mechanisms such as effects of habituation and sensitization can occur at the single neuron level as well as on psychological level, learning e.g. strategies to shift the attention away from painful stimuli [49][294]. At the single neuron level, the firing in response to stimulation varies over time and is usually not a linear or time-invariant function of the stimulus intensity, so the relation between neuronal response and stimulus/task parameters is not linear. Several studies have pointed out that nonlinear effects may also differ among brain regions [294].

Results from several fMRI datasets have revealed extensive variations in the HRF across scanning sessions, tasks, physiological modulations and populations. Whereas the hemodynamic response seems to be reasonably stable within subjects, the greatest variability is seen in the delay of the response across different brain regions in the order of seconds. This relatively wide range of response delays has been attributed to the vasculature of different regions and associated delayed flow of oxygenated blood through e.g. large veins draining the sites of neuronal activation. The exact sources of variance in hemodynamic response timing is presently unclear and research is still ongoing. Due to insufficient knowledge of the exact processes of hemodynamic coupling there is currently no gold standard for human brain activation. Determining the exact relationship between neuronal activity and fMRI activation, however, is complicated by the different dynamics of the neuronal activity involved and the properties of diverse stimuli [49, 85, 128, 129, 165, 219, 239, 241]. Several practical approaches taking possible deviations from linearity or vascular responses into account have been developed, e.g., the Volterra series

[94] or the balloon model [55]. These methods require fitting a large amount of parameters and therefore may not be practical for commonly performed fMRI experiments [211].

5.3 fMRI Preprocessing

fMRI is only an indirect measure of the underlying neuronal metabolic oxygen consumption, modeled through the hemodynamic response. Inevitably, several non-neuronal confounding sources of noise interfere with the measured signal, complicating the detection of the true underlying processes. The multiple sources of noise include the hardware (MRI scanner and associated hardware instability), gross subject movement (of the head), respiratory activity, heart beat or variations in baseline neuronal metabolism. As a result, uncorrected fMRI time series can show activity produced solely by spurious noise patterns which can lead to false conclusions. To remedy these shortcomings, a collectively termed 'preprocessing pipeline' has been proposed. This pipeline consists of several steps, each step removing or reducing structured noise to extract a signal which faithfully represents the underlying neuronal activity for further analysis. The majority of preprocessing steps are automatically performed within fMRI software packages, i.e. FSL, SPM or AFNI [63, 81, 104, 230, 281].

The next section briefly describes the most frequently employed steps of the preprocessing pipeline.

5.3.1 Distortion and slice timing correction

fMRI acquisitions may predominantly suffer from artifacts like signal loss especially near regions where air and tissue meet (most commonly regions in the anterior PFC and orbitofrontal cortex). These artifacts are due to inhomogeneities of B_0 caused by the susceptibility difference between two interfaces with different physical composition. Additionally, geometric distortions can occur. When gradients are applied to encode the spatial information in MRI, these inhomogeneities result in error in the location of structures in the resulting images and make it difficult to align functional with structural images. To correct for such arising distortions, hardware shimming and the additional acquisition of field maps, characterizing the B_0 field inhomogeneity, can be used. By obtaining complex-valued MR images at two different echo times, the difference in phase between the two images can be used to compute the local field inhomogeneity. These values can in turn be used to create a map quantifying the distance that each voxel has been shifted. By inverting this map, one can determine the original location of the data in each voxel [63, 131, 225].

Slice timing correction addresses the mismatch between the acquisition timing of different slices. fMRI data are usually obtained by using a 2D MRI acquisition technique which images one slice at a time. Slices are acquired in ascending/descending order or with an interleaved acquisition (e.g. 1,3,5...,2,4,6) design. Here, first the e.g. odd slices are acquired, followed by the even slices. As a result, different brain slices are acquired at systematically different times, depending on the TR. Correction for the difference in timing is usually done by temporal interpolation: The signal amplitude of each slice at a reference point is interpolated from neighboring TRs. A reference slice is chosen and the data in all other slices are interpolated to match the timing of the reference slice [63, 104, 225].

5.3.2 Motion correction

Especially with longer acquisition times and in patient populations (as opposed to healthy volunteers), motion is a common problem in clinical MRI. Although head immobilization techniques with foams and tapes try to prevent or diminish head movements during the scan in the first place, motion artifacts are mostly present, resulting in an unwanted mixing of signals from neighboring voxels. After each scan, the time series of motion parameters have to be visually inspected for drifts, displacement or rotation of the acquired image and data corrected accordingly or even discarded from further analysis if necessary [218].

Three core connected aspects are at the basis of the changes in the observed signal and therefore occurrence of motion-related artifacts. First, as the signal is proportional to the magnetization of the tissue, position changes due to e.g. head motion, alters the tissue composition and therefore the net magnetization at a specific location leading to an incorrect signal amplitude. Second, associated with the first issue, head movement changes the timing of different successive excited spins, leading to wrongly activated voxels over a period beyond the actual movement. Lastly, movements induce local magnetic field inhomogeneities which change local magnetic susceptibility gradients and lead to various artifacts such as image distortions or signal dropout, especially in regions at e.g. tissue surfaces [316].

To correct for subject motion that occurred during the scan, 'motion correction' is applied, which usually refers to the estimation of the rigid body movement parameters and the subsequent application of the estimated motion transformations to realign the time series of brain images, by using e.g., the 'MCFLIRT' tool, integrated in the FSL software package [135]. At each volume of the data the position of the head in space is estimated and all volumes are realigned to a reference image (usually first or middle one of the time series) using rigid body transformations. Rigid body transforms are given by the six parameters R = [X, Y, Z, pitch, yaw, roll], including three translational and three rotational parameters, to characterize the position of the head at each time point. Images are then resliced and voxel intensities are determined from an interpolation scheme using neighboring voxel values. The realignment parameters can then be condensed into a single summary estimate to indicate overall head displacement during the scan. Residual motion-related fluctuations in the data are then removed by a multiple linear regression with the six head motion parameters estimated from the rigid-body realignment as confound regressors. Additionally, their temporal derivatives as well as the squared versions of these are often included. Commonly used motion correction tools, beside MCFLIRT, include AIR [309] or statistical parametric mapping (SPM [96]) [67, 137, 230].

However, it has been shown [230, 246] that even with perfect correction, these approaches are often not capable of entirely removing the effects of motion. Additional techniques to correct for motion include temporal censoring operations, like spike regression or scrubbing, where contaminated volumes are excluded from the time series prior to further data analysis [68, 112, 230, 289]. Volumes are often identified as motion outliers by thresholding certain motion measurements based on the rigid-body parameters or signal change, e.g., framewise displacement (FD) [230] or DVARS [270]. 'DVARS' (where 'D' is referring to temporal derivative of time courses and 'VARS' referring to root-mean-square of the variance over voxels) and FD, are metrics defined to provide a single estimated head motion parameter for each time point [270]. FD indicates the position changes from frame to frame and is derived from the rigid-body

realignment parameters. The value of FD is defined as follows,

$$FD_i = |\Delta d_{ix}| + |\Delta d_{iy}| + |\Delta d_{iz}| + |\Delta \alpha_i| + |\Delta \beta_i| + |\Delta \gamma_i| \tag{5.33}$$

where the derivative is given by e.g. $\Delta d_{ix} = d_{(i-1)x} - d_{ix}$ and similarly for all other rigid body parameters $[d_{ix}, d_{iy}, d_{iz}, \alpha_i, \beta_i, \gamma_i]$. A sphere with radius $r = 50$ mm is used to calculate the rotational displacements on its surface to convert from degrees to millimeters [230, 267].
DVARS is defined as the root mean square of the temporal change of the fMRI voxel-wise signal at each time point [270]. It is calculated by first differentiating the measured fMRI time series (by backwards difference) and then calculating the RMS signal change over the whole brain. Comparisons to previous timepoints then indicate the intensity change from one brain image to the next (in contrast to the global signal, which is the average value of a brain image at a timepoint). Values of 0.5 for FD and 0.5 % Δ BOLD for DVARS are often used, but are dependent on the data set. To clean the data from the identified confounding spikes, regressors with non-zero values at each identified time point as well as its preceding and following timepoint are created and regressed out [230, 246, 316].

Combining motion regression and scrubbing approaches was shown to have the most considerable reduction in motion-related artifacts, although the ideal number of nuisance regressors is not known and dependent on each individual obtained dataset. Despite all correction methods, residual components of motion-related artifacts often still remain in the data. Hutchison et al. [130] noted, that residual nuisance effects “inevitably remain” in the BOLD time series and must therefore always be considered as contributor of unwanted signal in the reporting and interpretation of the results [67, 68, 81, 83, 104, 137, 149, 205, 218, 230, 289, 314, 316].

5.3.3 Registration and spatial normalization

The goal of spatial registration or normalization is to normalize each individual brain to a template (e.g., Talairach [278] or Montreal Neurological Institute (MNI) [84]) in order to generalize across individual brains and reduce variability between them to allow for meaningful group analysis. Normalization is implemented as a multistep method, first co-registering functional and structural images and then registering the high-resolution image to a high-resolution template. Preprocessing of the anatomical images prior to normalization in turn include bias field correction, brain extraction (BET) or skull stripping and tissue segmentation which vary between different software packages. Spatial normalization can be e.g. volume, landmark or surface-based, though surface-based registration gives a slightly more accurate result than low-dimensional volume-based registration [89]. Normalization and co-registration steps are largely automated in the i.e. FreeSurfer software package [63, 99, 145, 225].

5.3.4 Spatial and temporal filtering

Spatial and temporal preprocessing techniques involve the application of different filters to the images to foremost remove noisy frequencies to improve the signal-to-noise ratio (SNR) in the datasets. The most common approach to spatial smoothing is the convolution of the three-dimensional image with a three-dimensional Gaussian filter. The amount of smoothing imposed by a Gaussian kernel is determined by the width of the distribution, the full width at half-maximum (FWHM). The larger the FWHM, the greater the smoothing. A range of 4 mm to 8 mm kernel size is commonly applied.
The application of temporal filtering include low-, band-, or high-pass filters to reduce the

contributions of unwanted, noisy frequency ranges to improve the SNR. A standard type of applied temporal filtering in most fMRI analysis is e.g. the so called 'detrending'. Here, a high-pass filter removes the slow linear signal increase which is usually caused by the scanner drift due to hardware instability [63, 81, 104, 225].

5.3.5 Physiological noise correction: Independent component analysis (ICA) and principal component analysis (PCA)

A significant part of artifacts in fMRI result from cardiac and respiratory-related physiological processes, which are especially difficult to correct for retrospectively [81]. Blind signal separation techniques, such as e.g., ICA, have been found to effectively identify non-neuronal sources of variability and were first used for fMRI data by McKeown et al. [190].
The basic assumption of ICA is, that the data is a linear superposition of statistically independent processes and can therefore be modeled as

$$X_{jt} = \sum_{k=1}^{K} M_{jk} C_{kt} \tag{5.34}$$

where $\mathbf{X}$ is the measured fMRI signal space-time matrix of $j = \{1, ..., J\}$ voxels and $t = \{1, ..., T\}$ time samples. $\mathbf{M}$ is the so-called mixing matrix and $\mathbf{C}$ contains the K independent components. Iteratively, the ICA algorithm finds the so-called unmixing matrix $\mathbf{W}$ to calculate the individual components,

$$C_{tj} = \sum_{k=1}^{K} W_{tk} X_{kj} \tag{5.35}$$

with which the data X' can then be reconstructed from the independent components by

$$X'_{jt} = \sum_{k=1}^{K} W_{tk}^{-1} C_{kj}. \tag{5.36}$$

ICA returns a set of components along with an unmixing matrix that denotes the contribution of each spatial pattern to the observed signal at each timepoint. Ideally, some components then purely reflect BOLD signals, others artifactual processes. Once a set of artifactual components is identified, based on both the spatial and temporal characteristics, those components can be removed from the data, creating a "cleaned" dataset. Automatic ICA-based denoising techniques have been developed, e.g. FMRIB's ICA-based X-noiseifier (FIX), which once trained, (semi-) automatically identifies artifacts and removes the artifactual components in the dataset [63, 112, 142, 189, 225, 230, 237, 281].

Most neuroimaging studies either use ICA or PCA, or often a combination of both, for dimensionality and variation reduction of fMRI data. PCA is based on singular value decomposition (SVD) for a matrix $\mathbf{X}$ given in matrix notation by

$$\boldsymbol{X} = \boldsymbol{U}\boldsymbol{S}\boldsymbol{V}^{\mathsf{T}} \tag{5.37}$$

with $\mathbf{U}$ being a orthogonal matrix, $\mathbf{V}$ being unitary and $\mathbf{S}$ containing real, nonnegative diagonal elements. The matrices satisfy the following equations, $\boldsymbol{M}\boldsymbol{M}^{\mathsf{T}} = \boldsymbol{U}\boldsymbol{S}^2\boldsymbol{U}^{\mathsf{T}}$ and $\boldsymbol{M}^{\mathsf{T}}\boldsymbol{M} = \boldsymbol{V}\boldsymbol{S}^2\boldsymbol{V}^{\mathsf{T}}$ and are hermitian. The diagonal elements of $\boldsymbol{S}^2$ are the eigenvalues with $\mathbf{U}$ and $\mathbf{V}$ being the corresponding matrices of eigenvectors for $\boldsymbol{M}\boldsymbol{M}^{\mathsf{T}}$ and $\boldsymbol{M}^{\mathsf{T}}\boldsymbol{M}$. The matrix $\mathbf{P}$, which

contains the principal components, is then obtained by postmultiplying **U** by **S**. PCA finds a set of components (eigenimages) that are orthogonal to one another in multidimensional space. In contrast to ICA, for PCA there is inherent order of the components, i.e. the principal components (PC) are generated in order of decreasing variance explained. The first principal component therefore captures the greatest amount of variance and each successive component the greatest amount of residual variance, corresponding to non-systematic structures, e.g. noise, in the last components of the analysis. PCA thus transforms the data to a new coordinate system defined by the directions of largest variance of the data [7, 63, 142, 218, 225, 242, 243, 281, 319].

6 Statistical analysis

This chapter defines the concept of functional connectivity along with the metric with which it is measured (section 6.1), followed by the description of the sliding-window approach applied to dynamic functional connectivity investigations in section 6.2. Next, a short overview of the statistical analysis employed in fMRI analysis is given: from the general linear model (GLM) to more advanced linear mixed effects models (LME) in section 6.3. A more detailed description of the theoretical background on the statistical analysis can be found in Bernal et al. [37] and Witkovsky et al. [307].

6.1 Functional connectivity

To identify 'communications' between individual brain regions, correlations between the BOLD signal time series of brain regions are measured. This is referred to as 'functional connectivity' (FC). FC examines the functional co-activation between two or more spatially or anatomically distinct regions of the brain, i.e. whether activation in those regions correlates over time. Compared to 'effective connectivity', FC does not indicate any causal relationships, nor does it indicate any structural or physical connections. Several different metrics have been investigated to quantify the statistical dependence among BOLD time series of different brain regions, including covariance, mutual information, transfer entropy or Granger causality. The most common metric to indicate FC is the Pearson correlation coefficient, which is a non-directed measure of interaction, measuring the linear relationship between two random variables [6, 33, 207, 225, 297].

If two regions are functionally connected, they show similarly varying levels of activity, i.e. temporal synchrony between their time series. For two simultaneously obtained time series $x = (x_1, ..., x_N)$ and $y = (y_1, ..., y_N)$ with $i = 1, ..., N$ timepoints the Pearson correlation coefficient is calculated as

$$r = \frac{\sum_{i=1}^{N}(x_i - \bar{x})(y_i - \bar{y})}{\sqrt{\sum_{i=1}^{N}(x_i - \bar{x})^2 \sum_{i=1}^{N}(y_i - \bar{y})^2}} \tag{6.1}$$

where $\bar{x}$ and $\bar{y}$ denote the means of the two time series x and y, respectively. Hence, r is defined over the interval [-1,1], where $r = -1$ corresponds to a perfect anti-correlation, $r = 0$ indicates no correlation between the two variables and $r = 1$ implies a perfect positive correlation [126, 233, 237, 269].

Conventional seed-based or resting-state functional connectivity approaches most commonly derive connectivity information from the whole length of the BOLD time series which results in a stationary, time-averaged representation of the functional coupling between brain voxels or areas. However, dynamic changes of brain network activity occur at many temporal scales, from milliseconds to seconds, and other strategies have been used to take full advantage of

the temporal information contained in the FC data. Since functional coupling between brain regions is non-stationary over time within individuals, the most common approach to assess dynamic FC changes over a period is the so-called sliding-window analysis [126, 130, 161, 207].

6.2 Sliding-window analysis

In a sliding-window approach, a predefined time window of fixed length is selected, and the correlation coefficient between the two signals (BOLD fMRI time series, indicated by $t1$ and $t2$ in Figure 6.1) of interest within that window is computed. The window is then 'slided' forward in time by some offset (with possible overlap) and the process is repeated over consecutive windowed segments until the end of the time series is reached. In this way, the time-varying behavior of the chosen metric (e.g. Pearson correlation coefficient) is quantified over the duration of the fMRI scan by a time series of FC correlation values. This method is rather computationally expensive and is sensitive to the chosen window parameters, such as window length, offset and overlap [33, 50, 60, 92, 115, 126, 130, 161, 242].

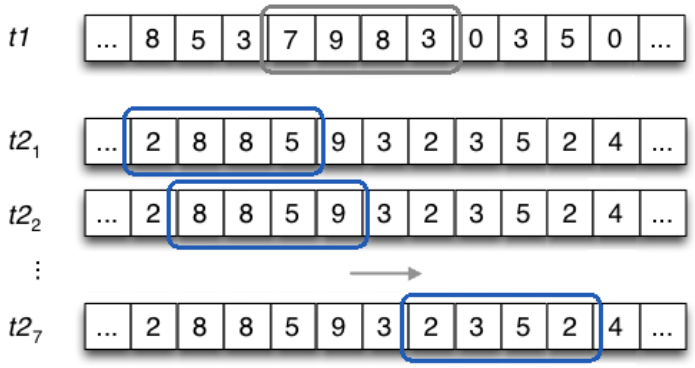

Figure 6.1: Schematic illustration of a sliding-window approach with two time series $t1$ and $t2$ of size N shifted against each other with window length $ws = 4$ and minimal overlap $o = 1$. Correlation calculations are calculated between the shown grey window of time series $t1$ and each single blue window (seven in total) of time series $t2$, before the grey window in time series $t1$ would be shifted further along. The obtained matrix of time series is then of size N×7, corresponding to one correlation time series for each of the seven overlaps; adapted from [132].

The biggest challenge in sliding-window analysis is the identification of an appropriate size of the window, as it has a substantial effect on the amount of time series variability captured by the sliding-window. As there is no ground truth in the fMRI data, the exact dynamics, timings of events and number of states are all unknown. The average duration of a real brain 'state' is not known and the BOLD response maximum lies delayed somewhere between five and seven seconds [165]. Finding the 'optimal' window length to capture the relevant neurological processes is a challenging task and no study has convincingly identified the optimal window length for dynamic FC analysis – or determined if there even is one. The 'optimal' window length depends on different external and internal factors, including the temporal resolution of the fMRI scanning sequence, the performed cognitive task during the experiment, as well as the physiological processing on cerebral level [242]. In principle for FC analysis, the size of the sliding-window should be able to resolve the lowest frequencies of interest in the

measured signal, as well as detect more rapid transitions between states on smaller timescales, i.e. capture both discrete and smoothly varying changes in the connectivity, without giving a time-averaged value over a long time period, suppressing potential interesting dynamics [242]. If only a small number of data points is included in the computation of the FC estimation, the signal-to-noise ratio (SNR) decreases, as few time points are available for the calculation and higher frequencies of the signal dominate the estimate. On the other hand, smaller window lengths offer higher temporal resolution and are more sensitive in capturing the dynamic changes in the FC of the time series. To avoid spurious variability in the FC estimate due to non-neuronal signal, a robust window length for resting-state fMRI analysis of 30 s is often used [63, 130, 161, 207, 232, 266].

An additional challenge is the variability of the FC measurements in and between-sessions, which is further complicated by non-stationary noise of the fMRI acquisitions. It has been shown that FC measurements vary within one subject, between different sessions as well as within single fMRI sessions [290]. Observed differences hereby include FC changes in strength and directionality, increasing the difficulty to analyse and interpret temporal variations in FC metrics happening on different timescales over fMRI time series [115]. Despite thorough preprocessing techniques trying to reduce or eliminate the introduced confounding factors, residuals from non-stationary noise may still remain in the data. The appropriate preprocessing, the neuronally relevant frequencies and the appropriate time scale for studying connectivity changes are presently open questions of research [4, 60, 130, 161, 205].

6.3 Linear mixed effects model (LME)

The typical statistical analysis of functional MRI studies include the comparison of the measured fMRI data against a hypothesized model based upon the known cognitive task that is performed during the scan. Voxel, cluster or region based inference can be drawn and the formulated hypotheses accepted or rejected based on the statistical threshold of significance. In this way, brain voxels responding to different conditions of a task, e.g., high pain states versus low pain states, are identified and assigned to individual activity maps. Hence, for each condition a corresponding brain map with significant condition-associated voxels is created and can be further analyzed and interpreted [63].

GLM

Since the introduction of the GLM to the neuroimaging community in 1995, the GLM analysis has established itself as the standard statistical model for fMRI analysis to examine the temporal synchrony between experimental observations and the predicted responses [96]. The GLM aims to explain the variation of a dependent, or response variable (measured fMRI data matrix) in terms of a weighted sum of several predictors (corresponding to the different experimental conditions) in order to detect task-related brain activity.

The GLM can be written in matrix notation as

$$\boldsymbol{Y} = \boldsymbol{X}\boldsymbol{\beta} + \boldsymbol{\epsilon} \quad \text{with} \quad \boldsymbol{\epsilon} \sim N(0, \sigma^2 \boldsymbol{I}) \tag{6.2}$$

where $\boldsymbol{Y}$ is the fMRI data matrix, $\boldsymbol{X}$ is the so-called design-matrix, $\boldsymbol{\beta}$ the model parameter matrix and $\boldsymbol{\epsilon}$ the matrix of error terms given by a normal distribution $N(0, \sigma^2 \boldsymbol{I})$ with mean

$\mu = 0$ and variance σ^2. By first left-multiplying both sides by $\boldsymbol{X}^\mathsf{T}$ the normal equations are obtained,

$$\boldsymbol{X}^\mathsf{T}\boldsymbol{Y} = \boldsymbol{X}^\mathsf{T}\boldsymbol{X}\boldsymbol{\beta} \tag{6.3}$$

and the best approximation $\hat{\boldsymbol{\beta}}$ can be obtained from the least squares solution

$$\hat{\boldsymbol{\beta}} = (\boldsymbol{X}^\mathsf{T}\boldsymbol{X})^{-1}\boldsymbol{X}^\mathsf{T}\boldsymbol{Y} \tag{6.4}$$

minimizing the sum-of-squares of the residual errors $\boldsymbol{\epsilon} = \boldsymbol{Y} - \hat{\boldsymbol{Y}}$, given by the difference between Y and the estimated signal $\hat{\boldsymbol{Y}} = \boldsymbol{X}\hat{\boldsymbol{\beta}}$. The $\hat{\boldsymbol{\beta}}$-weight of a condition predictor thus quantifies the contribution of its time course in explaining the voxel time course. The exact interpretation of β-values depends on the design matrix $\mathbf{X}$, where a large positive (negative) beta weight typically indicates that the voxel exhibits strong activation (deactivation) during the modeled experimental condition. All beta values together characterize a voxels 'preference' for one of more experimental conditions [34, 105, 136, 225, 226].

Mixed and random effects analysis

In order for group-level inference to generalize across the small population included in a study, results from individual subjects must be combined. Two common statistical approaches include fixed effects analysis and random effects analysis [97]. In a fixed effects analysis, all measured data points of each of the subjects are combined into a one analysis and single subject-level analysis is performed. The underlying assumption of this approach is that the experiment influences all subjects in the same manner and that therefore inter-subject variation is zero. The major drawback of this analysis is that conclusions are restricted to the investigated subjects and do not generalize across population. Random effects analysis is therefore more commonly applied in fMRI analysis. It accounts for the fact, that subjects are randomly drawn from a larger population of subjects and the investigated experiment or task leads to different responses for each individual. Typically, random effects analysis is carried out in two stages: first the subject-level, then the group-level. On stage one, first single subject statistics are calculated independently, followed by a significance testing of the individual summary statistics on the second- or group-level afterwards. The automatic analysis steps are available within various fMRI statistical toolboxes [63, 196, 200].

In current fMRI practice, most analyses treat the experimental manipulation as having fixed effects within individual but random effects across individual analyses, which leads to what is called a mixed-effects analysis [225]. The standard approach is then to include a mixture of within-subject or session fixed effects and across-subject or session random effects. Instead of using a two-level approach, an 'all-in-one' model can be used. This model directly estimates the parameter estimates $\hat{\boldsymbol{\beta}}$ at group-level from the full time series of all subjects conjointly, taking into account all fixed and random effects variance components. This is a major advantage compared to two-level models, as it can take differences in subject-specific parameter variances on group-level into account. A disadvantage can be the very large datasets, which are computationally challenging [62, 93, 201].

Linear mixed effects models are expressed by

$$\boldsymbol{Y} = \boldsymbol{X}\boldsymbol{\beta} + \boldsymbol{Z}\boldsymbol{u} + \boldsymbol{\epsilon}, \tag{6.5}$$

where $\boldsymbol{Y}$ is the n×1 response vector of observations, $\boldsymbol{X}$ is the n×p design matrix for the fixed effects $\boldsymbol{\beta}$, $\boldsymbol{Z}$ is the n×q design matrix for the random effects $\boldsymbol{u}$ and $\boldsymbol{\epsilon}$ is the n×1 vector of error. It is assumed that $\boldsymbol{u}$ and $\boldsymbol{\epsilon}$ follow a normal distribution

$$\begin{bmatrix} \boldsymbol{u} \\ \boldsymbol{\epsilon} \end{bmatrix} \sim N\left(\begin{bmatrix} \boldsymbol{0} \\ \boldsymbol{0} \end{bmatrix}, \begin{bmatrix} \boldsymbol{G} & \boldsymbol{0} \\ \boldsymbol{0} & \boldsymbol{R} \end{bmatrix} \right), \tag{6.6}$$

with mean $\boldsymbol{0}$ and $\boldsymbol{G}$ and $\boldsymbol{R}$ being the variance covariance matrices for $\boldsymbol{u}$ and $\boldsymbol{\epsilon}$, respectively. Hence

$$\boldsymbol{Y} \sim N(\boldsymbol{X\beta}, \boldsymbol{ZGZ}^\mathsf{T} + \boldsymbol{R}) \tag{6.7}$$

and

$$Var(\boldsymbol{Y}) = V = Var(\boldsymbol{Zu}) + Var(\boldsymbol{\epsilon}) = \boldsymbol{ZGZ}^\mathsf{T} + \boldsymbol{R} \tag{6.8}$$

where $\mathbf{R}$ is often assumed $\boldsymbol{R} = \sigma^2 \boldsymbol{I}_n$.

The central mixed model equations (MME) or Hendersons's equations [123]

$$\begin{bmatrix} \boldsymbol{X}^\mathsf{T}\boldsymbol{R}^{-1}\boldsymbol{X} & \boldsymbol{X}^\mathsf{T}\boldsymbol{R}^{-1}\boldsymbol{Z} \\ \boldsymbol{Z}^\mathsf{T}\boldsymbol{R}^{-1}\boldsymbol{X} & \boldsymbol{Z}^\mathsf{T}\boldsymbol{R}^{-1}\boldsymbol{Z} + \boldsymbol{G}^{-1} \end{bmatrix} \begin{bmatrix} \hat{\boldsymbol{\beta}} \\ \tilde{\boldsymbol{u}} \end{bmatrix} = \begin{bmatrix} \boldsymbol{X}^\mathsf{T}\boldsymbol{R}^{-1}\boldsymbol{y} \\ \boldsymbol{Z}^\mathsf{T}\boldsymbol{R}^{-1}\boldsymbol{y} \end{bmatrix} \tag{6.9}$$

are obtained by the $(\hat{\boldsymbol{\beta}}, \tilde{\boldsymbol{u}})$ that jointly maximize the log-density function of the joint distribution of $\boldsymbol{y}$ and $\boldsymbol{u}$ given by

$$l = -\frac{1}{2}\log|\boldsymbol{R}| - \frac{1}{2}(\boldsymbol{y} - \boldsymbol{X\beta} - \boldsymbol{Zu})^\mathsf{T}\boldsymbol{R}^{-1}(\boldsymbol{y} - \boldsymbol{X\beta} - \boldsymbol{Zu}) - \frac{1}{2}log|\boldsymbol{G}| - \boldsymbol{u}^\mathsf{T}\boldsymbol{G}^{-1}\boldsymbol{u} + const., \tag{6.10}$$

assuming $\boldsymbol{R}$ and $\boldsymbol{G}$ are known. This gives the best linear unbiased estimate for $\hat{\boldsymbol{\beta}}$ and best linear unbiased predictor for $\tilde{\boldsymbol{u}}$, analogous to the GLM:

$$\begin{aligned} \hat{\boldsymbol{\beta}} &= (\boldsymbol{X}^\mathsf{T}\boldsymbol{V}^{-1}\boldsymbol{X})^{-1}\boldsymbol{X}^\mathsf{T}\boldsymbol{V}^{-1}\boldsymbol{y} \\ \tilde{\boldsymbol{u}} &= \boldsymbol{GZ}^\mathsf{T}\boldsymbol{V}^{-1}(\boldsymbol{y} - \boldsymbol{X}\hat{\boldsymbol{\beta}}). \end{aligned} \tag{6.11}$$

The equations for calculating maximum likelihood estimators of variance components for fMRI data have to be solved with numerical iterative approaches, e.g., with the expectation maximization (EM) algorithm currently implemented in most statistical software (R, Python, Julia) [37, 97, 307].

Significance testing and correction for multiple testing

Statistical inference on fMRI data is usually done on voxel- or cluster-level. Hence, the chosen test statistic, e.g., t-statistic (given below) is evaluated either at each individual voxel or on certain clusters. Spatially continuous activated voxels are first defined as clusters, then the significance of each cluster is determined by measuring its size and then compared to some critical cluster size threshold, e.g., $\alpha = 0.01$ or $\alpha = 0.05$. If a certain statistical threshold calculated from the t-statistic is exceeded, the voxel or cluster is said to be significant [225]. The t-statistic

$$t = \frac{\boldsymbol{c}\hat{\boldsymbol{\beta}}}{\sqrt{\boldsymbol{c}(\boldsymbol{X}^\mathsf{T}\boldsymbol{X})^{-1}\boldsymbol{c}^\mathsf{T}\hat{\sigma}^2}} \tag{6.12}$$

with specified contrasts $\boldsymbol{c}$, 'contrasting' the $\hat{\boldsymbol{\beta}}$-estimates, and variance σ^2, is often used in fMRI analysis to carry out hypothesis testing and determine the significance of single voxels or clusters. As a result, a statistical parameter map is obtained indicating significance or non-significance for specific contrasts on a single voxel basis. From the t-statistics a p-value can then be obtained. For small p-values (high t-values) the null hypothesis H_0 (no effect of interest in the data) is usually rejected and the alternative hypothesis H_1 is accepted [175].

The so-called 'multiple-testing-' or 'comparison-problem' arises when a high number of statistical tests are simultaneously performed. In fMRI analysis, the statistical model is typically fit to each of the hundreds of thousands of voxels. To correct for false positive errors induced by multiple comparisons, several methods have been proposed e.g., the Familywise Error Rate (FWE, mostly controlled by Bonferroni correction) or False Discovery Rate (FDR). Other approaches, such as (non-)parametric permutation methods can also be applied to control for the FWE, but are computationally expensive [209]. For example, permutation approaches used in this work repeatedly resample the data sets under the null hypothesis and calculate the statistics from which the maximum across all voxels is extracted. In this way, an empirical null distribution for the maximum statistic is obtained and the percentile of interest (100(1-α)) is used to provide a statistical threshold which controls for multiple testing. Through random re-labeling of the data under the null hypothesis, the entire images can then be investigated for the quantity of interest [63, 164, 304, 305].

7 Machine learning in fMRI

This chapter gives a basic introduction to the theoretical background of machine learning methods with respect to the fMRI applications in Chapter 9.5. Two regression models are briefly introduced in section 7.1, followed by cross-validation schemes (section 7.2) and the performance measures (section 7.3) used in this work.

Machine learning is a data-driven technique that uses statistical methods to find complex patterns in large amounts of data. Applications to fMRI data are motivated by the ability of such methods to detect brain activity without a predefined model and use these cortical activity patterns to aid in diagnostic decisions, elucidate related brain activity to different cognitive states and identify pathologically related patterns to develop potential biomarkers for specific disorders [2].

The process of applying ML techniques to fMRI data can be divided into a general analysis pipeline of three major steps [2, 91, 142]: First, the relevant brain activity has to be extracted from the acquired BOLD fMRI time series and transformed to relevant features which enter the machine learning analysis. Second, using a subset of the data, one or several ML models are trained and the optimal parameters are obtained with respect to a predefined performance metric. Third, the performance of the ML model is tested on a new or not used (sub)data set to evaluate the generalisation accuracy, specified by some performance metric. The main advantage of ML methods applied to fMRI data is that they can offer higher sensitivity than their counterparts based on standard univariate statistics, due to being able to learn the likely complex manifestations of brain disorders in neuroimaging data. A major drawback of fMRI data when combined with ML approaches include the often obtained small sample size with a large number of noisy fMRI features [2, 173].

Machine learning approaches are typically divided into the two main subtypes of supervised and unsupervised learning. Supervised learning builds a model that predicts outputs from input data (e.g. classification and regression analysis), whereas unsupervised learning is concerned with finding structure in the data (e.g. clustering) [102]. In this work supervised models are used and therefore focused on in the following. Supervised machine learning refers to the subset of machine learning methods which derive models in the form of input-output relationships. The goal is to identify the mapping between labelled input variables and output variables on the basis of provided input features with corresponding target labels to generalize to unseen data with unknown labels.

Two commonly used supervised learning algorithms are linear/logistic regression and decision trees.

7.1 Regression models

7.1.1 Regularized linear models

A large class of supervised learning algorithms are based on regularized linear regression models. Compared to classical linear regression models (Equation 6.2), regularization (or "shrinkage") techniques add a penalty term in order to constrain or 'regularize' the coefficients which are estimated. In this way sensitivity to outliers, and hence the variance of the model, is reduced, leading to an improved prediction accuracy [102].
One of the most common regularization methods besides ridge regression is LASSO (Least Absolute Shrinkage and Selection Operator) [283]. Adding a penalty term $\Omega(\lambda, \boldsymbol{\beta})$ to the classic model leads to a penalized least squares (PLS) equation,

$$PLS(\lambda, \boldsymbol{\beta}) = (\boldsymbol{y} - \boldsymbol{X}\boldsymbol{\beta})^T(\boldsymbol{y} - \boldsymbol{X}\boldsymbol{\beta}) + \Omega(\lambda, \boldsymbol{\beta}) \tag{7.1}$$

with λ being a tuning parameter. If the tuning parameter λ is set to 0, $\lambda = 0$, then the ordinary least squares estimate is obtained. For LASSO the L_1 norm is imposed on the coefficients, i.e. the sum of the absolute values of the coefficients is restricted. The LASSO coefficients $\hat{\beta}_{LASSO}$ are then obtained from

$$\hat{\boldsymbol{\beta}}_{LASSO} = \underset{\boldsymbol{\beta}}{\operatorname{argmin}} \sum_{i=1}^{n}(y_i - \sum_{j=1}^{p} x_{ij}\beta_j)^2 + \lambda \sum_{j=1}^{p} |\beta_j|, \quad \lambda \geq 0 \tag{7.2}$$

7.1.2 Tree based models

In 1984 tree-based methods both for classification and regression analysis were introduced, as 'Classification and Regression Trees' (CART) [44]. For the prediction of a numerical value, regression trees are used and for categorical values classification trees are used [98].
A 'tree' is the visual representation of many binary 'if-then' decisions in the algorithm and is usually 'grown' upside down, from top to bottom. Starting with all observations in one so-called 'root' node, the trees grow downward, branching out, until in the endings one observation is left, in a so-called 'leaf' or terminal node. From the root node observations are placed into one of two descendant nodes (branches with 'child nodes'), using a split on a single input variable. At each split, every possible split on every feature is considered and the predictor and split combination giving the "best" value according to a certain metric is then used to partition the node. At each child node, the algorithm will decide whether to continue dividing. If it stops, the node is called a leaf node and it contains the final decision [121]. The most common splitting metric for regression trees is the sum of squared error (SSE) . If the data S is divided into two groups S_1 and S_2 for which the selection minimizes the sum of squared errors

$$SSE = \sum_{i \in S_1}(y_i - \bar{y}_1)^2 + \sum_{i \in S_2}(y_i - \bar{y}_2)^2 \tag{7.3}$$

where $\bar{y}_1$ and $\bar{y}_2$ are the average of the samples in S_1 and S_2. The same procedure is applied to all successive descendant nodes, which is also referred to as recursive partitioning: In a top-down 'greedy' fashion, the algorithm splits nodes at each step into two branches and chooses the best split at that particular step, rather than looking ahead and picking a split that leads to a better tree in general [142]. To remove sections that have little predictive power, 'pruning' is applied. The most common methods for pruning include setting a maximum tree depth or minimum number of samples per leaf. The trees then grow until one of the stopping criteria is

met, for example, all nodes contain fewer than some fixed number of cases, and then 'pruned' back to prevent overfitting. Once a tree is finished, it will have some non-partitioned nodes called terminal nodes. Predicted values in terminal nodes are obtained by averaging the response for regression problems [73].

Single decision tree models will generally suffer from high variance and low accuracy. To yield better prediction performances, an improved model is obtained by combining many trees, which is called ensembling. By incorporating the predictions of many different trees, an aggregated prediction generally yields an improved prediction accuracy compared to individual trees. The most common ensemble of trees methods are random forest and boosting machines [73]. Boosting is referred to as the combination of many weak learners (i.e. a single decision tree) to "boost" their performance in order to build a stronger model. Sequentially, as the first tree is split on the most predictive feature, weights are created to ensure that the subsequent tree splits on the feature that allows it to correctly classify the data points that were misclassified in the initial tree and so forth. Increased weights are then assigned to misclassified observations, while decreased weights are given to repeatedly correctly classified observations. In this way each model in the sequence is built to address the deficiencies of the previous models in the sequence. The final boosted predictions are then usually obtained as a weighted sum of all individual predictions. Gradient boosting is the most popular extension of boosting and uses the gradient descent algorithm for optimization [73, 98, 293].

The eXtreme gradient boosting (XGB), also known as 'regularized boosting', machine learning algorithm is a fast implementation of gradient boosted trees developed by Chen and Guestrin [64]. The goal of the learner is to make an accurate prediction $\hat{y}_i = \theta(\boldsymbol{x}_i)$ given $\boldsymbol{x}_i$ based on the data set $[(x_1, y_1), ..., (x_m, y_m)]$. The regularized objective function $O(\theta)$ is minimized to learn the set of functions f_k which are used to predict the outcome in the model and is given by

$$O(\theta) = \sum_i l(\hat{y}_i, y_i) + \sum_k \Omega(f_k) \tag{7.4}$$

with l describing the difference between the prediction $\hat{y}_i$ of the model and the true value y_i and

$$\Omega(f) = \gamma T + \frac{1}{2}\lambda \sum_{j=1}^{T} w_j^2 \tag{7.5}$$

being the regularization term which constrains the complexity of the model by introducing the regularization parameter λ on the learned weights w_j. T is the total number of leaves and γ is another weighting parameter.
The minimization of the objective function to find the optimal set of split values and leaf values for each tree is done in an additive, sequential manner. When $t-1$ trees have been optimized and the prediction $\hat{y_i}^t$ at tree t is next, one adds the f_t which maps x_i onto the right leaf and most improves the model $\hat{y_i}^t = \hat{y_i}^{t-1} + f_t(x_i)$ [64, 141, 155, 293].
To obtain a simplified objective at step t, the objective function can then be transformed from a sum over the training set to a sum over the leaves set

$$\tilde{O}^t \approx \sum_{j=1}^{T} [(\sum_{i \in I_j^t} g_i) w_j + \frac{1}{2}(\sum_{i \in I_j^t} h_i + \lambda) w_j^2] + \gamma T \tag{7.6}$$

with $I_j = \{i | f(x_i = w_j)\}$ mapping x_i to leaf j and g_i and h_i are the first and second order derivatives of the loss function.

From equation 7.6, the optimal weight w_j^* of leaf j and the corresponding best objective value can be calculated by

$$\tilde{O}^*(w_j^*) = -\frac{1}{2}\sum_{j=1}^{T}\frac{G_j^2}{H_j+\lambda} + \gamma T \tag{7.7}$$

with $G_j = \sum_{i\in I_j} g_i$ and $H_j = \sum_{i\in I_j} h_i$. The best tree structure is then found by sequentially splitting the features space, with each split loss reduction given by

$$O_{split} = \frac{1}{2}\left(\frac{G_L^2}{H_L+\lambda} + \frac{G_R^2}{H_R+\lambda} - \frac{G_R^2+G_L^2}{H_R+H_L\lambda}\right) - \gamma \tag{7.8}$$

with L and R indicating left or right node splits, respectively. In this way split candidates for the best split can be evaluated by the measure of fit improvement which is the difference between the scores of the new leaves after the split and the score of the previous leaf [293]. Full details of the exact derivatives of the algorithm can be found in the original publication of Chen et al. [64].

7.2 Cross-validation and resampling

To evaluate the accuracy of a predictive model which was trained on labeled, known data, its performance has to be measured on unknown data, to get an unbiased estimate. This is done by calculating the out-of sample error in order to evaluate the generalisability of the model to unseen, out-of sample data [160]. In a simple holdout strategy, the whole data set is divided into two different sets: the training and test set. The training set is generally then further split in two disjoint subsets, the training or learning set and the validation set. The training set is now solely used for fitting the model, i.e. to estimate the model (hyper-)parameters. Subsequently, the second subset is exclusively used for the purpose of assessing the estimated model performance or compare different models on an independent data set, hence validation set, before the most optimal model is chosen to be tested on the held-out test set [142].

However, when the learning sample is very small, subdividing the data further will yield an unreliable estimate. Additionally, the estimated generalisation error depends on the specific split and mostly the size of the subsets used for training, validation and testing. If too many data points are put in the validation set, few data points actually remain in the training set for the model to learn and hence will lack accuracy. On the other hand, if many observations are left in the training set with only few in the validation set, the model's variance of the estimated model error increases. With small data sets for example, more complex models may possibly better adjust to details in the data than simpler models, and will tend to overfit, i.e., will rather fit to the noise than to the underlying relationship of interest. As a result, while it perfectly performs in-sample, its out-of-sample performance is deteriorated and the model is said to have low bias, but high variance [160].
Both variance and bias should be minimal in a model. The main approach to handle the tradeoff between bias and variance is to adapt the complexity of the hypothesis space to the problem under consideration. By estimating the prediction error using cross-validation, meta-parameters controlling the complexity of the hypothesis space are selected, and especially if data are scarce, can provide good estimates for the generalisability of the model [287].

The most commonly applied resampling procedure in neuroimaging is k-fold cross-validation

(CV). It utilizes all data points for both training and validation through repeated holdout, yielding error estimates with much less variance than classic holdout. Explicitly, k-fold CV first splits the learning sample into k disjoint subsets of equal size (see Figure 7.1 for an schematic example for $k = 5$). Then, a model is inferred by the learning algorithm from each sample, trained k times, and its performance is determined on the held out sample. The average error of all k obtained single estimated model errors then represents the final performance estimate. When k is equal to the number of objects in the learning sample, this method is called leave-one-out cross-validation [98]. Typically, cross-validation schemes offer generalisation error estimates with relatively low bias, but with significant variability. Common recommendations to attain a good balance between bias and variance include 5-fold or 10-fold CV [121, 160].

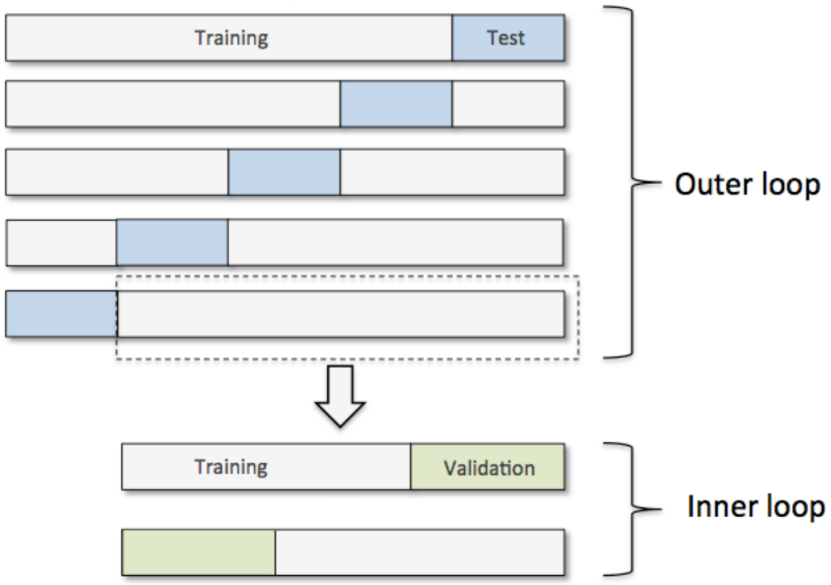

Figure 7.1: Schematic 5-fold cross-validation scheme: the data is split into five folds in the outer loop, of which four are constituting the training set and one the test set for each iteration. In the inner loop, training and validation sets are created from each outer training set, to tune hyperparameters. The errors of the five iterations are averaged to obtain the final performance estimation; adapted from [172].

7.3 Measuring performance

Common performance measurement metrics for regression models include the (Root) Mean Squared Error (RMSE/MSE) as an absolute measure,

$$RMSE = \sqrt{MSE} = \sqrt{\frac{1}{n}\sum_{i=1}^{n}(y_i - \bar{y}_i)^2} \tag{7.9}$$

and as a relative one the coefficient of determination or 'R-squared' (R^2),

$$R^2 = 1 - \frac{SS_{res}}{SS_{tot}} = 1 - \frac{\sum_{i=1}^{n}(y_i - \hat{y}_i)^2}{\sum_{i=1}^{n}(y_i - \bar{y})^2} \tag{7.10}$$

with $\bar{y}$ corresponding to the mean of the n datapoints y_i and $\hat{y}_i$ to the predicted value from the model. The MSE measures the average of the squares of the errors – that is, the average squared difference between the estimated values and the actual value. R^2 compares the sum of squared residuals obtained from the model (SS_{res}) to the sum of squared residuals obtained from a horizontal line fit (SS_{tot}), which represents the null hypothesis. In the best case, $R^2 = 1$, a baseline model has $R^2 = 0$ and if $R^2 < 0$ the model fits worse than the horizontal line or mean of the data [155].

8 Objectives

This chapter introduces the ten hypotheses investigated in this thesis. All hypotheses are given separately at the end of each of the sections representing the three different analyses approaches pursued. A short motivating overview of the most important literature and the pursued methodological approaches are given in this section. A detailed description of each of the three analyses are given in chapter 9.

8.1 fMRI BOLD analysis

The perception of pain is a subjective and multidimensional experience that has a profound impact on the physiological and psychological state of an individual [28, 197]. Chronic pain states are characterized by a hypersensitisation of nociceptive neurons [106], a reduced endogenous inhibition of the nociceptive system [82, 124, 274], and by maladaptive cortical processes [222, 231]. The cortical regions that are involved in the processing of chronic pain have primarily been investigated with experimentally-applied exogenous pain, i.e. thermal [31, 107, 262, 288], electrical [57, 78, 167], mechanical [101, 110, 113, 146], or chemical stimulation [252, 273]. These studies found increased activity in chronic pain patients in regions also involved in the encoding of acute pain, such as the primary and secondary somatosensory cortices (S1, S2), sections of the insular and cingulate cortices, the cerebellum, and the thalamus [15, 28, 88, 177, 231].

However, applying additional experimental pain to chronic patients already experiencing pain and investigating their response may reveal cortical processes that are not necessarily at the core of the chronic pain disease. First and foremost should be the unravelling of the underlying processing of the chronic pain experience, independent of external tasks or stimulations. What matters most to the individual are the dynamics of their endogenous pain experience, which fluctuates over time and consists of periods of increasing, stable, and decreasing pain intensity. Based on previous approaches [25, 185], investigations of pain intensity coding should therefore include all intensity levels and dynamics in the pain experience and not be restricted to periods of increasing pain. It is thus important to preserve the naturally evolving cortical trajectory of the patients' endogenous pain as much as possible with a continuous and event-free study design. This study thus complies with a more naturalistic paradigm to capture the individual endogenous pain experience for each subject as naturally as possible. Only by identifying the functional underpinnings of the connections of pain encoding, a treatment can target maladaptive developments and possibly redirect functional connections back to a healthy processing brain.

In four repeated fMRI sessions, 20 chronic back pain patients and 20 chronic migraineurs were asked to continuously rate the intensity of their endogenous pain. Cortical activity was therefore recorded simultaneously to the subjects' individual pain ratings during 25 minutes of one fMRI session without external stimulation. Linear mixed effects models were then used to

relate brain activity to the pain rating data to disentangle cortical processes related to pain intensity and to changes in pain intensity, i.e. increasing or decreasing pain. A detailed description of the experimental setup and applied methods are given in the following sections 9.2 – 9.3.

With respect to the following three hypotheses, a detailed analysis and discussion of the BOLD analysis is given in chapter 9.3:

(1) At group-level, the involvement of cortical regions that are known to contribute to the processing of pain, i.e. subregions of the insular and cingulate cortices, the primary and secondary somatosensory cortices, the thalamus, and the PAG is hypothesized for both pain cohorts.
(2) Different brain regions are hypothesized to show activation for the encoding of pain intensity and the encoding of the change in pain intensity.
(3) At subject-level, for each pain cohort, the processing of pain intensity and the change of pain intensity in chronic pain patients is hypothesized to yield a variety of individual patterns, i.e. the encoding of pain in chronic pain patients is subject-specific rather than generalisable across chronic pain disease.

8.2 fMRI functional connectivity analysis

Functional connectivity has become essential at exploring the functional network structure of both healthy and diseased brains [6, 237, 282, 319]. Alterations in functional connectivity patterns due to neurological or psychiatric disorders, as well as changes due to long-lasting chronic pain conditions have been reported [138, 183, 242]. Chronic pain conditions have been studied by analysing intrinsic cortical networks as well as computing seed-based correlations of one or a few predefined brain regions.

In a complex whole-brain connectivity study using cortical parcellation, multiple changes for chronic back pain (CBP) patients particularly for connections involving the frontal cortex and the ACC were found [24]. CBP patients were additionally found to exhibit a general reorganisation of the DMN, with increased connectivity of the DMN to the medial prefrontal cortex, ACC and left anterior insula and decreased connectivity of mPFC with the precuneus [30, 277]. A further study investigated CBP patients in high and low pain conditions. Compared to controls, patients had greater connectivity in the left fusiform, occipital, right posterior cingulate and inferior parietal cortices [147]. High back pain intensity was associated with stronger FC of the primary somatosensory (S1) and motor (M1) cortices and the left superior frontal cortex. In addition, CBP has been found to alter the connectivity between primary sensory networks compared to controls [267]. The authors reported e.g. increased connectivity between the primary visual network and S1 as well as decreased connectivity between the primary visual network and the left angular gyrus/lateral occipital cortex; the connectivity strength was further negatively correlated with the disease duration.

Specifically for CM patients compared to episodic migraineurs, a study revealed greater connectivity within an intrinsic network consisting of the ACC, the anterior insula, the thalamus, the dorsolateral prefrontal cortex, the precuneus, the supramarginal gyrus, and the cerebellum. In addition, the authors found a greater connectivity between this network and the hypothala-

mus as well as the dorsal raphe nuclei [159]. A further study reported decreased connectivity between the executive control network and the left dorsal attention system in CM compared to healthy controls [70]. Additionally for chronic migraineurs, a disrupted functional connectivity between the DMN and the executive control network, but increased functional connectivity between the DMN and the left dorsal attention system has been reported [70]. Furthermore CM patients showed stronger connectivity of the amygdalae with regions in the inferior temporal, prefrontal, cingulate, as well as the pre- and postcentral cortices compared to EM. In contrast, weaker connectivity was found between the right amygdala and occipital regions in CM compared to healthy subjects [65]. Similar results were obtained by [260], who were identifying atypical resting-state functional connectivity e.g. of the anterior insula, amygdala, thalamus and the PAG in CM compared to controls. In addition, the disease duration correlated with the strength of connectivity between the anterior insula and thalamic nuclei as well as the PAG. In this study, CM patients showed positive correlations between the left anterior insula and negative correlation between right amygdala and left occipital. CM patients were also found to show decreased connectivity within a central executive network between the right ventrolateral prefrontal cortex (PFC) and the thalamus as well as between the left dorsal PFC and the dorsomedial PFC compared to controls [9].

There are a number of challenges that hamper the formation of a unified framework for the understanding of the cortical underpinnings of chronic pain disease and might be the reason for the often contradicting findings across the FC-literature. First, findings from resting-state studies do not necessarily represent pain-specific networks that are at the very core of the disease. As a major disadvantage, analyses on stationary cortical maps can not take the ongoing functional dynamics of the subjective experience of pain into account. In addition, the cause of the common fluctuation of BOLD activity, which gives rise to distinct intrinsic networks, is not entirely understood yet. The BOLD fluctuations, consisting of peaks and troughs, might be caused by the continuously changing pain intensity, but this has not been sufficiently tested so far and network fluctuations that are unrelated to the ongoing experience of pain would be difficult to interpret. Second, most of the studies in the neuroimaging literature lack reliable cortical data with repeated measurements for reproducible and longitudinal observations [183, 221], which may explain the heterogeneity e.g. of the DMN findings. Therefore, extended and repeated recordings are mandatory in order to disentangle a subject's stable signature from random momentary fluctuations of brain activity that are valid only for a single measurement.

In a whole-brain connectivity analysis of 408 brain areas, FC between pairs of brain regions with respect to the acquired pain ratings were investigated in this thesis. With a sliding-window approach, the time-varying connectivity between all brain regions was determined across the entire recording period and linear mixed effects models were fitted to explore the relationship between cortical activity and the observed trajectory of the patients' fluctuating endogenous pain.

With respect to the now following four hypotheses, a detailed analysis and discussion of the whole-brain functional connectivity approach to identify coherent brain connectivity patterns of chronic pain encoding is given in chapter 9.4:

(4) Functional connectivity patterns describing the neuronal response to pain, are hypothesized to show increased connectivity for higher pain perception and lower functional connectivity for

lower perceived pain.
(5) Qualitative different patterns for the encoding of pain intensity and the encoding of change in pain intensity for both chronic pain cohorts are hypothesized.
(6) On group-level, mostly functional connections involved in pain processing, i.e. functional connections between insular/frontal opercular, ACC, PCC and frontal regions are hypothesized.
(7) On single subject-level, specific individual alterations in the cortical pattern between subjects due to their long lasting pain are hypothesized, arguing against one biomarker for chronic back pain or chronic migraine.

8.3 Supervised machine learning analysis

In recent years, data-driven methods such as machine or deep learning techniques have gained increased attention and have become progressively popular to harvest novel, undetected information of the brain's dynamics. Classifying disorders or predicting pathological development based on a subject's spatial brain structure or activity obtained with MRI is an intriguing possibility to develop biomarkers for specific diseases. Most studies so far have focused on diagnosis to identify brain signatures that discriminate healthy control subjects from patients involving several diseases and disorders, i.e., Alzheimer's disease, mental health and pain disorders [80, 181, 245, 308]. fMRI neuroimaging datasets contain a wealth of information, however, extracting useful information from raw scan data still remains challenging and the results often only represent a collection of independent effects. While common univariate analysis of fMRI data is informative in revealing various correlates of the BOLD signal, it is insufficient for investigating the interactions of systems responsible for the localized activations found from the univariate analysis approach. Therefore, ML algorithms, which try to identify brain patterns in the data to make predictions for unobserved data, flip the typical direction of fMRI analysis [238]: In order to allow for an accurate prediction to data with unknown label, task events are treated as dependent variables and observed fMRI data as independent variables to find the best model parameters describing the underlying processes. All available brain activity information is integrated and multiple interacting, dependent brain networks are included [235]. In this way, complex intrinsic variations of spatial and temporal dependencies within fMRI data can be detected, which seems particularly well suited for the investigation of the diverse networks of brain areas involved in the encoding and processing of the pain experience.

Since the first application of ML algorithms to the field of pain research in 2010 [181], several different investigations have been made to assess structural [27, 287] as well as functional changes. Chronic low back pain patients for example were distinguished from healthy individuals on structural changes in Ung et al. [287]. The most common ones use classification methods based on support vector algorithms with an experimental design of external thermal stimuli to assess pain thresholds and pain sensitivity [245, 254]. Several studies showed the ML algorithms were able to discriminate painful from non painful externally applied stimuli [45, 47, 295]. In a previous study [295], the Neurologic Pain Signature (NPS) was developed, a model to predict pain ratings in participants of four levels of thermal stimuli. The evolution of magnitude perception were investigated by Cecchi et al. [59] on subject-level and in Brown et al. [47] a certain stability of BOLD activations was encountered across individuals, both spatially and magnitude wise. This indicates that at least for applied exogenous noxious stim-

uli, patterns of BOLD activity are consistent enough to potentially develop a physiology-based classifier for pain, which most importantly for clinical applicability, generalizes well to other subjects. Additionally, they found that improved predictions were obtained, when pain was assessed on the whole-brain activity pattern in contrast to only a few individual brain regions.

So far, however, only self-report and questionnaire-based tools are the standard evaluation method for the pain experience and classify the foremost subjective experience, which can fail certain vulnerable populations, such as e.g., patients with dementia [47]. Especially in chronic pain, an objective measure for diagnosing and evaluating the fluctuating persistent pain experience is missing [235]. The approach chosen in the present work therefore investigates the possibility of a BOLD signal based marker for different pain intensity levels which then can predict the pain intensity of unknown brain states. Brain based objective measures of pain may augment and facilitate diagnosis, treatment, and promote better understanding of the underlying cause of different types of brain [57, 282].

Based on the BOLD activations during the four repeated measurements of the pain rating experiment, a supervised ML approach was investigated to test the possibility of predicting the pain intensity levels based on cortical activations. Two regression models were compared in their performance. A group-level and subject-level approach was investigated separately, i.e. learning on all data of one chronic pain cohort vs learning the model on subject specific data. To investigate the stability of the fMRI sessions acquired relationship between cortical activity and pain rating, a between-session and within-session approach were pursued.

With respect to the now following three hypotheses, a detailed analysis and discussion of the machine learning approach is given in chapter 9.5:

(8) Supervised ML approaches are hypothesized to predict pain intensity for chronic pain patients based on fMRI BOLD activity patterns.
(9) Comparing subject-level with group-level, learning on single subject-level data is hypothesized to yield better performance compared to learning on group-level data.
(10) The relationship between brain activity and pain intensity level is hypothesized to be constant over time, i.e. if the relationship is learned in one fMRI session it can be used to predict brain activity in a different session.

9 Whole-brain fMRI analysis in chronic back pain and chronic migraine patients

This chapter presents the methods and results for all three analysis approaches, i.e., BOLD analysis, connectivity analysis, and a machine learning approach. A detailed description of the study and experimental procedure common to all three analysis approaches is presented in sections 9.1 and 9.2. BOLD-specific analysis methods and results are presented and discussed in section 9.3, connectivity-specific analysis methods with results are presented and discussed in section 9.4 and ML-specific analysis methods and results are presented and discussed in section 9.5.

The work presented in chapters 9.3 and 9.4 have been drafted into two manuscripts that were submitted to scientific journals. By the time of submission of this thesis, the papers have not yet been peer-reviewed. However, preprint versions of the manuscripts have already been published on bioRxiv, a free online archive and distribution service for complete but unpublished manuscripts (preprints) in the life and health sciences, operated by Cold Spring Harbor Laboratory, as a not-for-profit research and educational institution. In this chapter, several paragraphs are taken verbatim or slightly modified from these preprint manuscripts for which the citation for the preprint for the BOLD analysis (chapter 9.3) will be referred to by reference [187] and for the preprint of the connectivity analysis (chapter 9.4) by reference [188].

9.1 Patients and questionnaire

In total 40 patients were included in the analysis: 20 patients diagnosed with chronic back pain (CBP - 16 female; aged 44 $\pm$ 13 years) and 20 patients with chronic migraine (CM - 18 female; aged 34 $\pm$ 13 years). CBP patients were diagnosed according to the IASP criteria (The International Association for the Study of Pain; [194]) and CM patients were diagnosed according to the ICHD-3 (Headache Classification Committee of the International Headache Society (IHS) 2018). All patients were permitted to continue their pharmacological treatment at a stable dose (see Appendix chapter 11 for patient characteristics Tables 11.7–11.9). The patients did not report any other neurological or psychiatric disorders, or had contraindications for an MRI examination; patients with any additional pain were excluded from the study. For all patients, a fluctuating pain (in contrast to a constant pain at the same intensity level) was a prerequisite for inclusion. All participants gave written informed consent. The study was approved by the Ethics Committee of the Medical Department of the Ludwig-Maximilians-Universität München and conducted in conformity with the Declaration of Helsinki.
Patients were characterized using the German Pain Questionnaire (Deutscher Schmerzfragebogen; [58]) and the German version of the Pain Catastrophizing Scale (PCS; [276]). The pain intensity describes the average pain in the last four weeks from zero to ten with zero representing no pain and ten indicating maximum imaginable pain (see small excerpt in Table 9.1). The German version of the Depression, Anxiety and Stress Scale (DASS) was used to

rate depressive, anxiety, and stress symptoms (Appendix Tables 11.7 – 11.9) over the past week [170].
In total nine initially screened patients were excluded: two patients developed additional pain during the study, the pain ratings of five patients were constantly increasing or decreasing throughout the pain rating experiment, and two patients were unable to comply with study requests. In total, 36 patients were recorded four times across six weeks with a gap G of at least two days (median (IQR): $G_{CBP} = 5\,(5.5)$ days, $G_{CM} = 7\,(8)$ days) between sessions. Four patients (two CBP and two CM) only completed 3 of 4 sessions.

	CBP	CM
pain intensity [0-10]	5 ± 2	5 ± 1
pain duration in years	10 ± 7	15 ± 12
PCS [0-52]	17 ± 10	21 ± 10
depression [0-21]	4 ± 3	3 ± 3
anxiety [0-21]	3 ± 2	3 ± 4
stress [0-21]	7 ± 4	6 ± 4

Table 9.1: Example of six characteristics (mean ± standard deviation) evaluated in the questionnaires; scores given in brackets indicate the possible range of values of the variable. See Appendix Tables 11.7 – 11.9 for detailed patient characteristics and questionnaire data.

9.2 Experimental setup and data acquisition

Altogether, four fMRI sessions of 25 minutes duration with simultaneous subjective pain rating recordings were acquired from two chronic pain cohorts, CBP and CM. During the fourth session, following the pain rating task, one additional measurement of 25 minutes of a visual control condition (see section 9.2.2) was recorded for all patients.

9.2.1 fMRI acquisition parameters

fMRI data were recorded on a clinical 3T MRI scanner (Magnetom Skyra, Siemens Healthineers, Erlangen, Germany) using a 64-channel head coil. A T2*-weighted BOLD gradient echo sequence with echo-planar image acquisition and a multiband factor of 2 was used with the following parameters: number of slices = 46; repetition time/echo time = 1550/30 ms; flip angle = 71°; slice thickness = 3 mm; voxel size = 3×3×3 mm^3; field of view = 210×210 mm^2. 1000 volumes were recorded in 1550 s resulting in a temporal resolution of 1.55 s per volume. Field maps were acquired in each session to control for B_0-effects.
For each patient, T1- and T2-weighted anatomical MRI images were acquired using the following parameters for the T1 MPRAGE sequence: repetition time/echo time = 2060/2.17 ms; inversion time = 1040 s; flip angle = 12°; number of slices = 256; slice thickness = 0.75 mm; voxel size = 0.75×0.75×0.75 mm^3; field of view = 240×240 mm^2, and for the 3D TSE T2 SPACE sequence: repetition time/echo time = 3200/560 ms; flip angle = 120°; number of slices = 256; slice thickness = 0.75 mm; voxel size = 0.75×0.75×0.75 mm^3; field of view = 240×240 mm^2.

9.2.2 Pain rating recording

During the fMRI acquisitions, patients rated the intensity of their ongoing pain for 25 minutes using an MRI-compatible potentiometer slider [256] (Figure 9.1 a). The scale ranged from 0 to 100 in steps of five with 0 representing no pain and 100 representing the highest experienced pain. On a light grey screen a moving red cursor on a dark grey bar (visual analogue scale, VAS) and a number above (numeric analogue scale, NAS) were shown during the entire functional MRI session (Figure 9.1 b). The screen was visible through a mirror mounted on top of the MRI head coil. Patients were asked to look only at the screen, focus on the pain with an emphasis on the fluctuating nature of their pain experience. The intensity and the changes of perceived pain had to be indicated as quickly and accurately as possible. To minimize head movement, foam pads were placed around the head and patients were instructed to lie as still as possible throughout the entire scanning session.

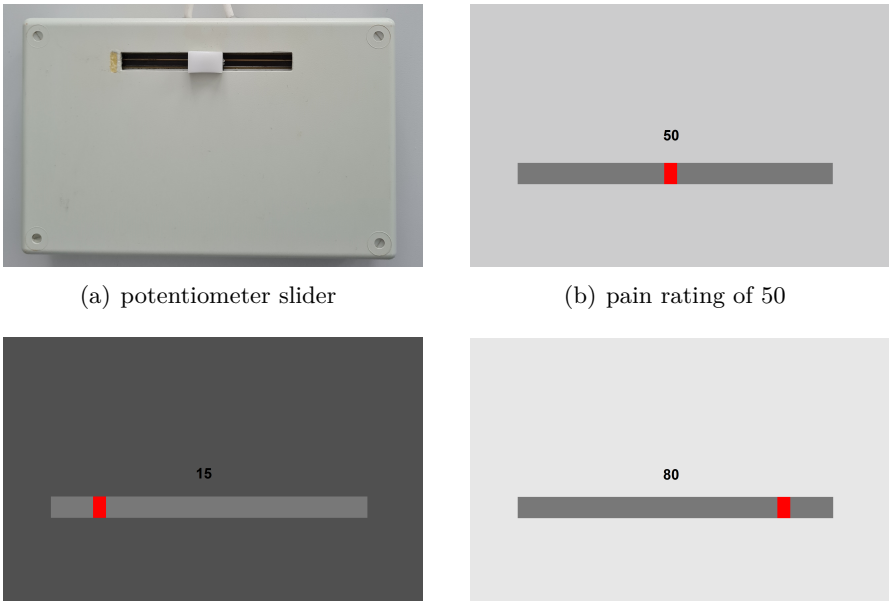

(a) potentiometer slider (b) pain rating of 50

(c) visual rating of 15 (d) visual rating of 80

Figure 9.1: Experimental setup: The patients indicated their pain experience with the MRI-compatible potentiometer slider (a) during the fMRI acquisitions and saw the according curser movement on the visual and numeric analogue scale on the screen (b). For the visual control condition, the changing background brightness (two different brightnesses (c) and (d)) was to be rated.

To control for visual-motor performance and decision-making activity during the pain rating session, a visual control experiment was carried out during the last visit. Patients were asked to continuously rate the changing background brightness of the screen as accurately and quickly as possible. The same feedback in the form of a red bar (VAS) and a number (NAS) was given on the same screen as for the pain-rating experiment (Figure 9.1 c and d). Unbeknownst to the patient, the control condition was a composition of parts of the previous pain rating sessions to match with range and frequency of the pain rating. Pain ratings between 0 and 100 in steps of 5 were converted to 21 shades of grey, 0 indicating black ([RGB: 0 0 0]) and 100 indicating white ([RGB: 255 255 255]).

9.2.3 Pain rating data preprocessing

The pain rating time courses for all individual patients in each session are shown in the Appendix in Figures 11.2 and 11.3 for CBP and CM patients, respectively. The average pain ratings were variable between recording sessions. For CBP and CM, an average rating of 39 ± 14 and 40 ± 15 was found, respectively. The pain ratings within each of the 78 sessions were fluctuating substantially, as reflected by a high variance over the 25 minutes of each recording: $\sigma^2 = 109.3 \pm 126.6$ for CBP and $\sigma^2 = 93.3 \pm 62.8$ for CM, given as the mean and standard deviation of the mean individual variances over all 78 sessions for each patient cohort, separately. The average rating did not exhibit any systematic change over the time course of one experimental session. A linear fit to the rating revealed a minor positive slope of 0.13 ± 0.41 1/min (mean change of rating unit per minute) for CBP and of -0.05 ± 0.37 1/min for CM (all mean $\pm$ standard deviation) was found.

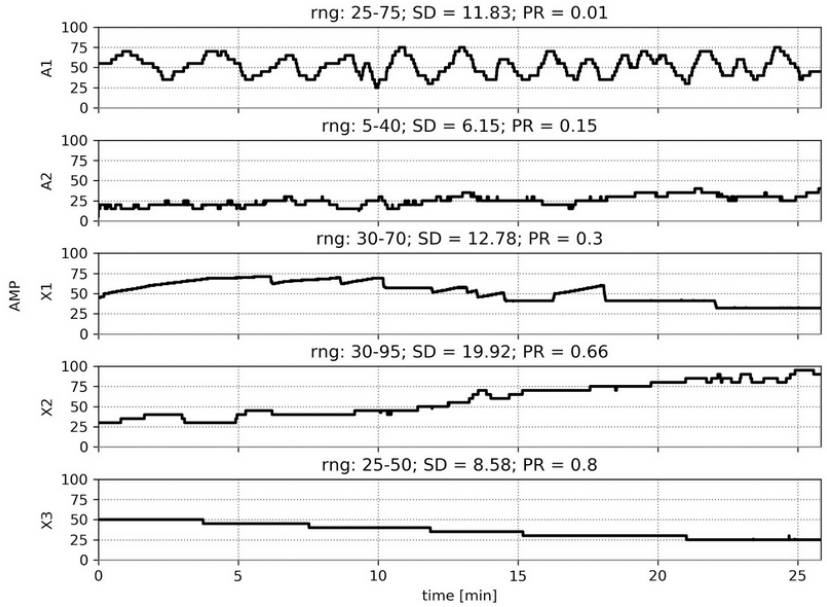

Figure 9.2: Accepted and rejected pain ratings based on the PR parameter with individual range (rng: min-max), standard deviation (SD) and parameter PR for each rating: Rating A1 represents an excellent rating with a very low PR value of 0.01, indicating high variance and no overall drift throughout the experiment. Rating A2 represents a pain rating with a moderate PR value of 0.15, whereas X1 represents an excluded rating with a PR slightly higher than the set threshold PR ≥ 0.25. X2 was excluded due to a steady increase in the pain ratings over the course of the experiment. X3 was excluded due to very low variability in ratings after high-pass filtering. Ratings A1 and A2 were accepted, whereas recordings X1, X2 and X3 were excluded from the analysis. Figure and legend taken from [187].

The rating time courses were required to fluctuate at a relatively constant level, in order to mitigate potential effects of order (e.g. in case of continuously rising pain). To ensure that the behavioural task performance of the patients fulfilled this criterion, the ratings of each patient's pain was quickly evaluated based on a constructed parameter PR after each fMRI recording session (see Figure 9.2 for examples of accepted and rejected pain rating time courses). The

ratings of each patient's pain were measured with the parameter PR defined as

$$PR = \frac{\Delta p_{ud}/\Delta t}{\sigma_{fd}} \tag{9.1}$$

with the numerator $\Delta p_{ud}/\Delta t$ being the slope of the regression line of the unfiltered data (ud) and σ_{fd} being the sample standard deviation of the filtered data (fd). The parameter PR is constructed in a way that its minimisation is desirable. The numerator describes how much the prerequisite is violated by fitting a least squares line across the rating time course. This violation can be compensated if the variance of pain ratings is considerably higher than the slope of the regression of the least squares line across the entire time course of the pain ratings. The standard deviation of the filtered data expressed in the denominator gives a measure of the (desired) fluctuations of the pain ratings but is stripped from a potential trend throughout the experiment. A minimisation of the quotient is given either by minimising the numerator corresponding to a small increase of the overall pain ratings over the whole experiment (small slope), or by maximising the denominator corresponding to a large variability in pain ratings across the rating task. Minor overall rising in pain intensity over the whole time of the experiment could be compensated by a greater variance of ratings; small fluctuation of pain intensity would only be accepted in cases of minor pain rating trends across the entire experiment.
Recordings showing values of PR ≥ 0.25 were rejected from the analysis or repeated if possible. Five participants were excluded and three sessions were repeated. Figure 9.2 shows examples of accepted and rejected ratings based on the PR value. The threshold of the PR value was chosen based on the following considerations: First, cortical processes that would progress linearly over the time course of the fMRI acquisition, would be filtered out through temporal data filtering as part of the preprocessing. Second, to avoid effects of order of e.g. steadily increasing pain intensity in CBP patients due to laying in the scanner for an extended period of time, linearly increasing or decreasing pain ratings were limited through the chosen threshold of the PR value. Finally, careful inspection of the pain rating data after each recording, determination of the the number of slider movements and overall trend of the rating throughout the 25 minutes of each session motivated the PR threshold.

Two additional variables were introduced to separate the distinct activity and patterns of pain intensity encoding from brain processes related to the sensing of rising and falling pain, as well as from motor activity and decision making. An exemplary illustration of all three variables is shown in Figure 9.3. First, to disentangle the distinct aspects of pain intensity (AMP - amplitude) from cortical processes related to the sensing of rising and falling pain, the ongoing rate of change (SLP - slope, encoded as 1, -1, and 0) in the pain ratings was calculated as the slope of the least squares regression line across a 3 s time window of the 10 Hz pain rating data. Increasing pain is represented by a positive slope; decreasing pain by a negative slope. Periods with SLP = 0 indicate time frames of constant pain. Second, a vector of the absolute slope value of pain ratings (aSLP - absolute slope, encoded as 0 and 1) corresponds to the modulus of the SLP variable and represents periods of motor activity (slider movement), changes of visual input (each slider movement changes the screen), and decision-making (each slider movement prerequisites a decision to move). This variable does not account for the direction of the movement or the direction of the pain intensity change. Periods with aSLP = 0 indicate time frames of constant pain without the need to move the slider.

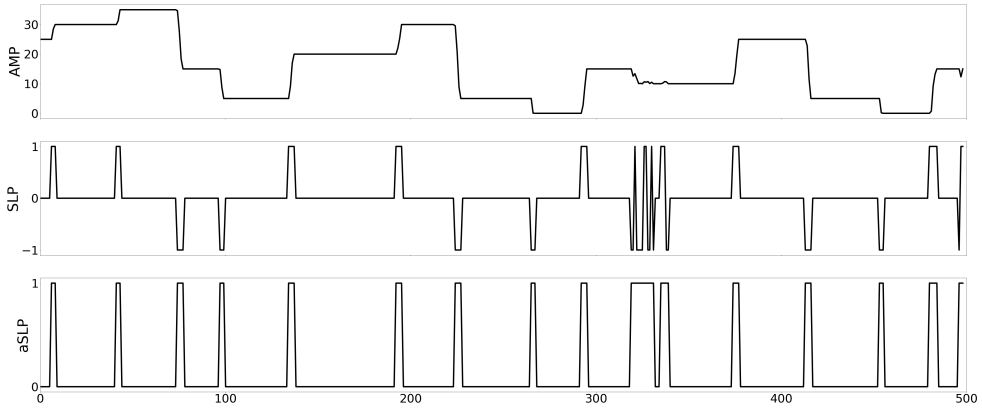

Figure 9.3: Exemplary pain rating variables AMP, SLP, aSLP over 500 datapoints corresponding to approximately half of one fMRI session. Pain intensity (AMP) rating range from 0 to 100, the SLP variable distinguishes rising (1), constant (0) and falling (-1) pain periods and aSLP encodes the motor activity of the slider movement (1) versus periods of rest (0).

These processes (SLP, aSLP) occur concomitant to the encoding of pain intensity (AMP) but are functionally, temporally and statistically independent, indicated by the low correlations of the three entities (AMP, SLP, aSLP): The mean ($\pm$ standard deviation) correlation coefficients (Fisher-z transformed) for all CBP/CM subjects for each of the variable pairs were: r(AMP, SLP) = 0.007 ± 0.04 / 0.02 ± 0.04; r(SLP, aSLP) = 0.06 ± 0.2 / 0.01 ± 0.12; r(AMP, aSLP) = 0.002 ± 0.08 / -0.004 ± 0.09.

9.2.4 Preprocessing

fMRI data were standard preprocessed using the Functional Magnetic Resonance Imaging of the Brain (FMRIB) Expert Analysis Tool (FEAT) in FSL (Version 5.0.10; [134]). The preprocessing for each subject included in the following order: slice time correction for interleaved acquisition, motion correction using MCFLIRT (motion correction using FMRIB's Linear Image Registration Tool) and B_0 unwarping, non-brain removal (using BET brain extraction), spatial smoothing using a Gaussian kernel with a FWHM (full width at half maximum) of 6 mm, a nonlinear high-pass temporal filtering with a cutoff of 400 s (lowest frequency 1/400 Hz) and spatial registration to the Standard Montreal Neurological Institute (MNI) template (FSL's MNI 152, T1: $2 \times 2 \times 2$ mm).
The rating data were continuously recorded and offline downsampled to 10 Hz. To remove the same filtering effects from the behavioural data as from the imaging data, a 400 s high-pass filter was applied.

Independent component analysis (ICA) was run with MELODIC ((Multivariate Exploratory Linear Optimized Decomposition into Independent Components) Module, Version 5.0.10, part of FSL) to minimize confounding factors i.e. respiration and cardiac cycles. Preprocessed data were projected into a 100-dimensional subspace and components were semi-automatically labelled by FIX (FMRIB's ICA-based Xnoiseifier, Version 1.06). Here, the BOLD signals are

separated into statistically independent components, representing either components of interest (BOLD signal) or noise-related (e.g. breathing) components. According to the components' spatial or temporal profile, artifact-related components were removed from the data following the recommendations in the literature [112], [140], [243]. The average number of artifact components for CM was 40 ± 6 and for CBP 49 ± 8.

The pain rating time courses (AMP, SLP and aSLP variables) of each patient were convolved with a hemodynamic response function (HRF) implemented in SPM12 [219] with the following parameters: $\mathrm{HRF} = \mathrm{spm}_{\mathrm{hrf}}(0.1, [6, 16, 1, 1, 100, 0, 32])$. The post-stimulus undershoot was minimized by the ratio of response to undershoot and motivated by the continuous and event-free fMRI study design. For the statistical analysis, the resulting filtered time course was transferred to Matlab (Mathworks, USA; version R2018a) and downsampled to the sampling frequency of the imaging data (1/1.55 Hz).

9.3 BOLD fMRI analysis in chronic back pain and chronic migraine patients

9.3.1 Sliding-window and statistical analysis for BOLD

A sliding-window approach was applied to investigate the timing of the different cortical processes. To allow for some variability in the HRF, responses between pathological populations (two different conditions), as well as between different tasks (encoding of pain intensity changes and encoding of motor activity), systematic shifting of the rating vector and BOLD response between -15 s and 20 s in steps of 1 s (36 steps) was applied. These shifts account for the unknown timing of cortical processing in reference to the rating: some ongoing cortical processes may influence later changes in pain ratings, other processes are directly related to the rating behaviour, or are influenced by the rating process and are occurring afterwards. The shifts were permitted to vary for different brain areas.

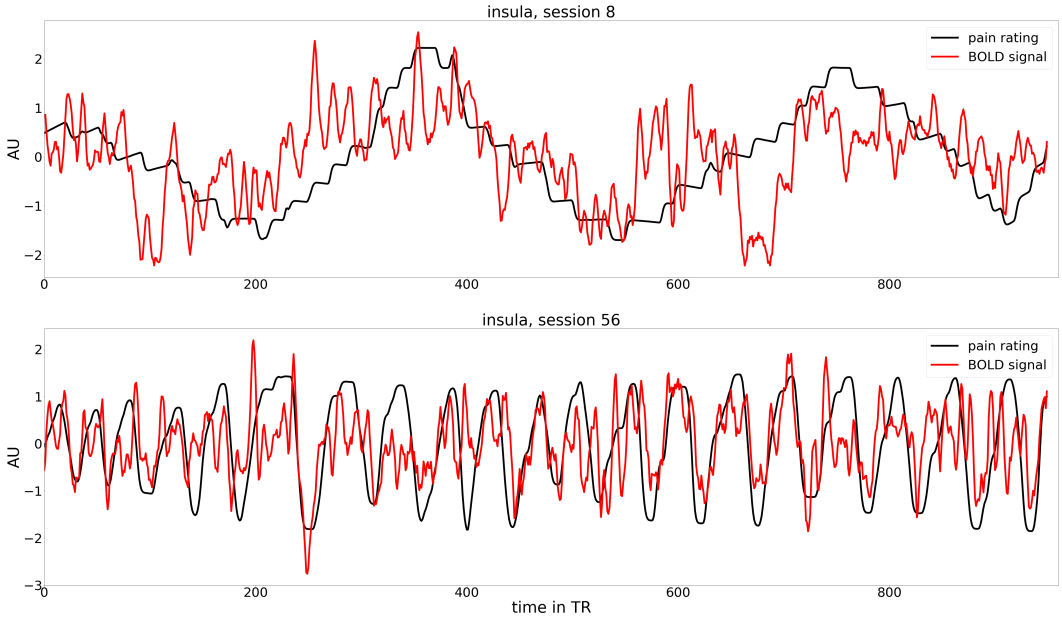

Figure 9.4: Exemplary pain ratings and BOLD signal in one voxel in the insula for two subjects in different sessions.

Voxel-wise linear mixed effects models (LME; MixedModels.jl package in Julia [38]) were computed to identify the brain regions in which the cortical activity changed during the experiment with respect to the amplitude of the pain rating (amplitude - AMP), as well as to rising or falling pain (slope - SLP). Illustrative exemplary obtained BOLD signals in one voxel in comparison to the pain rating are visualised in Figure 9.4. Each change of pain rating, irrespective of direction, is accompanied by motor activity, decision-making processes, and the perception of visual change on the monitor (absolute slope - aSLP). Respective time courses of AMP, SLP and aSLP were related to the time courses of brain activity in order to obtain a statistical estimate of the cortical underpinnings of these independent processes. The fluctuating BOLD activity of a particular brain voxel is modelled through the time course of the three variables

with the following model, expressed in Wilkinson notation [303]:

$$\begin{aligned} intensity \sim 1 + AMP + SLP + aSLP + \\ + (AMP - 1|session) + (SLP - 1|session) + (aSLP - 1|session) \end{aligned} \tag{9.2}$$

The included four fixed effects (represented by the four terms in the first line of equation 9.2) describe the following four properties: the magnitudes of the population common intercept ('1') and the population common slopes for the relationship between cortical data and the intercept and these three variables ('AMP, SLP, aSLP'). The $3 \cdot 78 = 234$ random effects (represented by the three terms in the second line of equation 9.2) model specific intercept differences for each recording session, which accounts for session specific differences in pain levels, for the three variables AMP, SLP and aSLP for each of the 78 (18 subjects $\times$ 4 sessions + 2 subjects $\times$ 3 sessions) recorded sessions. T-values of the fixed-effects parameters quantify the relationships which is of main interest in the analysis, i.e. identifying significant relationships of BOLD signal intensity for different pain levels (AMP), distinguishing rising and falling pain (SLP), and motor activity from rest (aSLP). Whereas AMP is represented by the continuous levels of pain intensity, the values for SLP (-1, 0 1) and aSLP are binned but numerical. This means that the interpretation of the statistics for SLP resembles a paired t-test between the conditions positive slope ('1') and negative slope ('-1'). The model was calculated 36 times for each of the shifts of the sliding-window approach, which results in 36 t-values for each variable (AMP, SLP, aSLP) and voxel of which the highest t-values were extracted. The model was separately calculated for CM and CBP.

For the direct contrast with the visual control experiment, the following model was computed with conditions pain vs. visual:

$$\begin{aligned} intensity \sim 1 + AMP \cdot condition + SLP \cdot condition + aSLP \cdot condition + \\ + (0 + AMP|session) + (0 + SLP|session) + (0 + aSLP|session) \end{aligned} \tag{9.3}$$

All voxel-wise statistical tests were corrected for multiple comparisons and autocorrelation in the behavioural data in the following way: 500 surrogate time courses were created from the rating data (Iterative Amplitude Adjusted Fourier Transform (IAAFT) algorithm [251, 279]), which were uncorrelated to the original rating data but had the same autocorrelation structure as the original data. The LME analysis was repeated 500 times with the surrogate data, resulting in 500 whole-brain statistical maps for AMP, SLP and aSLP. The highest absolute t-values from each map and repetition across the whole volume was extracted, which resulted in a right-skewed distribution of 500 values for each condition [256]. Based on the obtained distribution, the statistical threshold was determined using the Permutation Analysis of Linear Models (PALM) tool from Winkler et al. [305], also implemented in FSL [304]. The obtained statistical thresholds for the group and single subject analysis are given in Table 9.2.

In addition, the resemblance of the topography of the amplitude encoding (AMP) to the topography of the neurological signature of applied physical pain (Neurologic Pain Signature, NPS; [295]) was tested. By thresholding the NPS weights map at 0.005 and the AMP map at $t > 2$ both maps were 'normalised' with the following procedure: the pre-selected absolute t-values were ranked and equidistant numbers between 1 and 1000 were given to each included voxel. Voxels with negative t-values were given back their negative sign. Spatial correlations using Kendall's τ coefficients were computed for the common superthreshold voxels (4900 voxels for

CBP			
subject	**AMP**	**SLP**	**aSLP**
1	7.40	8.66	5.04
2	7.61	6.52	4.24
3	7.34	6.88	4.21
4	6.51	5.59	5.32
5	7.53	7.02	5.48
6	7.03	8.05	4.61
7	6.03	6.64	5.35
8	9.16	4.96	4.31
9	6.53	6.52	7.74
10	7.15	7.92	4.53
11	6.83	6.97	4.79
12	9.15	5.46	5.89
13	6.53	5.50	5.00
14	6.04	5.72	4.54
15	6.41	5.06	4.46
16	11.82	5.89	4.49
17	5.74	5.81	5.19
18	6.73	5.72	6.42
19	4.96	4.96	5.19
20	5.73	5.74	4.00
group	2.98	4.33	3.91

CM			
subject	**AMP**	**SLP**	**aSLP**
1	10.23	4.92	4.34
2	7.85	5.34	5.14
3	8.30	7.09	5.62
4	5.94	6.32	5.44
5	6.05	6.66	4.78
6	7.50	5.68	4.65
7	7.64	5.47	4.68
8	6.16	5.98	4.37
9	7.47	4.96	5.02
10	8.06	4.80	4.81
11	7.80	7.41	6.18
12	5.79	5.99	5.38
13	6.82	5.86	6.24
14	7.92	6.06	5.96
15	7.18	5.54	5.21
16	8.81	6.76	4.21
17	6.66	6.27	4.69
18	7.31	7.78	5.88
19	6.43	5.09	6.01
20	7.45	5.61	6.28
group	2.85	4.92	3.88

Table 9.2: Statistical thresholds for BOLD analysis: t-values for CBP and CM patients as determined by PALM [305] for single subject and group analysis.

CM; 1966 voxels for CBP) of the NPS map and the group activity map.

The individual maps of endogenous pain encoding were also investigated separately for each participant across all recordings. To assess whether the pattern of activity resembles the map of the group statistics, the activity of the group maps were correlated with the activity of the single-patient maps. The data were restricted to the voxels of group statistics and subject statistics with an absolute t-value $t > 2$. Group- and single-subject maps were 'normalised' as given above. Separately for each patient, spatial correlations using Kendall's τ coefficients were computed for each patient's activity map with the group activity map for the common superthreshold voxels.

9.3.2 BOLD: Chronic back pain (CBP)

BOLD: Encoding of pain intensity across all CBP patients (AMP)

The subjective intensity of endogenous pain is encoded in the anterior insular cortex (AIC), the frontal operculum, and the pons (see Table 11.1 in Appendix for exact MNI coordinates). Regions that exhibit decreased activity with higher pain intensities were the following: the posterior cingulate cortex (PCC), the precuneus, the pregenual anterior cingulate cortex (pACC), and the hippocampus (Figure 9.5 A). These findings persist when computing the statistical contrast (Equation 9.3) between the pain and the visual condition, i.e. there is a significant

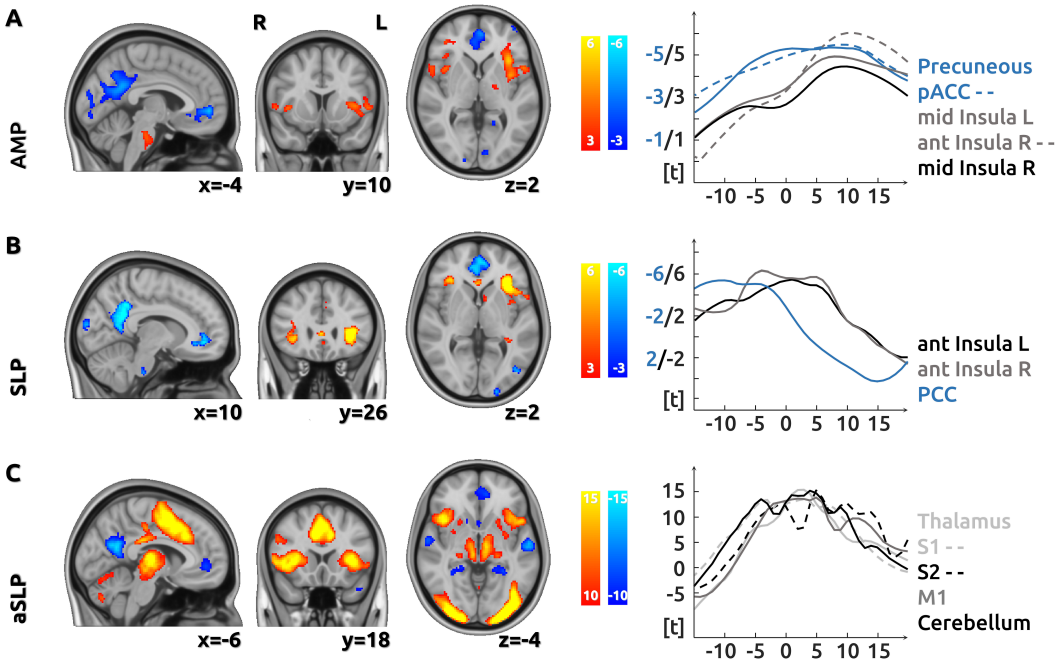

Figure 9.5: BOLD CBP: Visual representation of A pain intensity encoding (AMP), B change of pain intensity (SLP) and C motor activity encoding (aSLP) on the left; the right displays the time courses for a few individual regions across the sliding-window approach (36 time shifts on the x-axis), showing different peak times across regions and for the three variables AMP, SLP and aSLP; time courses in blue show a negative t-value. Figure and legend taken from [187].

difference in activations for the pain rating task compared to the control task. A spatial correlation between AMP and the NPS map [295] of 0.31 ($p < 0.001$) was found.

BOLD: Encoding of the change of pain intensity across all CBP patients (SLP)

The cortical processes that reflect the change of pain intensity are located in the AIC, in various regions in the frontal lobe (frontal orbital cortex, frontal operculum, middle frontal gyrus), as well as in the pACC, PCC and parahippocampal gyrus (Table 11.2 in Appendix). Brain regions that exhibit decreased activity during increasing pain comprise regions in the occipital lobe (occipital pole, lateral occipital cortex), the precuneus, the pACC and PCC, the paracingulate gyrus and the brainstem (Figure 9.5 B). The direct statistical comparison between the pain condition and the visual control condition (Equation 9.3) confirms the findings for the bilateral AIC and for the frontal lobe, i.e. the results persist in these regions, when the direct contrast between visual and pain condition is calculated (see section 9.3.4). The time courses given in Figure 9.5 B for the different regions exhibit a different temporal profile with a maximum peak before the regions in Figure 9.5 A for encoding the pain intensity.

BOLD: Processing of motor activity and decision making across all CBP patients (aSLP)

For the processing of motor activity, decision-making, and changes of visual input, an increased activity in the parietal lobe (superior parietal lobe, supramarginal gyrus), but also in the pre-

and postcentral gyrus (M1/S1), the middle frontal gyrus, the cerebellum, the thalamus, and the PCC was found (see Table 11.3 in Appendix). Decreased activity was located mainly in the hippocampus, the parahippocampal gyrus, the superior temporal gyrus, the lateral occipital gyrus, and the precuneus (Figure 9.5C). To separate the largely overlapping clusters and to disentangle the contribution of the brain regions, an increased threshold above the threshold of the randomisation statistics was used (see colourbar range in Figure 9.5 C).

BOLD: Individual activity maps for CBP

Activation maps for intensity encoding (AMP) for all single patients are shown in Figure 9.6. A considerable variety of activation patterns was found: while some patients exhibit a similar activity map as the maps from the group statistics, other patients show a rather weak correlation with the activity pattern of the group statistics, indicated by the correlation coefficient (Kendall's τ) given in the left top corner of each subject in Figure 9.6.

9.3.3 BOLD: Chronic migraine (CM)

BOLD: Encoding of pain intensity across all CM patients (AMP)

For CM, mainly the cerebellum is positively related to the intensity of endogenous pain, as well as the frontal orbital cortex and the temporal fusiform cortex (see Table 11.4 in Appendix). Areas negatively related to pain intensity were found in the PCC, the pACC and the subcallosal cortex, but also in the amygdala, and the thalamus (Figure 9.7 A). There was no difference for the direct comparison between the pain condition and the visual condition i.e. no specific effect was found for either the visual or the pain rating task. A spatial correlation between AMP and the NPS map of -0.08 ($p < 0.001$) was found.

BOLD: Encoding of the change of pain intensity across all CM patients (SLP)

The processes that contribute to the change of pain intensity only activate the cerebellum and the AIC (Table 11.5 in Appendix). Brain regions that exhibit decreased activity during increasing pain comprise various regions in the occipital lobe (occipital pole, lateral occipital cortex), as well as the angular gyrus, the precuneus, and the superior frontal gyrus (Figure 9.7 B). There was no difference for the direct comparison between the pain condition and the visual condition.

BOLD: Processing of motor activity and decision making across all CM patients (aSLP)

The processing of motor activity, decision making, and changes of visual input shows areas of increased activity mainly in the insular cortex, the thalamus, the pallidum, the parietal lobe (superior parietal lobule, parietal operculum, supramarginal gyrus) and the cerebellum (Table 11.6 in Appendix). Decreased activity was found in the precuneus, the hippocampus, the lateral occipital cortex, the superior frontal and superior temporal gyrus and the cerebellum (Figure 9.7 C). To separate the large overlapping clusters and to disentangle the contributions of the brain regions, the cluster threshold was increased above the threshold of the randomisation statistics (see colourbar range in Figure 9.7 C).

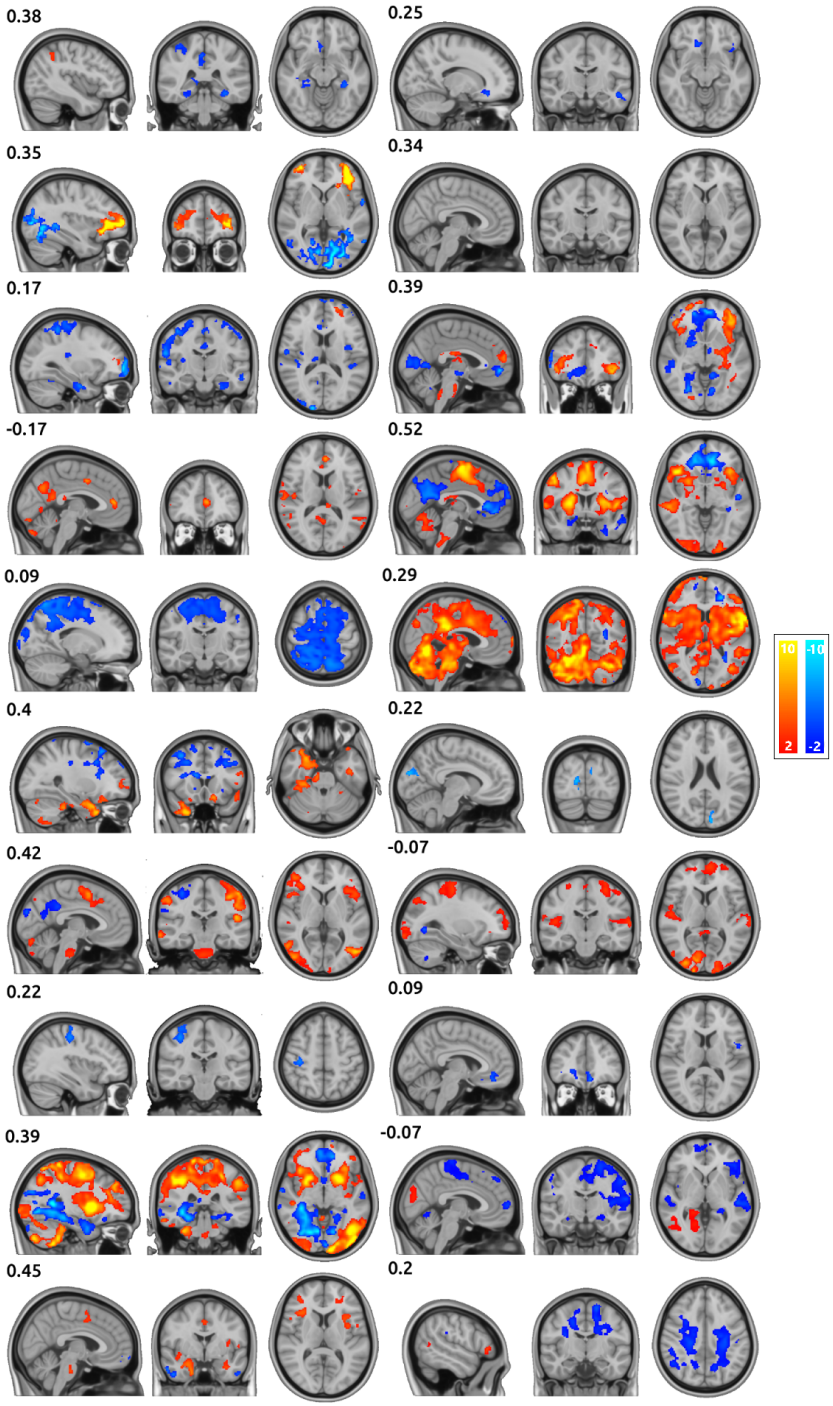

Figure 9.6: BOLD: CBP individual pain intensity (AMP) encoding with the numerical values at the top left of each subject denoting Kendall's τ coefficient of correlation with the group results. Figure and legend taken from [187].

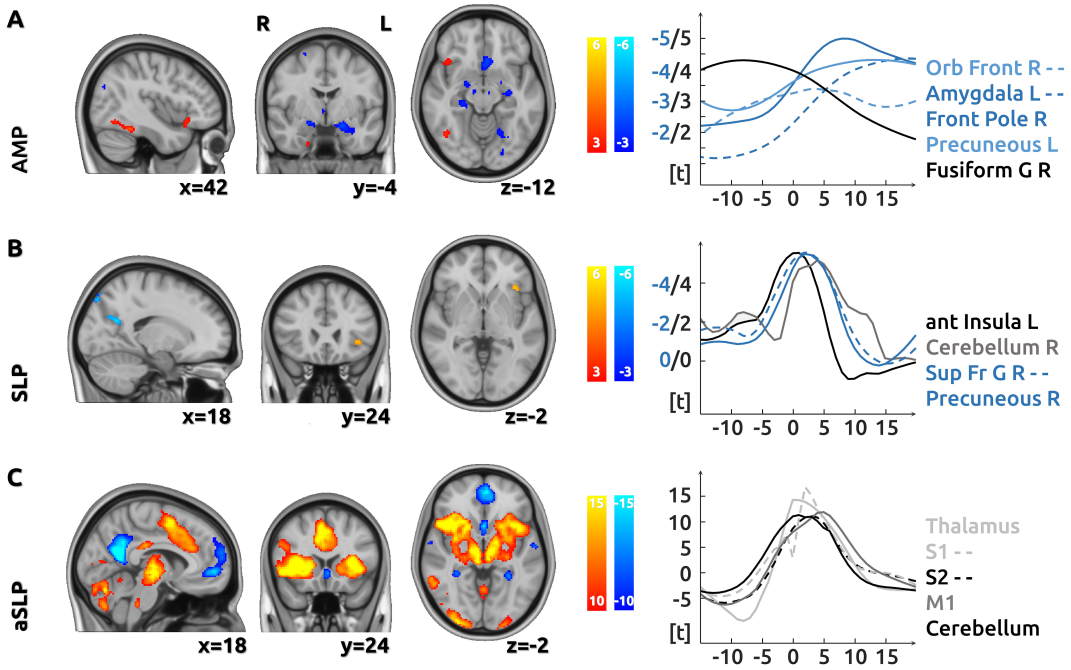

Figure 9.7: BOLD CM: Visual representation of A pain intensity encoding (AMP), B change of pain intensity (SLP) and C motor activity encoding (aSLP) on the left; the right displays the time courses for a few individual regions across the sliding-window approach (36 time shifts on the x-axis); time courses in blue show a negative t-value. Figure and legend taken from [187].

BOLD: Individual activity maps CM

Individual activity maps for the encoding of pain intensity are given in Figure 9.8 together with the individual correlation coefficient (Kendall's τ) indicating their similarity to the group results.

9.3.4 Visual control experiment

In the control experiment, predominantly occipital areas (occipital pole, lateral occipital cortex and occipital fusiform gyrus) of the brain were activated for the CBP patient group only (Table 9.3).

9.3.5 Discussion of BOLD fMRI results in CBP and CM

This approach aimed to investigate how the intensity and the intensity change of endogenous pain is encoded in the brain of chronic pain patients. In repeated fMRI sessions, 20 CBP and 20 CM patients rated their endogenous pain experience. The experimental design resembles the everyday experience of chronic pain patients, which is characterized by naturally fluctuating pain and consists of phases of relatively low and phases of relatively high pain. Linear mixed effects models were used to disentangle the cortical processes related to the different phases of pain intensity. At group level, the intensity of pain in CBP patients was found to be encoded in the AIC, the frontal operculum, and the pons; the change of pain in CBP and CM

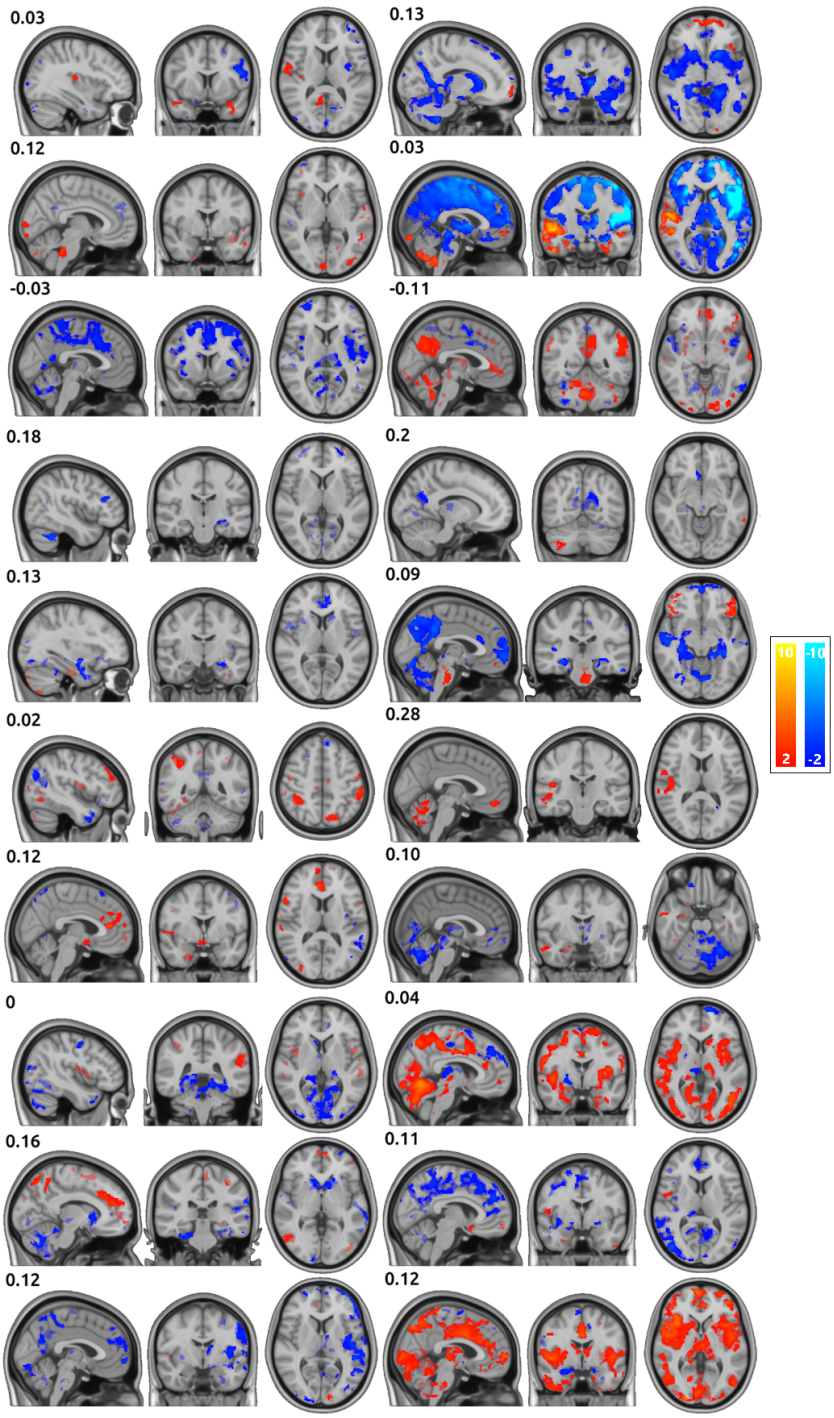

Figure 9.8: BOLD: CM individual pain intensity encoding with the numerical values at the top left of each subject denoting Kendall's τ coefficient of correlation with the group results. Figure and legend taken from [187].

anatomical structure	cluster size	t-value	x y z
AMP			
inferior frontal gyrus	225	16.2	35 32 6
frontal pole	216	-30	-33 52 24
paracingulate gyrus	141	-16.6	-2 53 -3
frontal pole	113	-16.2	-39 59 -3
frontal pole	99	-20.2	36 62 -8
anterior insular cortex	99	15	-31 16 7
inferior frontal gyrus	62	14.8	-33 31 4
paracingulate gyrus	56	-15	10 44 -4
SLP			
frontal operculum cortex, anterior insular cortex	484	15.8	-33 23 5
frontal orbital cortex	154	14.6	35 28 -1
precentral gyrus (M1)	41	12.4	-55 6 4

Table 9.3: Active brain areas for the direct contrast between the pain condition and the visual control condition for AMP and SLP in CBP; MNI coordinates are given for the center of the number of active voxels (cluster). Table and legend taken from [187].

patients was found to be mainly encoded in the AIC. At the individual level, a more complex picture was found where each patient exhibited their own signature of endogenous pain encoding. In the following, the present findings are mainly discussed in light of previous approaches to investigate endogenous and fluctuating chronic pain. To the best of knowledge, this is the first approach to investigate continuous pain intensity encoding in combination with a sliding window and LME analysis.

Methodological advances

By using a continuous, stimuli-free design, the entire time course of the data could be taken into account and the trajectory of cortical processes was related to the fluctuating intensity of pain. This more 'naturalistic' fMRI design is intended to exhibit greater real-world relevance, as task-based fMRI paradigms often do not resemble natural encountered stimuli and resting-state studies are difficult to control with patients trying not to think of anything. Both, stimuli-driven and resting-state paradigms can therefore not necessarily reveal the complex pattern of the chronic pain experience and identify the true underlying brain processes. Previous continuous endogenous pain recording studies were investigated mainly in the group of Baliki [28] and Apkarian [16], with the most similar one investigating continuous pain ratings over ten minutes in a longitudinal setting, comparing sub-acute back pain and CBP patients [120]. The approach in this thesis builds on the basics of a continuous rating fMRI design with several methodological improvements and further developments.

A particular focus was put on a fluctuating as well as balanced time course of pain ratings. This was classified by the PR parameter to ensure the capture of balanced epochs of multiple pain intensity levels as well as non-steady increasing or decreasing pain. In previous studies with similar designs [28, 185], subjects with continuously increasing pain throughout the experiment were included in the statistical analysis, which therefore e.g. do not take effects of order of the acquired time series into account. The PR parameter was a first attempt of a performance met-

ric of the continuous rating design, as there can be nothing comparable found in the literature. Additionally, as a particular focus was put on a fluctuating time course of pain ratings, brain regions that encode transient states of increasing and decreasing pain were detected. Previous pain rating studies investigated strictly binarised pain ratings to detect low or high pain states [28, 118]. These approaches lack the resolution of several different pain states between these two extremes in addition to a questionable definition of 'high' vs 'low' pain states for each individual. Compared to previous continuous pain rating designs [16, 29], the presented work here is therefore the first study to investigate the encoding of more than three different pain intensity levels with a continuous pain rating in combination with a sliding-window approach in CBP and CM patients.
Repeated, as well as extended sessions are necessary to obtain stable, robust and reliable results, especially for the relatively low signal-to-noise BOLD fMRI acquisition compared to e.g. structural MR images. The extended duration of the experiment guaranteed balanced phases of increasing, stable, and decreasing pain, which disentangled the processes related to pain intensity from aspects of pain intensity changes in all patients. The duration of typical fMRI resting-state designs is approximately five to ten minutes and include most of the time only one session for each subject [290]. Recommendations for a robust fMRI analysis include increasing the total acquisition time to improve reliability and similarity in the results obtained up to $\sim$ 16 minutes for resting-state acquisitions [41] and guidelines for more naturalistic paradigms include even larger acquisition times up to hours [3, 8]. To detect reproducible cortical activations, 4 sessions of 25 minutes were acquired for each subject. Thereby, 100 minutes of fMRI and pain rating data for 40 subjects provides an exceptional dataset suitable for reliable, individual analyses.
Investigations into reproducibility of fMRI results are scarce. In Amann et al. [6] repeated, longitudinal, task-based FC in two subjects were investigated with several statistical models but due to the low number of subjects, a generalisability is not given. Reproducibility of the BOLD activations in combination with the pain ratings of the four repetitions needs different statistical models than pursued in this approach and was not separately assessed. Therefore a different methodology was chosen and reproducibility was assessed with a ML approach (see section 9.5).

The pursued statistical approach differs from the current standard two-level GLM approach in common available fMRI analysis tools such as SPM or FSL. Instead of dividing the analysis into two stages of single-subject analysis on the first level and group analysis on the second one, the presented statistical analysis combines both levels and represents a dedicated model suitable for the pursued approach of repeated measurements, which is scarce in the fMRI neuroscience literature [200, 201]. In this way session-specific effects are accounted for and statistical parameters are estimated in one combined model which contains all BOLD time series and pain rating data. With the standard two-level approach, group results mark the 'final' analysis results, which might be the reason for the low number of reported subject-level results in fMRI literature. Emphasis must be put on the importance of a more patient-centered approach in neuroscience by repeatedly recording and analysing single patients [6]. The continuous suffering from pain for many years revealed that each patient shows an unique pattern of cortical pain encoding, which can be considered as an individual signature of chronic pain processing.
The correction for multiple comparisons with surrogate data has the advantage of keeping the naturally evolving data structure intact. Instead of using a potential healthy control group or a resting-state recording with random pain ratings, the surrogate data were uncorrelated to the

original data, but had the same autocorrelation structure, amplitudes, and variance. In this way the main features of the data were preserved but the timing of the rating was randomised, i.e. the main features of the behavioural data were unrelated to the time course of the imaging data. This approach has been previously utilised for the analysis of time series data but is utilized here for the first time for a continuous pain-rating fMRI design [115, 271].

AMP across both patient groups

Across all CBP patients and sessions the intensity of pain is mainly encoded in the AIC, the frontal operculum, and the pons. These regions exhibit a positive relationship between cortical activity and the amplitude of continuous pain ratings: higher intensities of pain are accompanied by higher cortical activity. Additionally, higher intensities of endogenous pain in CBP are related to decreased activity in the PCC, pACC, the precuneus, the hippocampus, and several frontal and occipital regions. This network of brain regions is largely overlapping with the NPS [295], but contradicts findings from previous work that located the encoding of endogenous chronic lower back pain predominantly in frontal regions [28, 118, 119].

For the encoding of the pain intensity in CM, a positive relationship between pain intensity and cortical activity was found predominantly in the cerebellum, as well as in the frontal orbital cortex and in the fusiform cortex. Similar to the CBP patients, negative relationships between pain intensity and brain activity in the PCC, pACC and the precuneus, as well as in the amygdala and the subcallosal cortex were found. No cortical regions within the NPS network were found [295]. The absence of any single NPS region that codes for pain intensity in CM underlines the complex pathophysiology of the disease [51, 79]. In line with the initial hypothesis, a patient-specific pattern of the cortical intensity coding of CM, which is not reflected in the group statistics was observed; this is echoed in the individual profiles of endogenous pain processing in each CBP patient. In other words, there are a number of regions that encode the pain intensity in chronic migraine; these regions are, however, specific for an individual and not commonly shared by all patients.

Most imaging studies so far apply external (trigeminal) stimuli to elicit additional pain [272, 273] – the results are therefore not directly comparable with the here obtained results. Additionally, most of these studies investigated episodic migraine patients. In contrast, this study investigated patients suffering from chronic migraine who were examined during attack-free phases. Patients were continuously evaluating different levels of their daily endogenous pain without any external nociceptive input. The few fMRI studies on chronic migraine suggest functional, structural, and neurochemical alterations of cortical and subcortical regions [162, 210, 223, 252] and networks [10, 11, 70] compared to episodic migraineurs or healthy controls. In line with these findings, the results presented here may point to a neuronal reorganisation in chronic migraine patients which is specific for each individual.

SLP across both patient groups

The processing of pain intensity changes of endogenous pain in CBP patients is mainly located in the AIC and in frontal regions. Regions that show increased activity during falling pain were found in the occipital lobe (occipital pole, lateral occipital cortex) the PCC, pACC and precuneus. For CM patients, positive relations were located in the AIC and the cerebellum.

Besides occipital regions, negative relations were found in the precuneus and the angular gyrus.

Baliki and colleagues reported similarly increased activity in the right AIC and the cerebellum, but showed additional activity in the posterior insula, S2, multiple portions of the middle cingulate cortex, and S1 [28]. However, these findings apply to periods of increasing pain contrasted to both periods of stable and decreasing pain. As a result of not distinguishing between, what is referred to in this work as SLP and $aSLP$, the analyzed periods of increasing pain are more influenced by pain-unspecific effects of motor activity and decision-making. These aspects of motor activity and decision-making were specifically controlled for in this study by including the contrast between time periods of rising and falling pain. Periods of rising and falling pain share the motor activity of regulating the slider to indicate the change in pain intensity, which therefore vanishes in the direct contrast of these time intervals. The analysis of pain changes can be considered as independent from the analysis of pain amplitude: increasing pain can occur at both high and low levels of pain. The regions that encode the change of pain experience could have an impact on the emotional well-being of pain patients and would be a valuable target for therapeutic interventions such as neurofeedback.

The role of the anterior insula for the processing of chronic pain
For both pain diseases, the largest cortical effect for pain direction encoding (SLP) was found in the AIC; rising endogenous pain is accompanied by increasing insular activity. Interestingly, for CBP the AIC is processing the intensity (AMP) and the change of pain intensity (SLP). However, the encoding of intensity exhibits a different temporal profile and has its peak after the processing change detection. Therefore, the activity of the AIC for amplitude and change of amplitude is overlapping and is determined by a summation of the activity for the current pain intensity and the transient activity for rising (plus) or falling (minus) pain. The results of the present investigation, in particular the contribution of the AIC, does not exclude that chronic pain patients suffer from emotional problems [28, 120], but militates against opinions that the transitions to chronic pain might be reflected by a shift from insular processes to frontal areas. These findings argue against suggestions that chronic pain may have become decoupled from the sensory aspects but are purely emotional.

Individual patterns of pain intensity encoding in single patients
A main focus of this investigation is the assessment of individual (patient-specific) profiles of pain processing. In order to disentangle unique activation patterns of pain processing, each pain patient was recorded four times. As a result, the individual maps differ remarkably from each other and a substantial variation for the correlation of single patient signatures with the activity pattern from the groups statistics was found. For CBP, the activity of the prominent regions of the group statistics may have been driven by the few patients who exhibit strong effects in the AIC and the pACC. The importance of assessing individual patterns of brain structure and activity has been suggested previously [183]. In a similar vein, it was shown in EEG measurements that, although group statistics suggest otherwise, individual parameters of gamma oscillations in tonic and chronic pain are not encoded by gamma activity in all study participants [185, 255]. The enormous variability of the individual pain signatures indicates qualitative rather than quantitative differences between patients [317].

Indeed, the different pain signatures in the present study depicts a complex picture: even if all patients had a marginal (and positively correlated) contribution of the e.g. insular cortex (which they do not have), one must assume that the major weight for the encoding of pain for most patients relies on the processing in different brain regions. The variety of cortical processing is in line with the clinical picture of pain diseases, in which each individual exhibits a complex composite of specific characteristics [268]. The lack of significant and consistent positively correlated insular activity in most patients is suggested to be caused by qualitative rather than gradual differences between patients and would make the interpretation of quantitative effects challenging. The question is whether it is possible and plausible that the encoding of pain in the insula (or any other region) can be modulated (e.g. by parameters like depression) in a way that some patients have a positive correlation between pain and brain activity while some other patients would have negative relationships between brain activity and pain. The same applies for the pACC, which is considered to be a main hub of the descending pain control system. The group results suggest a negative relationship, but some individuals exhibit a positive relationship between the pACC and pain intensity, which would turn this region into a pain facilitation region rather than a pain inhibition hub. It remains to be verified if some factors reverse the relationship between cortical activity and pain intensity. The plausibility of this potential phenomenon decides whether a correlation or modulation of any factor with the present variety of cortical maps is justified.

Limitations and Conclusion

This investigation included a large sample of patients with repeated recordings and although the entire data amounts to more than 100 minutes of pain encoding data for each single patient, the following limitations need to be considered.

The majority of patients were on different types of prescribed medication which could have had an effect on the BOLD fluctuations. In addition, even the four fMRI recordings for each patient might not be enough to assess the stable and invariant pain signature of an individual. Similarly, the statistics on single patients might have been driven by a subset of the four recordings. The temporal stability of the individual pattern of pain-related cortical activity across four recordings was not investigated separately, as different statistical approaches and methodologies would be required. Repeated measurements were mainly acquired to extend the amount of fMRI data to increase robustness of the fMRI measurements. A supervised machine learning approach was applied (see section 9.5) to investigate the stability of the fMRI pain ratings and accompanied BOLD activations.

The present study expands the knowledge on the cortical underpinnings of chronic pain by showing that individuals exhibit their own signature of cortical processing of chronic pain, in chronic back pain as well as chronic migraine subjects. Further studies are needed to explore whether the current findings on individual pain signatures can be utilized for interventions that aim to directly modulate brain activity, e.g. neurofeedback [61].

9.4 Connectivity analysis in chronic back pain and chronic migraine patients

9.4.1 ROI analysis and additional preprocessing for connectivity analysis

In contrast to the BOLD analysis in the previous section 9.3, connectivity analysis was not based on voxel-wise analysis but on the parcellation of brain regions. Brain parcellations combine all voxels into several distinct homogeneous brain areas, which allows for a more robust and reproducible analysis. Additionally, compared to a voxel-based analysis, brain parcellations reduce the dimensionality of the data and increase signal-to-noise ratio [50, 63, 103]. Several brain parcellations are available (e.g., [248, 280]), the most extensive one by the human connectome project by Glasser [103]. Here, the brain is subdivided into 360 brain regions, 180 for each hemisphere, based on a multi-modal dataset using architecture, function, connectivity and topography to define individual brain regions. For the present study, 21 additional subcortical areas were added for a more detailed analysis (Table 9.4). To investigate the role of involvement of the cerebellum in pain processing, 27 regions in the cerebellum (Table 9.5) were added to the analysis as well. A principal component analysis (PCA) was applied to each of the 408 individual regions and the first principal component was taken for further analysis [225].

Structure	**x**	**y**	**z**
accumbens L/R	-7/8	9/11	-8
amygdala L/R	-23/24	-5/-4	-20
brainstem	0	-30	-30
hippocampus L/R	-25/26	-23/-22	-14
pallidum L/R	-19/20	-4	-2
thalamus L/R	-11/12	-19/-18	6
hypothalamus ASL	6	0	-12
hypothalamus sphere	6	-6	-12
LC bilat.	3	-38	-23
caudate L/R	-13/14	9/10	10/11
putamen L/R	-25/26	0/2	1/0
PAG	1	-34	-8
pons sphere2	4	-20	-20
spinal sphere	6	-40	-46

Table 9.4: Additional subcortical structures with MNI coordinates (left L/right R) of the center of the structure. Table and legend taken from [188].

For connectivity analysis, additional scrubbing and censoring was applied to minimize changes in connectivity related to motion. Outliers in the fMRI data were labelled as such, based on the definition of framewise displacement (FD) and DVARS introduced in section 5.3.2. A volume is defined as an outlier if it exceeds one of the following thresholds: FD $\geq$ 0.2 mm or DVARS $\geq$ (the 75th percentile + 1.5 times the interquartile range)[86]. Outliers are marked for each subject and then included in the regression as a vector of zeros (non-outlier) and ones (outlier). Each 'window' in the sliding-window analysis (see section 9.4.2) was additionally scrubbed for outliers using Grubbs's test at significance level $\alpha = 0.05$; windows with more than two outliers

were excluded from further analysis, including the preceding and following one. Windows with a correlation coefficient $r > 0.99$ were omitted because these high correlations were mainly driven by outliers. The average percentage of scrubbed timepoints for all region pairs was 0.3 $\pm$ 0.6 % for CBP and 0.3 $\pm$ 0.4 % for CM.
MCFLIRT motion parameters as well as their squares and temporal derivatives with squares (total of 24 regressors) were included as motion regressors. The pain rating vector, the rate of change vector, and the absolute value of the rate of change vector were convolved with the hemodynamic response function given in section 9.2.4 and also included as regressors. A schematic illustration of different time courses involved in the preprocessing is given in Figure 9.9.

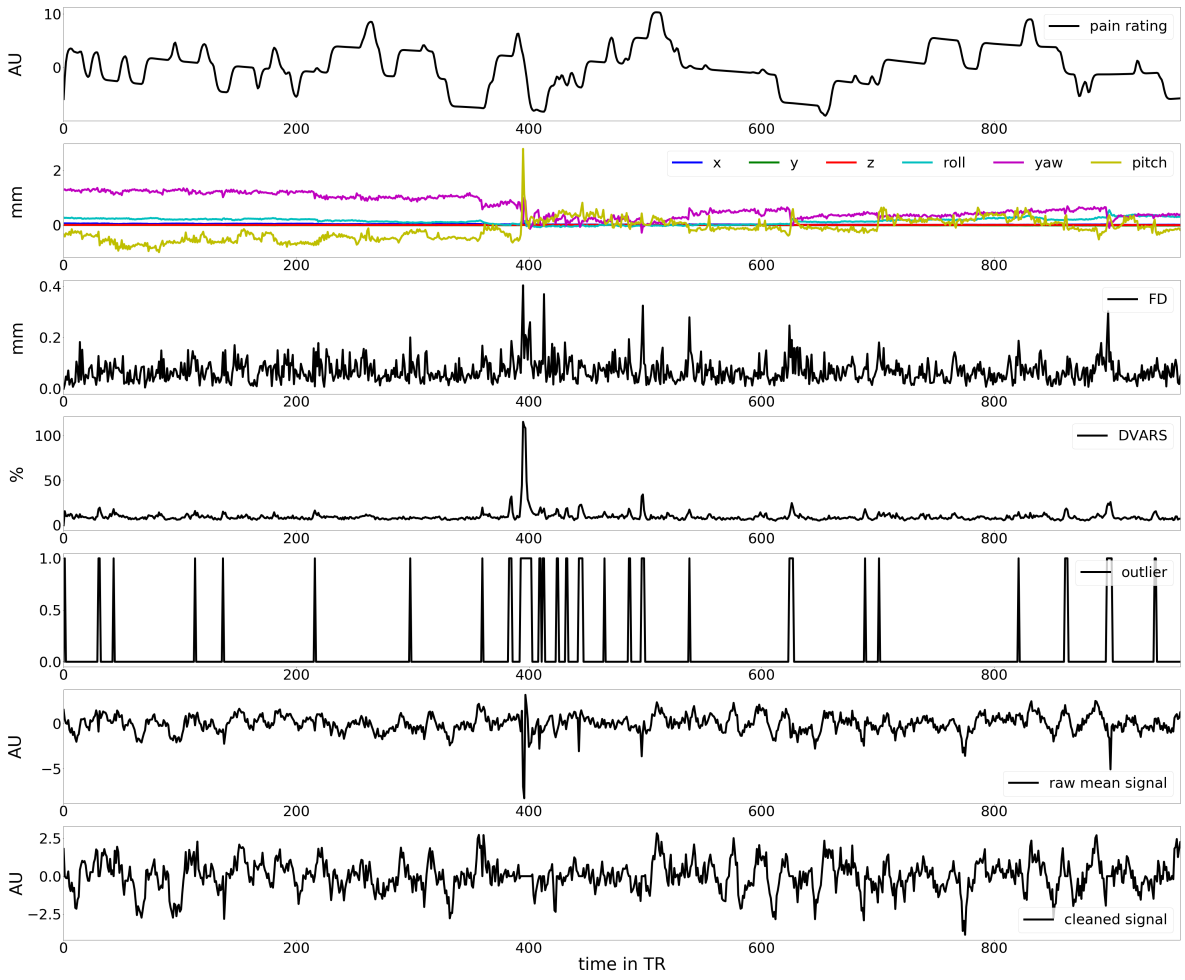

Figure 9.9: Schematic illustration of the different time courses of the pain rating, the MCFLIRT movement parameters (x, y, z, roll, yaw, pitch), the framewise displacement (FD), the DVARS, the identified outliers, the raw BOLD signal as a mean over the region and the 'cleaned' preprocessed time course.

Structure	x	y	z
I-IV L/R	-7/10	-44/-43	-17/-18
V L/R	-13/14	-50/-51	-19
VI L/R	-23/24	-59/-58	-25
Vermis VI	1	-71	-21
Crus I L/R	-36/38	-68	-32
Crus II L/R	-26/26	-75/-76	-42/-41
Vermis Crus II	0	-75	-31
VIIb L/R	-26/28	-66/-65	-51/-50
Vermis VIIb	0	-68	-31
VIIIa L/R	-24/26	-57/-58	-53
Vermis VIIIa	0	-67	-38
VIIIb L/R	-17/18	-50/-51	-55
Vermis VIIIb	0	-63	-42
IX L/R	-7/7	-53	-48
Vermis IX	0	-56	-37
X L/R	-21/22	-37	-45/-46
Vermis X	22	-37	-46

Table 9.5: Cerebellum subregions with MNI coordinates (left L/right R) of the center of the structure. Table and legend taken from [188].

9.4.2 Sliding-window and statistical analysis for connectivity

A whole-brain exploratory approach was applied, computing correlations between all extracted time courses (i.e., between the first PCA components of the signal) from all pairs of 408 regions. A visualisation of a schematic overview of the following description of the sliding-window approach is given in Figure 9.10.
The coherence of the time courses between two regions (Figure 9.10 A) was determined by Pearson's (full) correlation coefficient R over sliding windows of window length = 10 data points (t = TR $\cdot$ 10 = 15 s) from -4 to 4 data points and an offset of one data point (see section 6.2). This resulted in nine correlations for each of the 950 data points (Figure 9.10 B). For the relationship between the correlation strength of two regions and the pain ratings (Figure 9.10 C), the rating vector was shifted in the same manner as described above (section 9.3.1), between -15 s and 20 s with offsets of 1 s (36 total correlations) against the correlation time course. The whole sliding-window approach thus generated $9 \times 36 \times 950$ dynamical functional connectivity matrices of dimensions 408×408 for each subject and session (Figure 9.10 D). Fisher's z-transformation was used for the normalisation of the correlation coefficients. The same steps were applied to the corresponding rate of change and absolute rate of change vectors.

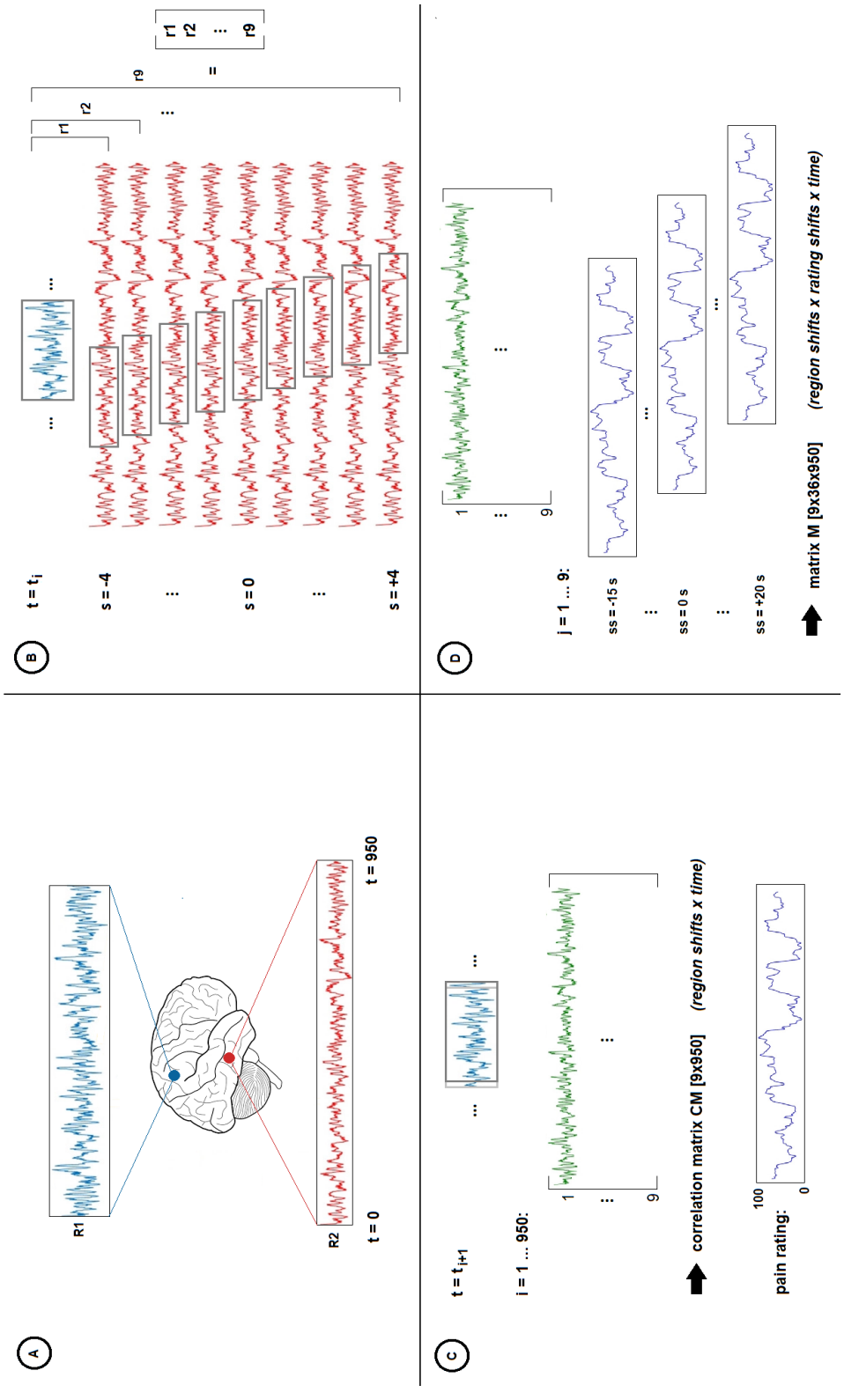

Figure 9.10: Schematic illustration of the sliding window approach in four steps (A–D) for two ROIs (R1 blue and R2 red); adapted from [247].

Using Linear Mixed Effects models (LME; MixedModels.jl package in Julia; [38]), the relationship between fluctuating pain intensity and the fluctuating cortical connectivity was determined separately for each pair of brain regions. The fluctuating connectivity of a particular pair is modelled through the time course of the three variables (AMP, SLP, aSLP) derived from the pain ratings. The statistical model is given by

$$\begin{aligned} connectivity \sim 1 + AMP + SLP + aSLP + \\ + (AMP - 1|session) + (SLP - 1|session) + (aSLP - 1|session) \end{aligned} \tag{9.4}$$

All statistical tests were corrected for multiple testing (connections, time shifts, rating shifts) and autocorrelation in the behavioural data: 1000 surrogate time courses were created using the IAAFT algorithm (Iterative Amplitude Adjusted Fourier Transform) from the original rating data, which were uncorrelated to the original rating data but had the same autocorrelation structure as the original data [251]. Using the surrogate data, the entire LME analysis was

CBP			
subject	**AMP**	**SLP**	**aSLP**
1	10.83	9.26	9.22
2	11.06	9.33	8.55
3	10.63	7.91	8.21
4	10.85	8.88	8.45
5	11.65	9.37	8.26
6	10.62	7.56	8.40
7	9.83	7.61	9.03
8	11.18	9.29	8.53
9	9.06	9.77	7.09
10	11.00	8.11	8.47
11	11.82	9.50	8.29
12	10.85	9.00	8.37
13	11.45	8.20	9.49
14	10.19	9.63	8.03
15	10.62	9.50	9.68
16	11.49	9.73	8.87
17	11.01	9.70	8.72
18	10.61	9.87	7.46
19	10.42	8.36	7.98
20	10.59	5.54	7.31
group	4.77	6.97	6.98

CM			
subject	**AMP**	**SLP**	**aSLP**
1	12.27	9.98	8.90
2	11.26	9.40	8.93
3	11.05	9.19	8.68
4	11.39	9.17	9.11
5	11.18	9.09	8.36
6	10.20	8.92	7.28
7	11.15	8.79	8.34
8	11.26	9.04	8.73
9	10.73	9.48	8.30
10	11.36	9.20	8.41
11	11.67	8.85	9.10
12	12.45	9.63	8.53
13	11.20	9.60	8.82
14	10.84	8.52	8.33
15	10.96	6.08	7.92
16	11.32	8.34	8.95
17	11.21	8.49	9.01
18	10.70	7.97	8.59
19	10.95	7.90	8.30
20	11.10	9.42	8.61
group	4.81	7.27	7.18

Table 9.6: Statistical thresholds for connectivity analysis: t-values for CBP and CM patients as determined by PALM [305] for single subject and group analysis.

repeated 1000 times for the vectors (AMP, SLP, aSLP) with zero shift, resulting in 1000 statistical maps for AMP, SLP and aSLP, respectively. From each map the highest absolute t-values of each repetition across the whole volume was extracted, which resulted in a right-skewed distribution of 1000 values for each condition [256]. Based on the distributions of 1000 values (for AMP, SLP, aSLP), the statistical thresholds were determined using PALM [304, 305]. The statistical thresholds for the group and single subject analysis are given in Table 9.6.

9.4.3 Connectivity schemata

For the analysis, positive and negative relationships between functional connectivity and pain intensity ratings were considered as follows (see Figure 9.11 A–C). After the calculation of the correlation between the BOLD timeseries of two brain regions with the sliding window approach, the resulting time course of correlations can be considered in three ways: as mostly consisting of negative (Figure 9.11 A), mixed (Figure 9.11 B) or positive (Figure 9.11 C) coefficients r. A correlation coefficient of $r = 0$ is indicated by a vertical dashed line in Figure 9.11.
The resulting time course of 'connectivity' correlations (corresponding to the green time courses in Figure 9.10) was then correlated with the pain intensity ratings (corresponding to the blue time courses in Figure 9.10) of the patients, which can be divided into a positive (solid lines in Figure 9.11) or negative (dashed lines in Figure 9.11) relationship.

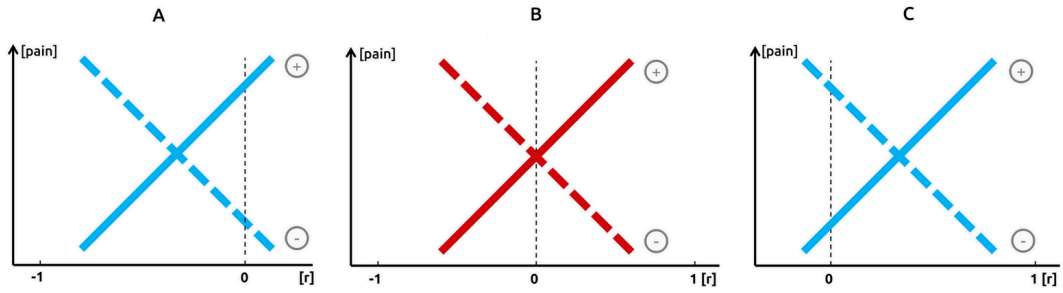

Figure 9.11: Connectivity schemata: Ratings of different *pain* intensity levels on the y-axis are plotted against the correlation coefficient r between two ROIs. Whereas mostly positive (A) or negative (C) pain-related connectivity was considered, a mixture of positive and negative correlations (B) was not considered in the analysis. Figure and legend taken from [188].

In a first case (Figure 9.11 A), pain-related effects may occur for pairs of brain regions that are largely anti-correlated, which is reflected as a negative correlation coefficient r on the x-axis. A positive relationship (solid line) with pain intensity would imply a drop of anti-correlation for high pain. Here, low pain states are likely related to suppression effects. This might be the case for "cognitive" brain regions that suppress pain-related insular activity; less activity in these regions and a subsequent disruption of suppression and collapsing anti-correlation would increase pain. For negative pain-related relationships (dashed line) high pain is bound to highly anti-correlated connections; high pain is related to a strong anti-correlation and a suppression effect between brain regions. Higher pain intensities may inhibit frontal brain regions which in turn control behaviour that is involved in the maintenance of pain, e.g. pain-related rumination and hypervigilance on pain. However, no significant effects for anti-correlated brain regions were found.

In a second case (Figure 9.11 B), data would cross the boundary between positive and negative correlation coefficients. These cases were found as non-interpretable, particularly the absence of cortical connectivity for mid-range pain intensities.

In a third case (Figure 9.11 C), the relationship between pain intensity and functional connectivity occurs for brain regions that are largely correlated, reflected by a positive correlation

coefficient r on the x-axis. For positive relationships with pain intensity (solid line), high-pain states are bound to higher connectivities. The perception of pain may require a crosstalk between two brain regions. A disruption of the crosstalk would lower the intensity of pain. For negative pain-related relationships (dashed line), high pain states are associated with an decrease of cortical connections. This may occur when one brain region suppresses the processes of the other brain region, e.g. the top-down modulation of the pACC on the PAG. Due to potential noise in the data, an overlap of 20 % towards sections of the data with negative correlation coefficients was allowed.

9.4.4 Connectivity: Chronic back pain (CBP)

In total, 83 connections were found to be significant for the encoding of pain intensity, 94 for the encoding of the change of pain intensity and 3696 for the encoding of the slider movement. No anticorrelations (connectivity schemata 9.11 A) were found and the following results focus on the positive correlations between the two corresponding brain areas and positive (connectivity schemata 9.11 C+, solid line) and negative (connectivity schemata 9.11 C–, dashed line) relationships to the pain rating. Connectivity confusion matrices for AMP and SLP are given in Figure 9.12.

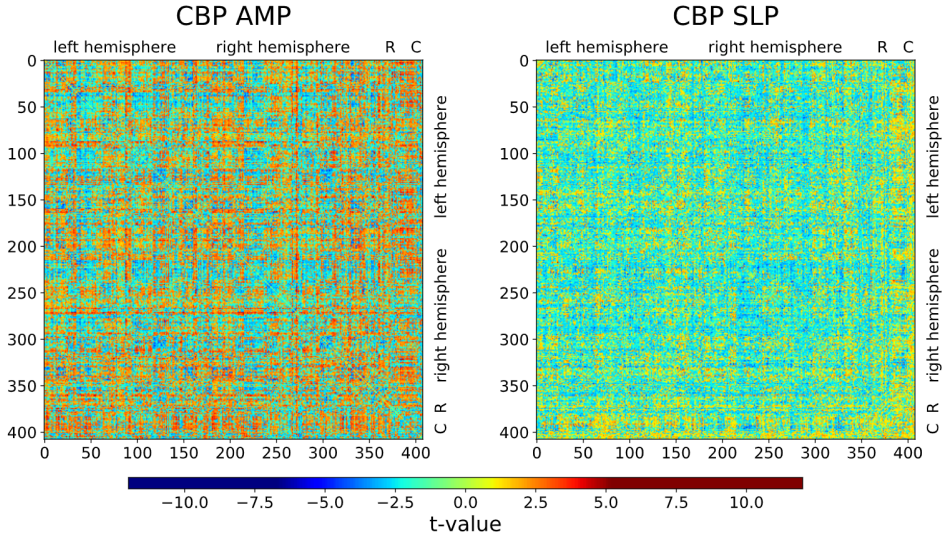

Figure 9.12: Connectivity confusion matrices for the encoding of pain intensity (AMP) and the change in pain intensity (SLP) for CBP patients for all 408 region pairs given in t-values: 1-180: left hemisphere, 181-360: right hemisphere; 361-381: R: additional regions; 382-408: C: cerebellum. AMP shows 70 % negative and 30 % positive significant t-values; the confusion matrix for SLP shows even more negative (74 %) than positive (26 %) ones. Figure and legend taken from [188].

Connectivity: Encoding of pain intensity across all CBP patients (AMP)

Across all subjects and sessions, two connections were found to be positively related to the intensity of the endogenous pain (Figure 9.13); these pairs of brain regions, consisting of connections between cerebellar and parietal brain regions, showed a higher connectivity with higher levels of pain intensity. In addition 42 pairs of brain regions that exhibited a negative relation-

# of connections	area description	area name	hemisphere
4	medial area 7P	7Pm	L
4	area lateral occipital 2	LO2	L
4	area lateral occipital 2	LO2	R
3	area 31pd	31pd	L
3	medial superior temporal Area	MST	R
3	area lateral occipital 3	LO3	R
3	middle temporal area	MT	R
3	area V4t	V4t	R
2	area 7m	7m	R
2	dorsal transitional visual area	DVT	L
2	lateral area 7P	7PL	L
2	medial area 7A	7Am	R
2	area lateral intraparietal ventral	LIPv	L
2	premotor eye field	PEF	R
2	parahippocampal area 1	PHA1	R
2	parahippocampal area 3	PHA3	R
2	auditory 5 complex	A5	R
2	seventh visual area	V7	L
2	area V4t	V4t	L
2	area V6A	V6A	R

Table 9.7: Connectivity: CBP AMP brain regions with more than two connections. Table and legend taken from [188].

ship between cortical connectivity and pain intensity were found. These pairs showed a lower connectivity with higher levels of experienced pain. One pattern of connectivity is related to the occipital cortex, where an overall disconnection within the lobe for higher pain states can be observed. Further disruptions of connectivity have been observed in limbic (hippocampal, parahippocampal), precuneus (BA7), and cingulate areas (BA23 and BA31). All 44 significant connections exhibited pain-related connectivity changes for positively correlated brain regions, i.e. the sliding-window approach resulted in a time series of mostly positive correlation coefficients. There was no significant effect for connections that relied on anti-correlated brain regions. Regions with more than one connection are listed in Table 9.7.

Connectivity: Encoding of the change of pain intensity across all CBP patients (SLP)

Across all subjects and sessions, nine connections were found to be positively related to the direction of change of the endogenous pain intensity (Figure 9.14). These pairs of brain regions showed increasing connectivity with rising pain intensity and include interhemispheric and left-lateralized intrahemispheric occipital connections as well as connections between right angular and somatosensory regions. However, the majority of the significantly connected brain regions exhibited a negative relationship between cortical connectivity and change of pain intensity. These 35 pairs showed decreasing connectivity with increasing levels of experienced pain. In other words, increasing pain is predominantly bound to a progressive loss of connectivity. This applies to connections that involve left parietal opercular regions, right insular regions, as well as large parts of the parietal, cingular and motor cortices. Again, the entire statistics largely

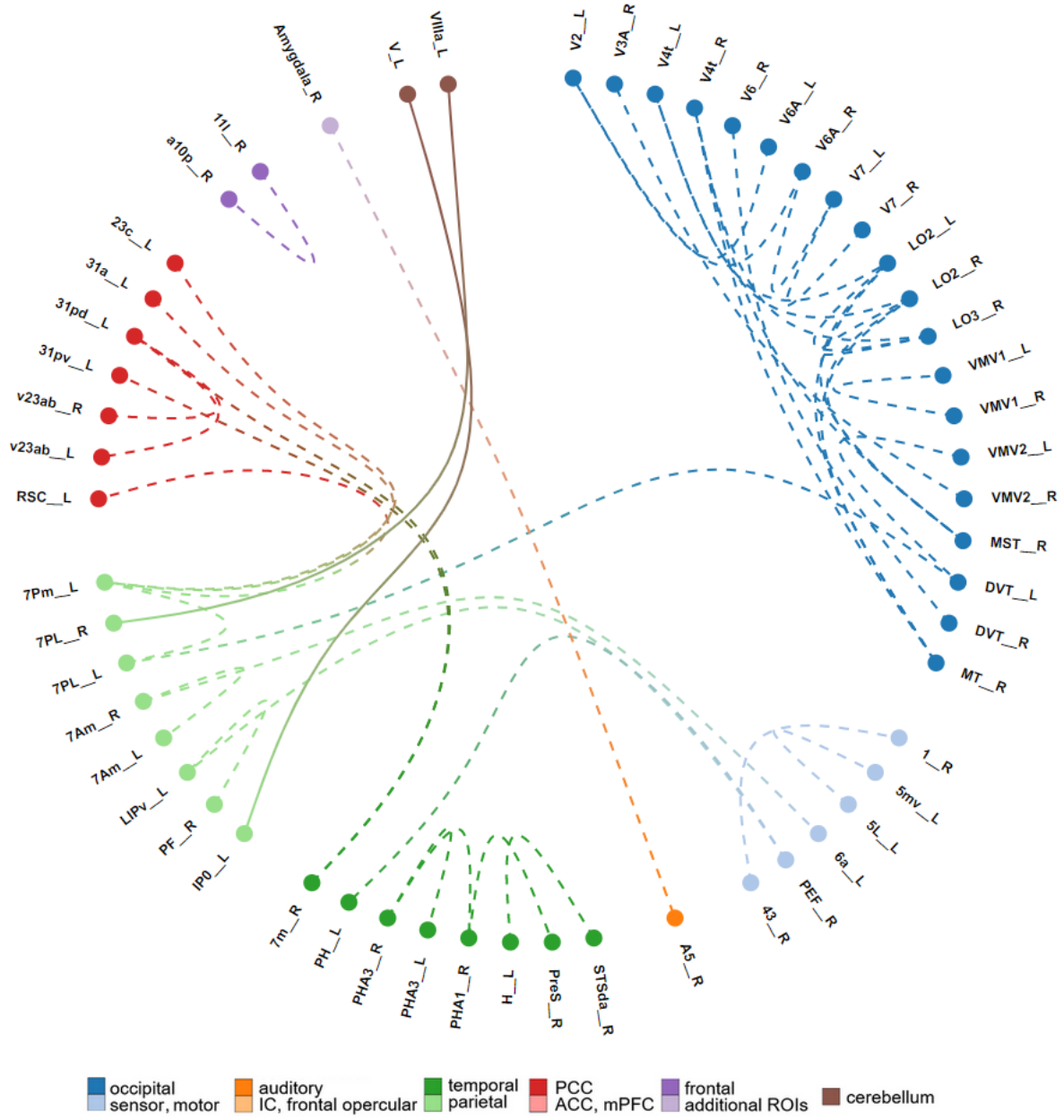

Figure 9.13: CBP Connectivity pain intensity (AMP) encoding: Dashed lines indicate negative relationships with pain intensity; solid lines indicate positive relationships with pain intensity. Figure and legend taken from [188].

relied on a time course of positive correlation coefficients between brain regions. There was no significant effect for connections that relied on anti-correlated brain regions. Regions with more than one connection are listed in Table 9.8.

# of connections	area description	area name	hemisphere
3	area 6m anterior	6ma	R
3	area 6 anterior	6a	R
3	area V6A	V6A	R
3	area V6A	V6A	L
2	area 1 (primary somatosensory cortex)	1	R
2	primary motor cortex	4	R
2	middle temporal area	MT	L
2	posterior inferotemporal	PIT	L
2	area OP1/SII	OP1	L
2	area OP2-3/VS	OP2-3	L
2	area OP4/PV	OP4	L
2	area temporo parieto occipital junction 3	TPOJ3	R
2	lateral belt complex	LBelt	R
2	area PH	PH	L
2	area lateral intraparietal ventral	LIPv	R
2	area lateral intraparietal ventral	LIPv	L
2	anterior intraparietal area	AIP	R
2	area 7PC	7PC	R
2	area 46	46	R

Table 9.8: Connectivity: CBP SLP brain regions with more than two connections. Table and legend taken from [188].

Connectivity: Processing of motor activity and decision making across all CBP patients (aSLP)

For the encoding of motor activity and decision making the regions with the most connections are given in Table 9.9. The most connected regions shown in Table 9.9 have more than or equal to 83 connections and are mainly found in the frontal cortex.

9.4.5 Connectivity: Chronic migraine (CM)

In total 12 connections were found to be significant for the encoding of pain intensity, 79 for the encoding of the change of pain intensity and 12707 for the encoding of the slider movement. No anticorrelations (connectivity schemata 9.11 A) were found and the following results focus on the positive correlations between the two corresponding brain areas and positive (connectivity schemata 9.11 C+, solid line) and negative (connectivity schema 9.11 C–, dashed line) relationships to the pain rating. Connectivity confusion matrices for AMP and SLP are given in Figure 9.15.

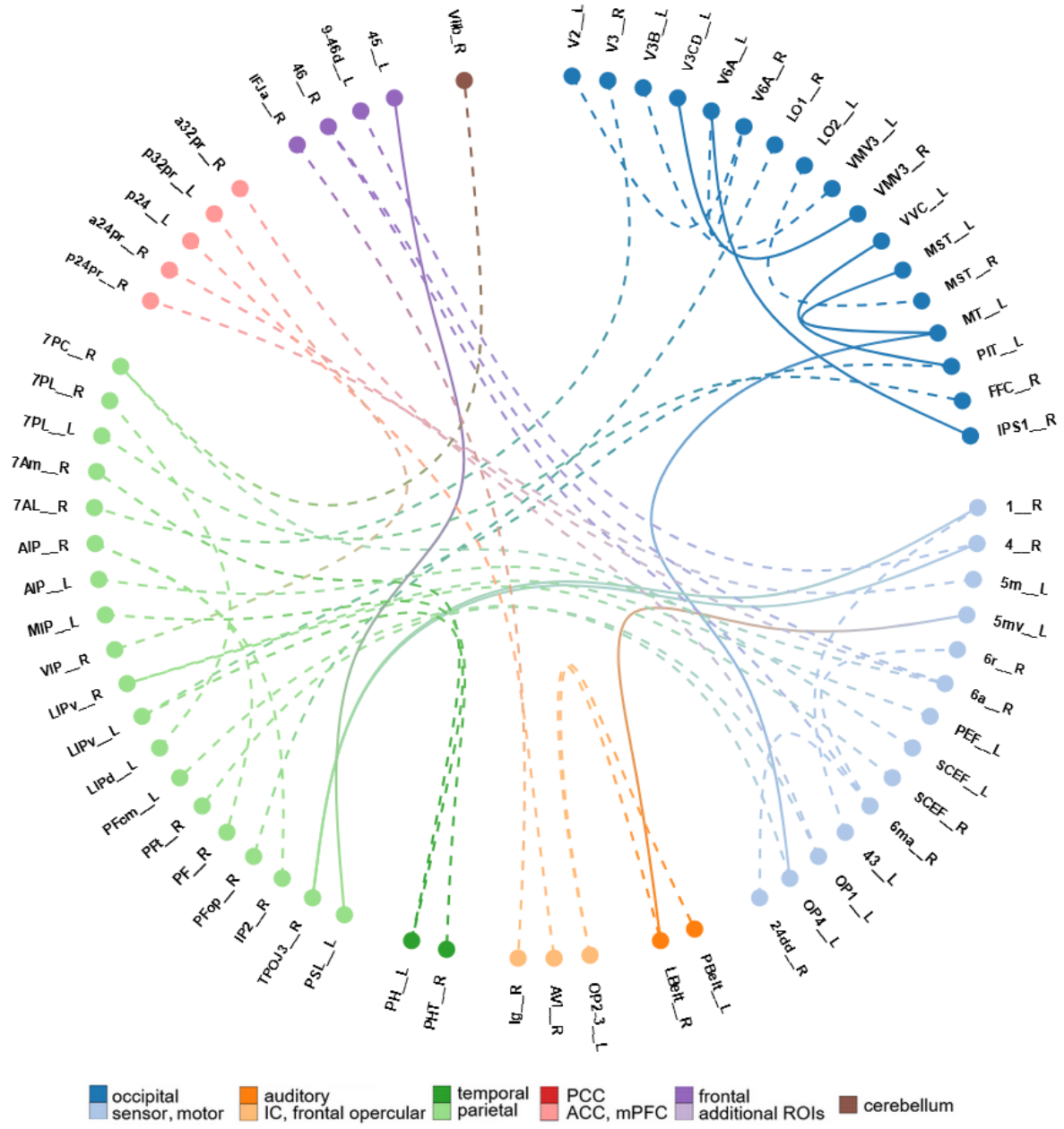

Figure 9.14: CBP connectivity change of pain (SLP) encoding: Dashed lines indicate negative relationships with pain intensity; solid lines indicate positive relationships with pain intensity. Figure and legend taken from [188].

# of connections	area description	area name	hemisphere
114	supplementary and cingulate eye field	SCEF	L
108	posterior inferotemporal complex	PIT	R
103	dorsal area 6	6d	L
100	area lateral occipital 2	LO2	L
100	frontal opercular area 4	FOP4	R
92	fusiform face complex	FFC	R
88	premotor eye field	PEF	R
86	posterior inferotemporal complex	PIT	L
85	supplementary and cingulate eye field	SCEF	R
83	frontal opercular area 4	FOP4	L

Table 9.9: Top 10 (corresponds to 70 %) of all significant regions with the most connections for the encoding of motor activity and decision making (aSLP) in CBP. Table and legend taken from [188].

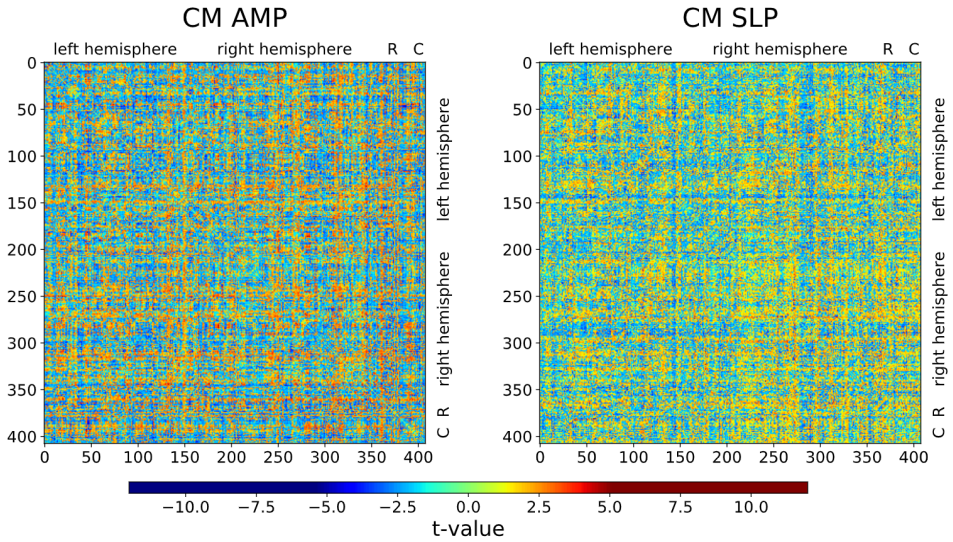

Figure 9.15: Confusion matrices for AMP and SLP for all 408 region pairs given in t-values: 1-180: left hemisphere, 181-360: right hemisphere; 361-381: additional regions (R); 382-408: cerebellum (C). The confusion matrix for AMP shows 25 % positive significant t-values, and 75 % negative ones, compared to SLP which shows more positive (58 %) than negative (42 %) ones. Figure and legend taken from [188].

Connectivity: Encoding of pain intensity across all CM patients (AMP)

For CM, only two connections (Figure 9.16) that exhibit a significant effect for the encoding of pain intensity were found: Decreasing connectivity for left motor regions (6d and 43) and increasing connectivity between the anterior insula and the orbitofrontal cortex (AVI and pOFC) indicate high pain intensity of CM.

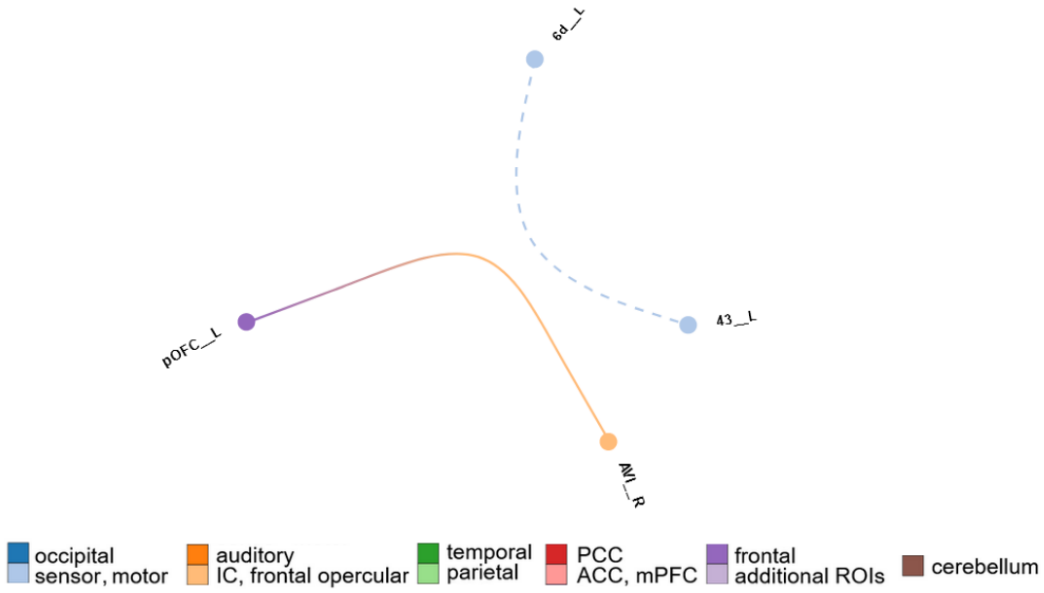

Figure 9.16: Connectivity: CM pain intensity encoding: The dashed line indicate a negative relationship with pain intensity; the solid line indicate a positive relationship with pain intensity. Figure and legend taken from [188].

Connectivity: Encoding of the change of pain intensity across all CM patients (SLP)

Across all subjects and sessions, four connections were found to be positively related to the change of intensity of the endogenous pain (Figure 9.17); these pairs of brain regions, e.g. consisting of connections between temporal regions with the left posterior insular and the hippocampus, showed increasing connectivity with increasing levels of pain intensity. In addition, 42 pairs of brain regions that exhibited a negative relationship between cortical connectivity and the change of pain intensity were found. These pairs showed decreasing connectivity with decreasing levels of experienced pain.

Connectivity: Processing of motor activity and decision making across all CM patients (aSLP)

The top ten most connected regions for the encoding of motor activity and decision making are given in Table 9.10. The most connected regions shown in Table 9.10 have more than or equal to 183 connections and are mainly found in the frontal and parietal cortex.

9.4.6 Individual connectivity results for CBP and CM

Single subject circle plots for the encoding of pain intensity (AMP) for all subjects and possible 408 regions are shown in Figures 9.18 and 9.19 for CBP and CM, respectively. The number of significant connections visualised in these circle plots for each individual subject for both patient groups are given in Table 9.11. The correlation between individual maps and the group results were calculated with Kendall's τ and are given in Table 9.12. The mean correlation between individual AMP maps and group AMP map for CBP/CM is $\tau = 0.09/0.07$, $\tau = 0.03/0.05$ for the SLP variable and $\tau = 0.09/0.10$ for the aSLP variable.

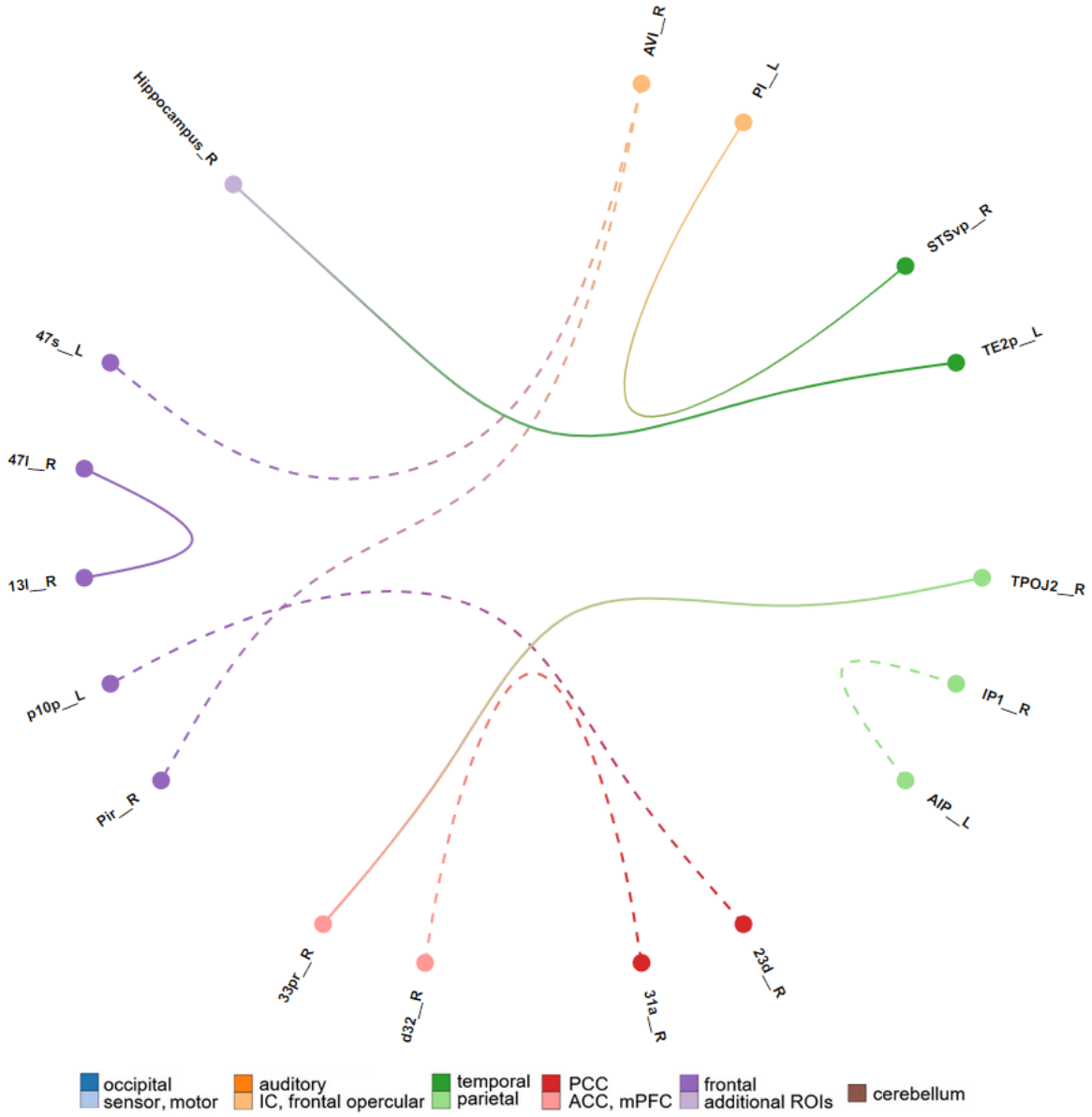

Figure 9.17: CM connectivity: change of pain encoding. Dashed lines indicate negative relationships with change of pain intensity; solid lines indicate positive relationships with change of pain intensity. Figure and legend taken from [188].

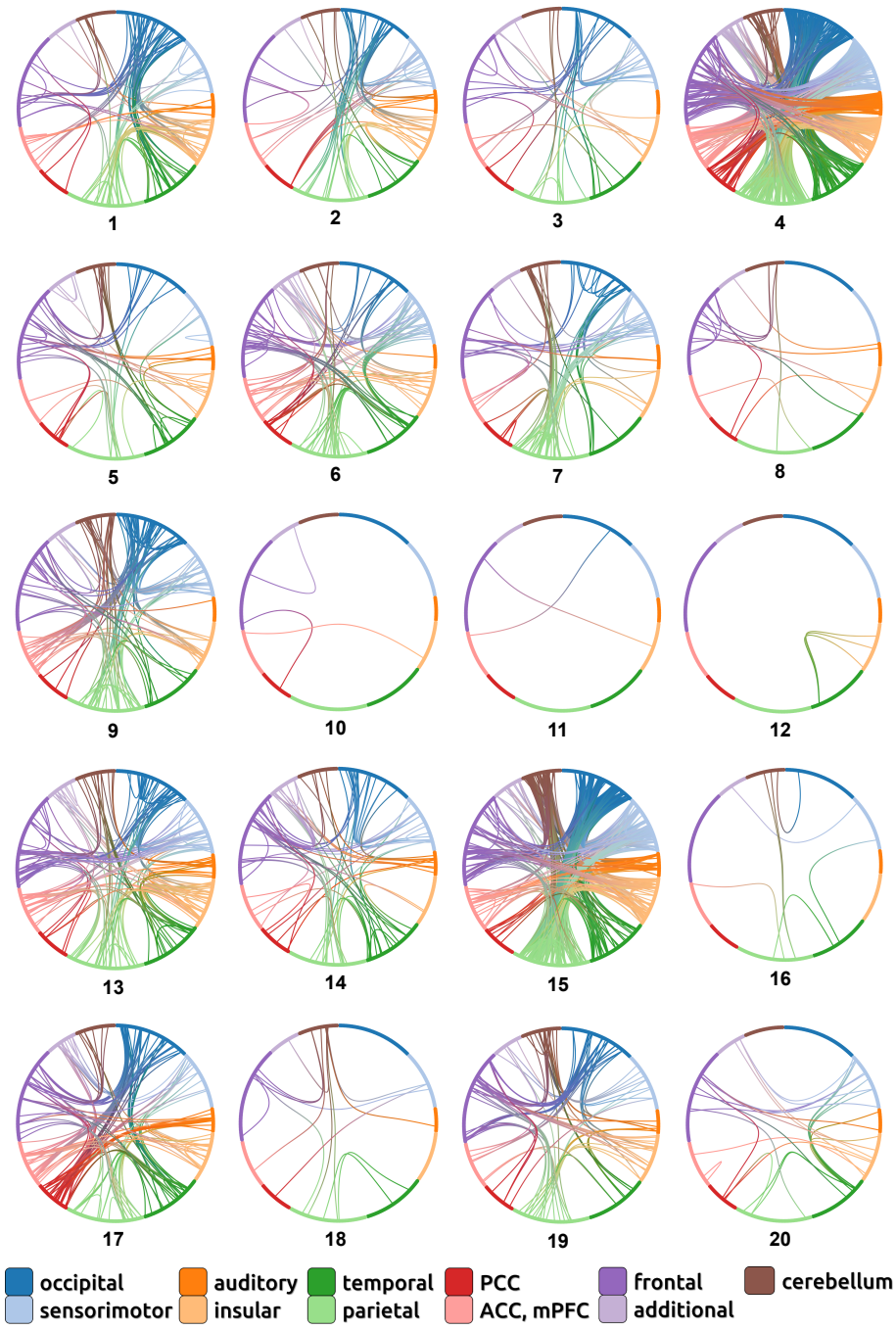

Figure 9.18: CBP individual circle plots patterns: The encoding of pain intensity (AMP) is shown for each of the 20 subjects individually for all 408 possible regions. Figure and legend taken from [188].

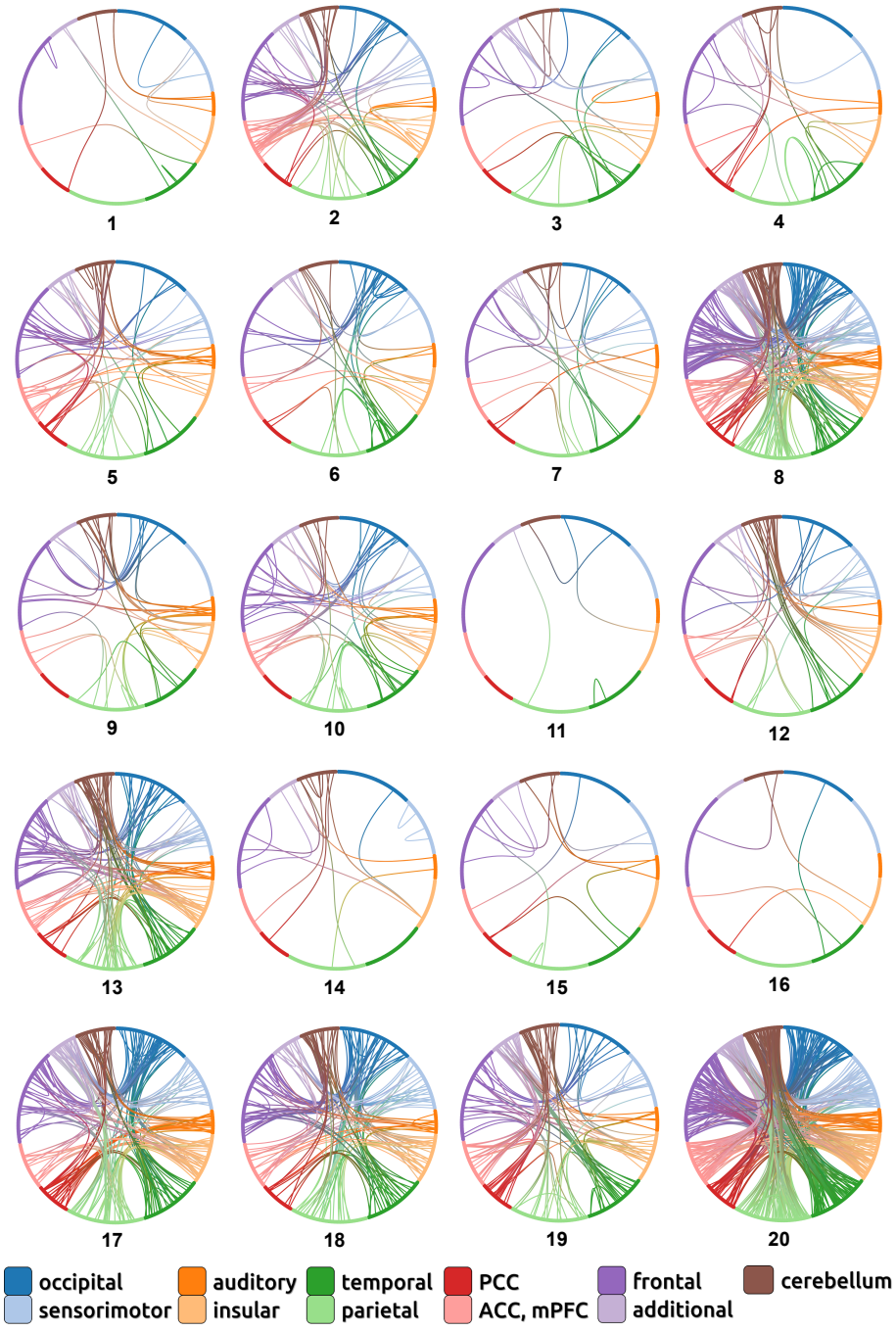

Figure 9.19: CM individual circle plots patterns: The encoding of pain intensity (AMP) is shown for each of the 20 subjects individually for all 408 possible regions. Figure and legend taken from [188].

# of connections	area description	area name	hemisphere
196	supplementary and cingulate eye field	SCEF	R
194	area anterior 32 prime	a32pr	R
192	area p32 prime	p32pr	R
190	area PFt	PFt	R
188	area PFt	PFt	L
188	premotor eye field	PEF	R
188	rostral area 6	6r	R
184	area PF opercular	PFop	R
183	area lateral occipital 2	LO2	R
183	area PH	PH	R

Table 9.10: Top 10 (corresponds to 93 %) of all significant regions with the most connections for the encoding of motor activity and decision making (aSLP) in CM. Table and legend taken from [188].

CBP				CM			
subject	AMP	SLP	aSLP	subject	AMP	SLP	aSLP
1	106	106	10	1	11	7	8402
2	65	13	475	2	70	29	10793
3	44	188	305	3	24	29	1369
4	1240	55	86	4	20	33	333
5	54	5	722	5	59	10	6596
6	109	462	167	6	41	1	37837
7	95	2284	1	7	24	59	4746
8	15	26	5026	8	255	460	5281
9	131	0	2775	9	36	2	856
10	20	55	62	10	52	14	148
11	2	4	4019	11	4	52	75
12	3	4	7015	12	39	163	1186
13	158	2716	58	13	128	32	8188
14	78	8	958	14	17	17	716
15	704	1437	33	15	12	5889	0
16	7	19	1187	16	5	66	8529
17	164	4	202	17	197	371	379
18	14	0	33564	18	151	2888	10
19	92	65	2528	19	112	583	172
20	26	5857	581	20	508	73	578

Table 9.11: Number of significant connections for every single subject for CBP and CM for the encoding of AMP, SLP and aSLP. Table and legend taken from [188].

9.4.7 Discussion of connectivity fMRI results in CBP and CM

Changes of cortical connectivity in relation to complementary aspects of the perception of ongoing chronic pain were investigated. A ten second sliding-window connectivity analysis was computed for the pair-wise and time-varying connectivity between all 408 parcellated brain regions across the entire fMRI recording period. Linear mixed effects models were fitted for each

CBP			
subject	**AMP**	**SLP**	**aSLP**
1	0.053	0.065	0.095
2	0.20	0.027	0.081
3	0.055	0.030	0.097
4	0.10	0.0044	-0.0084
5	0.043	-0.018	-0.027
6	0.12	-0.00032	0.22
7	0.085	0.072	0.075
8	0.14	0.027	0.14
9	0.039	0.0024	0.080
10	0.13	0.047	0.075
11	0.086	0.051	0.22
12	0.12	0.0015	0.084
13	0.068	0.11	0.061
14	0.099	0.034	0.082
15	-0.0079	0.12	0.022
16	0.089	0.0027	0.13
17	0.0036	0.034	0.022
18	0.10	-0.020	0.072
19	0.052	-0.019	0.16
20	0.14	0.068	0.040

CM			
subject	**AMP**	**SLP**	**aSLP**
1	0.12	0.070	0.20
2	0.093	0.061	0.27
3	0.017	0.0072	-0.050
4	0.022	0.050	0.12
5	0.076	0.0052	0.12
6	0.071	0.099	0.0046
7	0.12	0.063	0.084
8	0.096	0.0064	0.069
9	0.058	0.052	0.11
10	0.080	0.036	-0.026
11	0.085	0.073	0.079
12	0.15	0.050	0.16
13	0.040	0.027	0.13
14	0.16	0.098	0.089
15	0.033	0.054	0.076
16	0.095	-0.012	0.19
17	0.053	0.085	0.14
18	0.036	0.087	0.12
19	0.016	0.0085	0.075
20	0.056	0.035	-0.052

Table 9.12: Correlation between individual maps and group maps indicated by Kendall's τ. Table and legend taken from [188].

pair of brain regions to explore the relationship between cortical connectivity and the observed time course of the patients' fluctuating endogenous pain. Two pain processing entities were taken into account: different pain intensity levels and the direction of pain intensity changes (rising vs. falling pain). Positive and negative relationships between pain perception and positively correlated brain regions were revealed, but no effect for anticorrelated (i.e. suppressing) brain regions was found. As a result, distinct patterns of pain-related connectivity for CBP and CM for the encoding of the magnitude of pain intensity as well as for the encoding of the (directional, i.e. signed) change of pain intensity were revealed. Periods of high and increasing pain were predominantly related to low cortical connectivity. For CBP this applies to the pain intensity-related connectivity for limbic and cingulate areas, and for the precuneus. The change of pain intensity was encoded by connections in left parietal opercular regions, right insular regions, as well as large parts of the parietal, cingular and motor cortices. The change of pain intensity direction in CM was reflected by decreasing connectivity between the anterior insular cortex and orbitofrontal areas, as well as between the PCC and frontal and ACC regions.
Overall, the results resemble recent findings of reduced cortical connectivity for higher pain states as in Schulz et al. [257]. The analysis of the repeated single-subject connectivity maps suggests a more complex picture, indicating a unique pattern of pain-related cortical processing for each patient. The group findings will be discussed in a traditional fashion but the single subject analysis suggests that none of the group findings apply to the cortical processing of a single subject. The findings suggest rather qualitative than gradual differences between individual pain patients.

Methodological advances

The underlying principle of this part of this work, namely the combination of a continuous, event-free fMRI design with a whole-brain sliding-window dynamic FC approach has not been investigated before. This design enabled the investigation of the functional dynamics changes in communications between multiple pairs of brain regions, as well as their relationship with the pain rating in chronic pain patients. In contrast to resting-state designs, where static, averaged FC throughout the fMRI sessions are considered, the introduction of a two-stage sliding-window analysis enabled the extraction of maximally resolved information of the different underlying pain encoding processes. This approach raised the necessity for a new identification and characterisation of the functional connectivity identified with the presented connectivity scheme. This innovative approach in between resting-state and task-based design with such combination of analysis steps needed new methodological configurations and considerations for preprocessing and analysis discussed in the following.

Typical connectivity analyses usually select a seed-based correlation approach with 5 to 10 different ROIs modeled as spheres with different radius ($\sim$ 3–5 mm) around a chosen center of mass. These ROIs are specific and predefined to the investigated task, often based on expected results or previous investigations. Comparisons of results are therefore not straightforward as different centers of mass for the same brain region are often reported or definition of nodes for ROIs differ, i.e. if determined by structural or functional brain-atlases. Moreover with a limited number of ROIs in a seed-based approach the analysis can not incorporate all information present during the encoding task and is therefore not representable. Additional communications between e.g. two brain regions through an excluded third one, cannot be adequately reflected in the results. In contrast, the present work here was aimed at an exploratory analysis of the interconnections of all 408 brain regions of one of the more detailed brain atlases developed by the Human Connectome Project [103], seldom pursued due to the computational expense. The use of a predefined atlas additionally improves accuracy and reproducibility of the obtained results.
A combination of an ICA preprocessing approach and a PCA for each region was applied to extract the signal which most faithfully represents brain activity. PCA for fMRI analysis was investigated by e.g., Zhong et al. [319], who found increased SNR compared to calculating the mean over the voxels contained in one region in resting-state fMRI. Different principal components were investigated for several sample regions at an early stage of this work to ensure representative reflection of the task. Due to the preceding ICA, which included the time-consuming selection of noise components for each individual subject, signal fluctuations from physiological noise were already reduced and the first PC was chosen for further analysis. Future investigations may include several or different PCs to investigate their distinct contribution to the data as well as their neurological interpretation. Instead of region-specific analysis a data-driven approach with IC or PC could be investigated in the future to identify co-activation on a more functional network-base.

For the motion correction preprocessing and removal of outliers, recommendations for resting-state as well as task-based fMRI designs were combined to adequately fit the new requirements of the somewhat intermediate approach of the continuous pain rating. The inclusion of 24 movement parameters was motivated by previous investigations [67] to obtain nearly movement-free fMRI data which then was set in relationship to the pain intensity rating. No subtraction of

the global mean signal was applied, as there are no standardized recommendations in the literature and this is still a highly discussed and active field of research [229, 246]. Both advantages in global signal removal, as well as e.g. the introduction of artificial negative correlations in seed-based connectivity analysis [203] have been reported. A potential limitation of the applied scrubbing approach to minimize confounding motion artifacts is the variation in length of the different remaining time series for each individual subject [314]. This is a fundamental problem for experimental designs with short acquisition times, however the reported amount of scrubbed data indicate a negligible amount for this work with its extended time period of acquisition of 25 minutes per fMRI session.

Pearson full correlation coefficient was chosen due to the simple and effective application in combination with a high number of ROIs and the systematic sliding-window approach, which led to extensive computational calculations. The Pearson correlation coefficient is a non-directed model-based metric to quantify interactions and makes the assumption of linearity with respect to the kinds of interactions that may take place between two signals. By combining this metric with the applied sliding-window approach, where two time series are shifted against each other, a cross-correlation function is obtained which accounts for the temporal structure in the data. However, the interpretation of the obtained connectivity correlations is complex as neuronal activations and communications can be considered bi-directional between two interconnected brain regions and can occur on various timescales [33]. Future investigations may include different metrics to quantify the relationship e.g. Granger causality or partial correlations to even further investigate the communication between several groups of brain areas to overcome the limitation of nonlinearity or directed interactions. Several different metrics have been investigated including ones to quantify causal relationships i.e. effective connectivity [297].

The sliding-window statistical approach with adjustable shifts between cortical processes and pain ratings allowed one to take into account the temporal dynamics of the continuous design. The variable shifts incorporate, on the one hand, individual variations of the HRF and, on the other hand, the individual cascade of cortical processes that precede and succeed the transient intensity of pain which is a major advantage compared to fixed time-series. Although no gold-standard recommendations are available on the sliding-window parameters, resting-state fMRI designs have found robust FC results for window-lengths of approximately 30 s, whereas task-based sliding-window parameters are inherently dependent on the experimental fMRI task-design [161]. Additionally, different unknown timescales, on which changes in functional connections may vary have to be taken into consideration [207]. Therefore, sliding window parameters were chosen to capture the variable frequencies of the pain ratings of all patients to resolve the timing of the different pain encoding processes as accurately as possible. The high-resolution offsets of 1 s between the wide range between -15 and 20 s allowed for a determination of a hemodynamic response curve for the majority of the ROIs BOLD response with a good resolution to detect an increase, peak activation and decrease of the signal. Future analysis could include a detailed investigation of regional-specific timescales of BOLD activations in individual brain regions as well as systematically changing window parameters such as windowlength or shape. Alternative solutions to include considerations of different timings, could be the generation of optimal basis sets for use in the HRF convolution (e.g. FLOBS in FSL) [311].

The proposed connectivity schemata identified statistical significant brain regions which repre-

sented the encoding of pain intensity as well as the change in pain intensity in a more intuitive way. Significant brain regions, identified by the statistical analysis, were thresholded at 80 % to mostly represent a positive or negative relationship with the pain ratings, i.e. positive correlations or anticorrelations. Brain regions which were e.g. significantly positively correlated to high pain ratings in the first half of the fMRI rating design but negatively in the second half were excluded from analysis (see Figure 9.11 B). On the one hand, this certainly limits the analysis to some extent but interpretability of the results are otherwise difficult and rather non-intuitive. On the other hand, this separation may not even be distinguishable in shorter acquisition approaches and was only possible due to the extended acquisition time. Nevertheless, interpretations of positive connectivity as well as negative connectivity, i.e. anticorrelations, are still highly debated [50, 232]. Importantly, no anticorrelations have been found in this analysis.

Connectivity pattern encoding pain perception in CBP

Overall, predominantly a negative relationship between cortical connectivity and high as well as rising pain was found in CBP. These findings are considered to reflect the severe impact of chronic pain on perception and cognitive functioning and are supportive of previous studies showing how the experience of pain suppresses, inhibits, and impairs cortical processes [53]. The findings on intra-occipital pain intensity related disruptions are in line with the observations of suppressed occipital activity through applied pain [224, 295] and the finding of disrupted visual network connectivity in chronic pain [267]. Similar to the obtained results, disrupted connectivity between the PCC and parietal regions was previously reported for acute tonic and chronic orofacial pain [5]. Furthermore, impaired parahippocampal and hippocampal functioning as observed in chronic back pain has been discussed in the context of depression [87, 195], biased memory [36, 220], pain memory [244], and the transition from episodic to chronic pain [178, 204].

Besides disrupted connectivity, a positive relationship for cerebellar and parietal connectivity with high levels of pain was found. The contribution of the cerebellum to the cortical processing of pain has been discussed in various contexts [69], including emotion, cognition, and motor functions, and has been suggested to integrate the multi-faceted aspects of pain experience[199]. Consequently, the suffering from long-lasting pain may have caused structural changes in the cerebellum. For CBP, alterations of the cerebellar grey matter density were observed compared to healthy subjects in [171, 287]. Both, cerebellum and the connected parietal regions have been associated with a top-down attentional direction of pain intensity features [168].

For the investigation of the change of pain intensity, periods of rising pain were contrasted with periods of falling pain in the statistical model. This contrast controls for motor-related connectivity and decision making processes, as these processes equally occur independent of rising and falling pain. As a result, a wide-spread disruption of cortical circuits with rising pain was observed; the connectivity was significantly higher during falling pain for a number of cortical connections. This applied to the connectivity between brain regions commonly associated with pain perception, i.e. insular cortex to pACC [285]. Similar results were reported previously, where increased cortical connectivity was observed for decreases in pain intensity for regions that are known to be involved in the encoding of pain [257].

In addition, a disruption within the parietal and the cingulate cortices was found. The parietal disruption may reflect the deviant processing within the default mode network, which has been previously reported [5, 30, 169].

Connectivity pattern encoding pain perception in CM
For CM, the group statistics showed only two connections that represent the encoding of pain intensity. Among these connections an increasing connectivity with higher pain intensities between the right anterior insular and the left orbitofrontal cortex was found. Orbitofrontal cortex [19, 306] and anterior insular cortex [295] have been consistently found to be involved in pain processing. The comparably low number of connections may represent the complexity of the cortical processing in chronic migraine [51, 79]. Indeed, most patients who were included in the present study exhibited individually unique patterns of pain-related cortical connectivity that do not match the overall pattern of the group statistics.

There are a number of connections that represent the rising and falling pain in CM. An involvement of the right anterior insula was found which is connected to orbitofrontal areas; one of these frontal regions has been previously related to migraine attacks [77] and placebo modulation [296]. The pain-modulated connectivity between the anterior and the posterior cingulate cortex can be considered to reflect the activity of the DMN [5, 30, 72]. Superior temporal regions were found to be positively connected to the insula and have been shown to be affected in episodic migraine [261] and pain memory [127]. This may also apply to the connection between the hippocampus and an inferior temporal area. Again, the majority of the regions exhibit a disrupted connectivity with rising pain.

However, the findings are not directly comparable to previous studies as the nonstationary aspects of the cortical network were assessed. Here, the pain-dependent within-subject dynamic fluctuations irrespective of the general amplitude of the BOLD oscillations was investigated. This perspective on the data considers and contrasts only the rising and falling periods.

Individual patterns of pain intensity encoding in single patients
A major aspect of the investigation is the assessment of a single patient's profile of pain processing. In order to describe the unique patterns of pain-related connectivity, each pain patient was repeatedly recorded in order to obtain sufficient and reliable data. Individual connectivity maps were created for each patient which varied significantly from the group results in the number of connections as well as in the overall connections. For these reasons no direct comparison of pain-related connectivity changes between CM and CBP patient groups was calculated, as variability between subjects in one chronic pain cohort is already tremendous.

Individual variations may reflect pain processing, the experience of pain or even the individual coping strategies of the patient, all of which may influence the success of chronic pain treatments. Only a few studies have addressed the importance of single patient effects in their analysis and have reported variability [109, 111, 179]. However, the possibility that variables such as pain duration and intensity, current medication, or indeed psychological parameters and subtypes of chronic pain diseases may modulate some aspects for specific individuals, can not be excluded.

Limitations and Conclusion

Methodological limitations of this approach include the use of a predefined atlas, in which function as well as structure of a different set of individuals were used to predefine the cortical regions. This classification might not adequately reflect the functional characteristics for each individual in this specific cohort and task-free fMRI design.
As dynamic functional connectivity is only an indirect measure, it's interpretation is complex and not necessarily straightforward. Depending on the pairwise correlation values, negative correlations or "anticorrelations" are theoretically possible, but are particularly difficult to interpret and are still highly debated in the field of neuroimaging [232]. In this work no "anticorrelations" were found in the connectivity results, therefore only the positive connections found were described according to the chosen connectivity schemata. Future investigations may include a more sophisticated connectivity metric, i.e. partial correlations or graph-based analysis including several nodes to characterize functional connections between single brain regions and their temporal dynamics among themselves [130, 207].

The experimental setup aimed to reflect the dynamically evolving cortical connectivities related to the subjective experience of pain. However, none of the single subject connectivity patterns, assessed in repeated sessions, resembled the patterns obtained by group statistics. The results suggest that individual chronic pain patients exhibit qualitatively distinct signatures of cortical connectivity; this applies to chronic back pain as well as to chronic migraine. Consequently, the present findings argue against a common biomarker for the subjective experience of chronic pain that is based on dynamic connections. This is in line with the experience of clinicians; each patient can be characterized by a unique personality, various combinations of symptoms, and a broad range of treatment success. The findings support recent developments for a more personalized medicine.

9.5 Stability of pain ratings in chronic back pain and chronic migraine patients

The following section describes the supervised ML approach pursued to investigate the hypotheses introduced in the objectives chapter 8.3. These include the investigation of the stability of the pain ratings across the four repeated fMRI sessions and the possibility of predicting the pain intensity levels based on learned brain activity from previous sessions. Sections 9.5.1 and 9.5.2 describe the extracted features from the underlying BOLD fMRI and pain rating measurements and the applied supervised ML regression models before the results are presented in section 9.5.3 and discussed in section 9.5.4.

9.5.1 Features

The measured BOLD signal intensity from all voxels belonging to each of the 408 parcellated brain regions (see section 9.4.1) were extracted and averaged. The obtained 408 BOLD signal time series ($t = 950$ time points) were standardized by subtracting the mean and dividing by the standard deviation of the time series (z-scores), and served as predictor variables/features. Hence, the data is represented as a matrix of dimensions 408×950 for each subject and session. Subjects with missing values or sessions were excluded. A total of 17/18 CBP/CM patients were analyzed. The endogenous pain level (amplitude - AMP) as indicated by the subject during the rating task is the target variable. Based on the distribution of shifting vectors (Appendix figure 11.1) obtained from the BOLD analysis, the rating vector at time $t = -6$ s was used for CBP and $t = -5$ s for CM.

9.5.2 Models and resampling

An eXtreme gradient boosting (XGB) algorithm (see section 7.1.2) was compared to a baseline linear regression model with LASSO regularization (see section 7.1.1) over the following two resampling schemes: cross-validation between-session and cross-validation within-session. These two resampling-schemes were chosen to investigate the stability of the pain ratings as follows: the between-session approach evaluated if the relationship between pain level ratings and BOLD activity learned in one fMRI session can be used to predict the brain activity in a different session. The within-session assessed if the relationship between pain level ratings and BOLD activity learned in one part of the fMRI session can be used to predict the brain activity in a different part of the session.

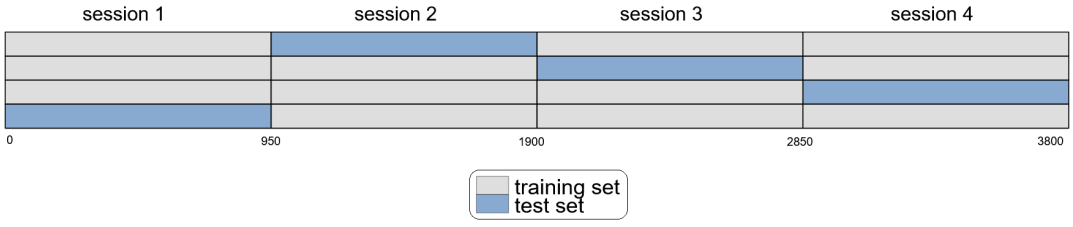

Figure 9.20: Cross-validation between-session: 4-fold cross-validation with three sessions in the training (grey) and one session in the test set (blue). One session consists of 950 datapoints. The cross-validation scheme is shown for the single-subject approach; for the group-level approach the corresponding folds for training and test sets were concatenated across all 17/18 CBP/CM subjects.

Both cross-validation schemes were separately applied to a single-subject and a group-based approach to compare subject- with group-level learning of the models, resulting in four different settings: Group-level between-session, group-level within-session, subject-level between-session and subject-level within-session. For the group-based approach the model is trained on all 17 subjects for CBP and all 18 subjects for CM, whereas in the single subject approach, the model is trained only on individual subject data. The resampling schemes for the single subject based approach for between- and within-sessions are shown in Figure 9.20 and 9.21, respectively. Group based resampling schemes were then obtained by concatenating the respective folds across all subjects.

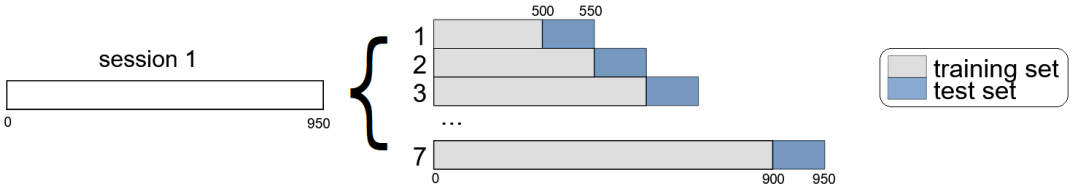

Figure 9.21: Cross-validation within-session: 7-fold rolling-window / walk forward cross-validation scheme in one measurement with an initial window size of 500 (training set) and a horizon of 50 datapoints (test set). The cross-validation scheme is shown exemplary for one session of the single-subject approach; for the group-level approach the corresponding folds for training and test sets were concatenated across all 17/18 CBP/CM subjects.

A so-called 'rolling window' or 'walk forward' cross-validation scheme with predefined folds (time slices, caret package [154]), which moves the training and test sets in time was applied as a resampling strategy for the within-session analysis approach. This accounts for the temporal order and non-independence of collected data points within a time series. The following parameters were chosen for the rolling window CV scheme: The initial window length, i.e. the number of consecutive values in each training subset was set to 500 (initial_window = 500) and the number of values in the test set at horizon = 50. The training set always starts at the first sample, varying its size over the data splits whereas the size of the test set remains fixed (fixedWindow = FALSE) which is skipped (skip = 49) for every window to ensure strict splitting of training and test set. Each single session containing 950 observations is thus divided into seven folds which are subsequently used for training and testing until all data are included. A 4-fold cross-validation scheme was applied between-sessions such that three of the sessions were used for training and one for testing.

An inner resampling loop was used for hyperparameter tuning for the XGB and LASSO model. For the between-session approach, hyperparameters were tuned over an inner 3-fold cross-validation resampling and over a 4-fold rolling-window cross-validation scheme for the within-session setting. The best found set of parameter configuration was then set as hyperparameters for the outer loop. The following four hyperparameters of the XGB were tuned over the following parameter space: maximum number of boosting iterations (nrounds, $50 - 500$), subsample ratio of columns when constructing each tree (colsample_bytree $= 0.05 - 0.1$), minimum sum of instance weight needed in a child node (min_child_weight $= 1 - 10$), minimum loss reduction required to make a further partition on a leaf node of the tree ($\gamma = 0 - 10$) [312]. For the LASSO model the regularization parameter $\lambda = \ln(0.01) - \ln(20)$ was tuned.

Evaluation of the models was based on the root mean squared error $RMSE_i$ as performance metric, with the subscript $i = \{l, x\}$ differentiating between the LASSO ($RMSE_l$) and XGB ($RMSE_x$) model. R_i^2 values are plotted in the corresponding figures.

All analyses were implemented in R (Version 4.0.2) using the mlr3 package [157]. The following additional software packages were used: mlr3learners [158], caret [154], ggplot2 [299], purrr [125], furrr [292], future [35], dplyr [300], mlr3viz [156], gridExtra [20] and zoo [318].

9.5.3 Machine learning results

Between-session setting

RMSE and R^2 values were calculated to measure the performance of the two regression models (LASSO and XGB) and a featureless model for comparisons. As the MSE measures the average squared difference between the estimated values of the model and the actual value, the RMSE indicate the root of the MSE and is an absolute performance measure in the units of the pain ratings.

The RMSE values for the models of the group results for the between-sessions analysis for CBP and for CM are given in Table 9.13. The corresponding R^2 values are given as follows and are shown in Figure 9.22 for all iterations for both CBP and CM. For the LASSO model the mean R^2 values are $R^2_l = 0.041 \pm 6.6 \times 10^{-3}$ for CBP and $R^2_l = -4.2 \times 10^{-5} \pm 8.3 \times 10^{-5}$ for CM. For the XGB model the mean R^2 values are $R^2_x = 0.048 \pm 4.5 \times 10^{-3}$ and $R^2_x = -2.8 \times 10^{-4} \pm 2.5 \times 10^{-4}$ for CBP and CM, respectively. The mean and standard deviations are given over the four resampling iterations. Both models show very low overall performance. In contrast to CM, the performance of both models for CBP is better than the featureless model. Both models perform better on the CBP dataset than on the CM one.

The subject-level between-session results are shown in Figure 9.23 and Figure 9.24 for CBP and CM, respectively. The mean RMSE over all subjects and resampling iterations are given in Table 9.13 below. The mean R^2 over all CBP subjects and resampling iterations is $R^2_l = -1.7 \times 10^{-4} \pm 0.015$ for the LASSO and $R^2_x = 0.015 \pm 0.026$ for the XGB model. The mean over all CM subjects and resampling iterations is $R^2_l = -2.3 \times 10^{-4} \pm 9.0 \times 10^{-4}$ for the LASSO and $R^2_x = -7.6 \times 10^{-3} \pm 0.013$ for the XGB model. All models therefore show low performance comparable to or worse than the featureless model which is predicting the mean value. Only the XGB model on the CBP dataset performs better than the featureless model.

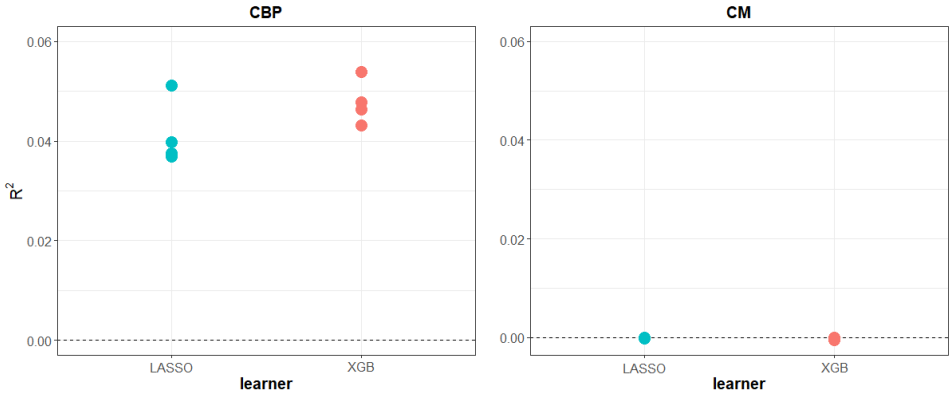

Figure 9.22: CBP and CM group-level between-session: R^2 values obtained from both the LASSO model and the XGB, are shown for CBP on the left and for CM on the right. The R^2 of the featureless model is indicated by the dashed line at 0.

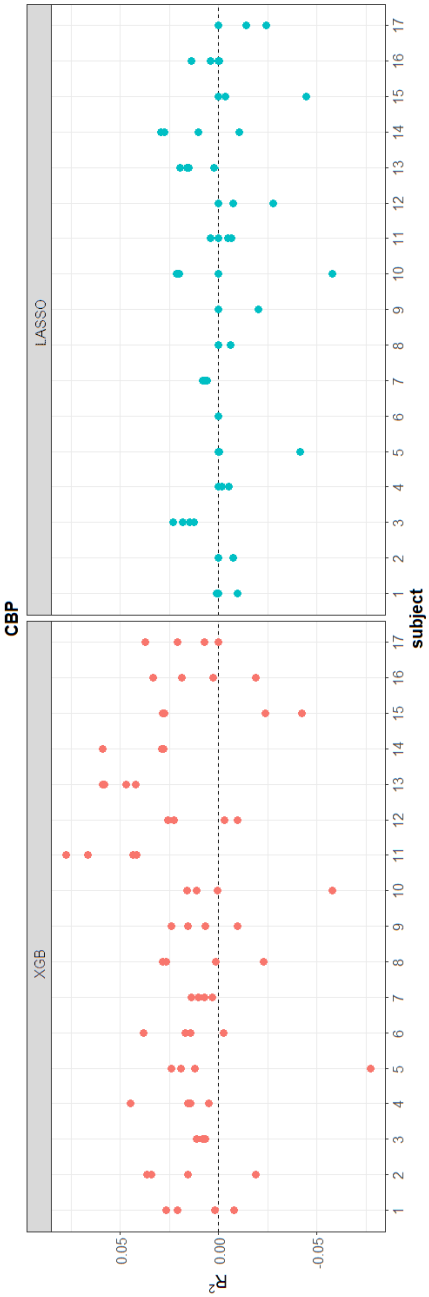

Figure 9.23: CBP subject-level between-session: R^2 values are plotted over the four resampling iterations for each subject.

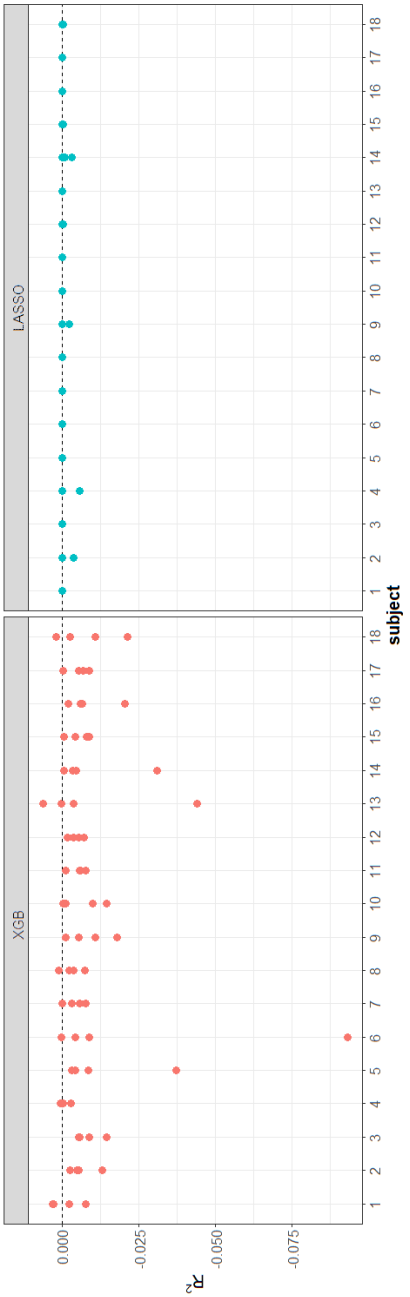

Figure 9.24: CM subject-level between-session: R^2 values are plotted over the four resampling iterations for each subject.

	RMSE		
	featureless	**LASSO**	**XGB**
CBP group	8.89 ± 0.15	8.71 ± 0.142	8.68 ± 0.153
CM group	8.12 ± 0.20	8.12 ± 0.203	8.12 ± 0.20
CBP subject	8.87 ± 0.67	8.87 ± 0.658	8.80 ± 0.658
CM subject	7.52 ± 3.08	7.52 ± 3.08	7.54 ± 3.08

Table 9.13: Mean and standard deviations of the RMSE values for the between-session setting for both group- and subject-level in CBP and CM for the featureless, LASSO and XGB model.

Within-session setting

The group-level within-session results are shown for each of the four sessions separately and models in the boxplots in Figure 9.25 for CBP and in Figure 9.26 for CM. The mean R^2 over all seven folds for CBP are given as follows for each of the four resamplings for both models (LASSO/XGB): $R_1^2 = 0.036 \pm 8.4 \times 10^{-3} / -5.9 \times 10^{-3} \pm 0.025$, $R_2^2 = 0.050 \pm 0.016 / -0.010 \pm 0.030$, $R_3^2 = 0.038 \pm 0.012 / 0.018 \pm 0.056$ and $R_4^2 = 0.063 \pm 0.014 / -5.1 \times 10^{-4} \pm 0.042$. The overall performance of both models on the CBP dataset is similar throughout the four sessions, with the LASSO model showing better results than the XGB model.

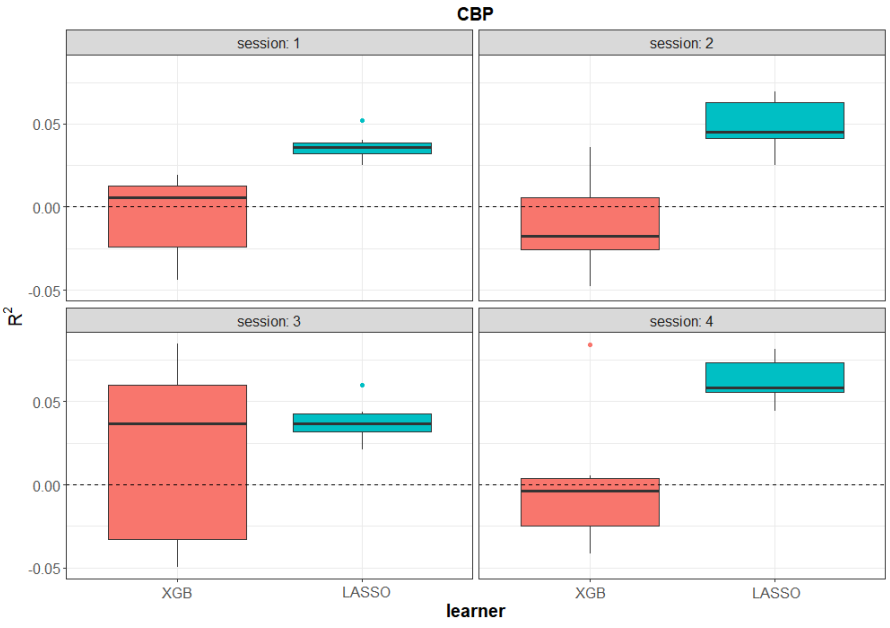

Figure 9.25: CBP group-level within-session: For each session the R^2 values of the LASSO / XGB model are shown over all seven folds.

The mean R^2 over all seven folds for CM are given as follows for each of the four resamplings for both models (LASSO/XGB): $R_1^2 = -9.2 \times 10{-}4 \pm 1.6 \times 10{-}3 / -0.13 \pm 0.056$, $R_2^2 = 4.3 \times 10{-}4 \pm 1.2 \times 10^{-3} / -0.14 \pm 0.035$, $R_3^2 = 2.6 \times 10^{-4} \pm 9.5 \times 10^{-4} / -0.11 \pm 0.029$ and $R_4^2 = 5.3 \times 10^{-4} \pm 1.4 \times 10^{-3} / -0.14 \pm 0.028$. In all four sessions for CM the XGB performs worse than the LASSO and featureless model. The LASSO model performs better than the

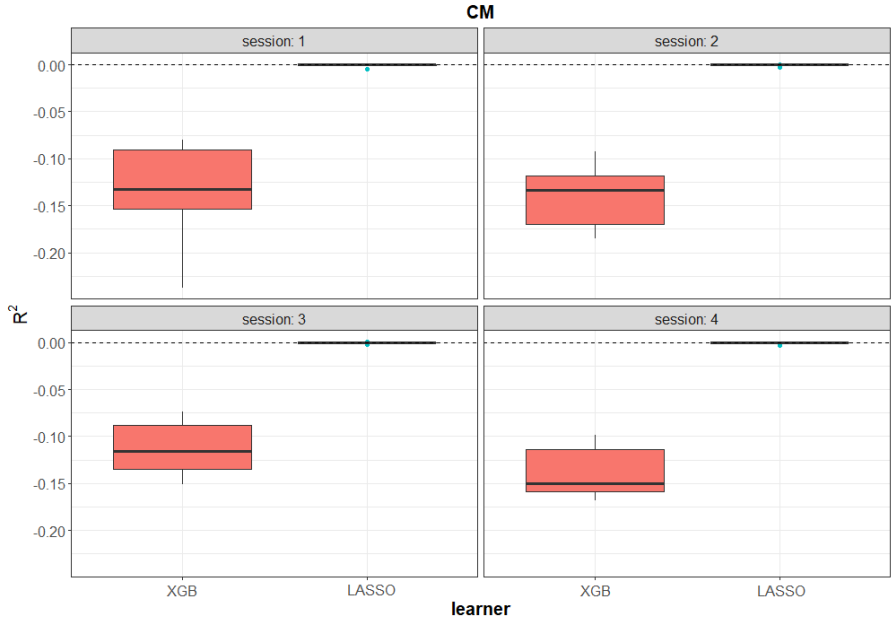

Figure 9.26: CM group-level within-session: For each session the R^2 values of the LASSO / XGB model are shown for all seven folds

featureless model on the CBP dataset, but equally to the featureless model on the CM dataset. The XGB model shows more variability than the LASSO model for all settings and models, but is better on the CBP dataset than on the CM dataset. The LASSO and XGB model mean RMSE values over all seven resampling iterations for each of the four sessions in CBP and CM are listed in Table 9.14.

	RMSE		
CBP group	**featureless**	**LASSO**	**XGB**
session 1	8.54 ± 0.20	8.38 ± 0.20	8.56 ± 0.20
session 2	9.04 ± 0.20	8.81 ± 0.22	9.08 ± 0.20
session 3	8.85 ± 0.21	8.69 ± 0.19	8.77 ± 0.29
session 4	8.92 ± 0.29	8.64 ± 0.28	8.92 ± 0.17
CM group			
session 1	8.05 ± 0.73	8.05 ± 0.70	8.57 ± 0.66
session 2	7.91 ± 0.73	7.92 ± 0.73	8.45 ± 0.72
session 3	8.56 ± 0.75	8.56 ± 0.75	9.02 ± 0.72
session 4	8.42 ± 0.74	8.42 ± 0.74	8.97 ± 0.77

Table 9.14: Mean and standard deviations of the RMSE values for the within-session setting for group-level.

The subject-level within-session results are shown in the boxplot of Figure 9.27 for CBP and in the boxplot of Figure 9.28 for CM. The mean RMSE values over all CBP subjects for each of the model is $RMSE_l = 8.19 \pm 1.20$ and $RMSE_x = 8.27 \pm 1.23$. The minimum is obtained in subject 1, session 3 with $RMSE_l = 4.94$. The mean RMSE values over all CM subjects for each of the model is $RMSE_l = 7.48 \pm 4.15$ and $RMSE_x = 8.25 \pm 4.28$ and the minimum is

obtained in subject 13, session 3 ($RMSE_l = 0.42$).

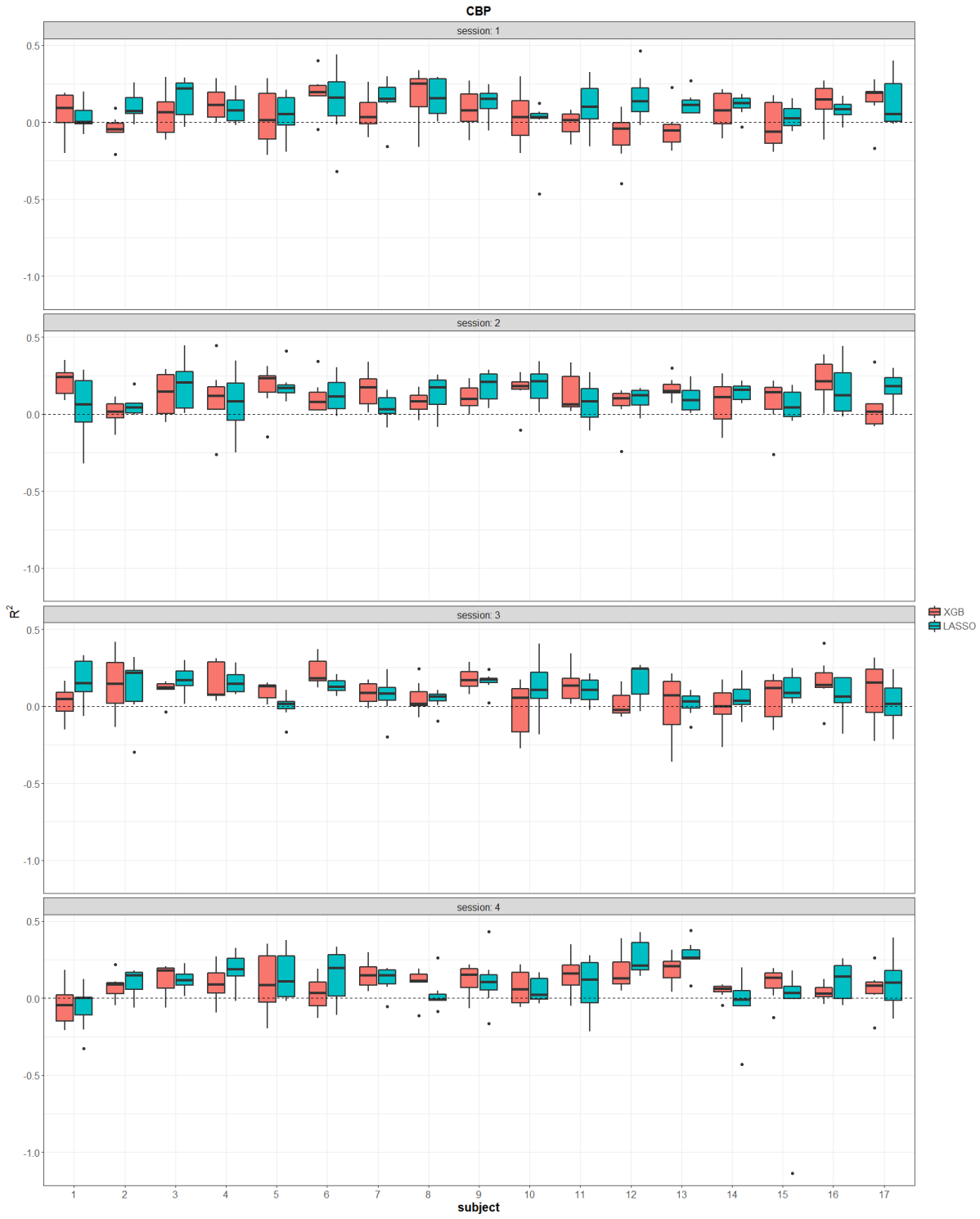

Figure 9.27: CBP subject-level within-session: For each subject, the LASSO and XGB model R^2 values are shown over seven folds for each session separately. The maximum is obtained in subject 12 session 1 with $R^2_l = 0.46$.

Figure 9.28: CM subject-level within-session: For each subject, the LASSO and XGB model R^2 values are shown over seven folds for each session separately. The maximum is obtained in subject 4 session 3 with $R^2_l = 0.39$. For visualization purpose only, three outliers are not shown in the boxplots: in session 3 subject 13 for LASSO/XGB R^2 = -6.0/-92 and in session 2 subject 7 for XGB R^2 = -11.

For CBP the mean R^2 values over the seven folds for each session separately are: $R_1^2 = 0.10 \pm 0.14/0.056 \pm 0.15$, $R_2^2 = 0.12 \pm 0.13/0.12 \pm 0.14$, $R_3^2 = 0.098 \pm 0.13/0.089 \pm 0.15$, $R_4^2 = 0.12 \pm 0.19/0.093 \pm 0.14$. Both models consistently perform better than the featureless model with the mean R^2 over all subjects and sessions for both models given by: $R_l^2 = 0.10 \pm 0.15$ and $R_x^2 = 0.089 \pm 0.14$. Session 2 showed the best performance for both the LASSO and the XGB model.

For CM the mean R^2 values over the seven folds for each session separately are given as follows: $R_l^2 = -0.047 \pm 0.13/-0.37 \pm 0.58$, $R_2^2 = -0.065 \pm 0.25/-0.53 \pm 1.1$, $R_3^2 = -0.11 \pm 0.66/-1.1 \pm 8.2$, $R_4^2 = -0.048 \pm 0.21/-0.39 \pm 0.49$. Therefore, similar results to the group-level within-session analysis were obtained in the subject-level within-session setting: whereas the LASSO model performs comparably to the featureless model throughout all sessions and subjects, the XGB model performs worse than the featureless model with additional higher variability over the seven folds. The mean R^2 over all subjects and sessions for both models is $R_l^2 = -0.067 \pm 0.37$ and $R_x^2 = -0.60 \pm 4.1$.

9.5.4 Discussion of machine learning results

The possibility of predicting the pain intensity based on fMRI BOLD brain activity alone was investigated and the stability of acquired pain ratings during four fMRI acquisitions was tested, i.e., if pain intensity levels can be predicted in a different session by a model trained on only one session. Diverse results were obtained depending on the four variants pursued. Overall, compared to the intercept model, the CBP data set yielded better results than the CM data set for both models across all four variants, but the overall performance was low. This leads to the conclusion that with the currently pursued approach, the pain intensity level in CBP and CM patients cannot be predicted solely on the BOLD signal of each region. All following observations and comparisons are therefore made on an overall low level of performance.

For the between-session variant on group-level, both models yielded better results on the CBP data set than the CM set. For both the CBP and CM cohort, the XGB model performed slightly better than the LASSO model. On subject-level, comparing both patient cohorts, the model fit on the CBP data set yielded better results than on the CM dataset. Comparing both models in each patient group separately, the XGBoost consistently performed better than the LASSO model on the majority of CBP subjects, in contrast to the CM data set, where the XGB model suffers from overfitting leading to negative R^2 values. The overall obtained maximum in both datasets is $R^2_x = 0.077$ in the chronic back pain cohort (subject 11, session4).

Looking at the performance values to answer hypotheses (9) and (10), the models performed better on group-level than on subject-level for CBP but better on subject-level than group-level in CM in the between-session setting. This is in line with previous observations of highly individual patterns of BOLD brain activity in chronic migraine patient cohort and a more homogeneous, although still variable, cortical activity in chronic back pain patient cohort in this dataset. Acquiring more data from different chronic back pain patients might therefore increase the prediction accuracy, whereas for chronic migraine more data for each individual subject may be more effective. The stability of the pain ratings and its underlying brain activity is therefore more given in CBP patients than in CM patients based on the obtained observations.

Within-session group-level analysis showed better results of the models compared to the intercept model on the CBP dataset, but negative R^2 values for almost all CM sessions and iterations. Overall, comparing both models, the LASSO model performed better than the XGB one, although both performances were very low. For CBP all four sessions yielded fairly similar results, with the third session showing the greatest variability in the XGB model.
On subject-level, the CBP cohort showed the best results, with a maximum of $R^2 = 0.46$ obtained in one iteration, indicating almost 50 % of the pain intensity can be explained by the corresponding brain activity in distributed regions. Here, the mean LASSO model slightly outperformed the XGBoost over all four sessions. For CM, the mean over all subjects and sessions showed a negative R^2 value, indicating both models perform worse than the intercept model. The XGB model constantly overfitted the data yielding negative R^2 values, whereas through the penalization in the LASSO model, the R^2 values were close to the featureless model at zero. High negative values for R^2 are generated by the high discrepancy between the predicted value and the true one given in equation 7.10.

Comparing now subject- with group-level, the models yielded better performances on subject-level than on group-level in CBP whereas in CM both settings yielded very low performance.

In general, the linear model fit showed improved performance over the XGB model for both group and single subject-level in CBP and CM. Overall, this suggests that stability over a shorter period of time of one session is given within individual CBP subjects, but not CM subjects. Further interpretations of the results with the obtained low performance does not seem justifiable.

Several limitations can be the reason for the obtained results, which can be divided into three categories, concerning the data set itself, the methodological approach and the underlying neurological processes involved.

First, the fMRI data set, although properly preprocessed according to recommended preprocessing pipelines, still contains residual noise, and changes due to BOLD activations are inherently low. On the other hand, preprocessing steps which smooth the data and spatially align the images to standard templates may remove distinct signals and hence may not guarantee fully accurate inter-subject functional consistency. Additionally, the data includes all three variables, pain intensity, the change of pain intensity and the encoding of motor activity. Encoding of motor activity yielded huge clusters of significant voxels in the BOLD analysis. This activity may confound the more subtle encoding of pain intensity encoding.
A feature space of 408 different features, corresponding to all parcellated individual brain regions, involves brain regions containing mostly noise or regions irrelevant to the task which introduces variance to the model [47]. Although both models, LASSO and XGB, inherently contain a feature selection property by imposing sparsity constraints [121], feature selection using prior knowledge of specific features (e.g. pain regions) could yield improved results, also in combination with dimensionality reduction techniques such as ICA or PCA. If, however, a mask with preselected, potentially informative features is used, it should be selected a priori on separate data, but this seems inappropriate at this point for a whole-brain multivariate approach.

Second, from a methodological point of view, the common problem of overfitting with sparse sample sizes in neuroimaging data was minimized by the applied regularization and resampling schemes with several cross-validation iterations to ensure good generalisability [245, 287]. Still, the relatively small sample size is one of the most limiting factors in neuroimaging machine learning approaches [18]. To improve the performance of the models, an increased number of iterations for the hyperparameter tuning could be used in the future. Further, modelling of subject specific effects on group-level could be included to allow for subject specific variations. Special focus was put on the walk forward cross-validation scheme to account for the resampling in time series analysis. However, the prediction could be additionally improved by exploiting the properties of the time series itself, i.e. by incorporating time series features into the model to account for e.g. periodicity of the pain ratings. The focus of this work though, was to purposely only include brain activity to predict the pain intensity. So far, no adjustment or inclusion of modelling of the autocorrelation present in the data was attempted. One way to include autocorrelation into the ML models would be to include lagged features of the pain level and/or time with a time series model, e.g. ARIMA [43]. With the implementation of the walk forward scheme in the presented exploratory analysis, future models can thus be easily compared against autoregressive models.

Third, the timing of the underlying neurological processes are still unknown. The HRF is slow and only an indirect measure of the cortical activity. Incorporating the timing results from the BOLD analysis, the pain rating vector with the shift corresponding to the maximum of the most regions was used. This certainly is a first approach to account for the variability between all 408 brain regions but may not reflect the actual timing of events in many regions. As can be seen from the BOLD and connectivity results, the encoding of especially the pain intensity is difficult to resolve, in particular for CM patients, and the SLP rather than the AMP variable leads to more meaningful results. Possibly these processes cannot be distinctly separated with the pursued ML approach and the value of pain intensity has no clear, separable neuronal representation, detached from the pain experience as a whole. The assumptions of a linear relationship between high-dimensional fMRI signal and pain ratings instead of a complex nonlinear one may also not be representable of the underlying cortical processes [59].

The majority of neuroimaging studies in the past have used classification-based approaches, as prediction compared to classification is harder but would be more promising for clinical utility, e.g. for disease prognosis and treatment progress [18]. An increasing number of studies nowadays focus on prediction of continuous variables such as individual cognitive scores or behavioral performance using fMRI data [18]. The intersubject variability between fMRI sessions is a general problem of functional magnetic resonance imaging and a ML-based biomarker would have to take subject-specific effects into account as well as fulfill several other properties, such as practical issues like independence of acquisition site and scanner type [238]. Further investigation into the possible applications of ML algorithms to fMRI and pain neuroimaging are necessary to harvest the objectivity a ML approach can offer on the pain experience and pathology [2, 142, 235]. Future approaches, involving multi-voxel pattern [238] analysis and deep learning strategies, e.g., neuronal networks, may be more capable of data-driven automatic feature learning, removing the subjectivity in selecting relevant features and disentangling the underlying complicated data patterns. Such models in combination with even larger data sets as acquired in this work are needed to potentially provide useful and robust brain measures and new disorder categories that will help treatments of the patients [47].

10 Conclusions and future directions

In conclusion, the presented work describes investigations to understand the neuronal underpinnings of the natural fluctuations of spontaneous pain based on data acquired in repeated acquisitions of fMRI of two chronic pain disease cohorts: chronic back pain and chronic migraine. During four repeated fMRI sessions of 25 minutes, 20 CBP and 20 CM patients indicated their continuous, endogenous fluctuating pain intensity without application of external stimuli. The analysis of continuous pain assessment, which best captures the natural, spontaneous and unique fluctuations of chronic pain patients is hardly pursued in a field that relies mostly on the application of exogenous pain to chronic pain patients. Only one group has investigated continuous pain rating paradigms for fMRI [16, 28, 120] and one study applied it to EEG measurements [185]. To the best of the author's knowledge, this is the first investigation of a sliding-window whole-brain BOLD and dynamic functional connectivity approach with a continuous, stimuli-free pain rating fMRI paradigm both in CBP and CM patient cohorts. Therefore the presented study here contains the most thorough analysis of the natural pain experience in two chronic pain cohorts, adding new aspects to the understanding of the core of chronic pain disease, especially in chronic migraine where data is scarce. Three different analysis approaches were pursued to investigate the naturally evolving trajectory of pain: an fMRI BOLD activity approach, a dynamic functional connectivity approach to assess functional coupling between brain regions, and a ML approach to test for stability over several fMRI sessions as well as prediction of pain intensity levels based on BOLD activations.

Methodological considerations

The presented concept of a continuous fMRI design in combination with the sliding-window and LME analysis helps the identification of the true underlying chronic pain disease and must be further investigated especially in patient populations where additional stimuli seem unwarranted. This approach emphasizes the importance of adjusting the fMRI experimental paradigms to the true underlying, investigated neuronal processes. In contrast to block-design studies where the experimental task is set in advance, special attention must be given to the performance of the continuous performance of subjects, and repeated or extended fMRI acquisitions are needed for robust results.

The applied sliding-window approach, both in the BOLD and FC analysis, allowed accounting for unknown timings of different cortical processes, variability in the HRF for each individual ROI and variability in two pathological populations. Such combined use of methodologies has not been reported in the literature and showed a simple but effective technique to resolve the dynamics of the functional connections. However, certain weaknesses still need to be assessed in future systematic analysis, such as the fact that results depend on the chosen sliding-window parameters, especially the window-length.

Additionally, as dFC gained more popularity in recent years because functional connections are not being seen as constant over the acquisition of a resting-state acquisition anymore, the interest grows in a more complex, biologically motivated dFC metric. The presented approach identified the cortical processes involved with a connectivity scheme to better capture and visualize the complex dynamics, but interpretation with a simple descriptive measure is lim-

ited. Overall, new suggestions and directions for future continuous, naturalistic approaches are presented in this work adding to the neuroimaging community, which lacks standardized preprocessing, analysis and statistical approaches in particular for continuous and spontaneous fluctuating fMRI designs.

Processing of pain in chronic pain patients
The results of this study further underlines the importance of the insula cortex, as a major contributor for the experience of pain in chronic pain patients. BOLD activations indicate a significant involvement of the insula in both processes of pain intensity encoding as well as the change of pain intensity encoding. The involvement of the pACC as main hub of the descending pain control system further indicates a disruption of the inhibitory control system of chronic pain patients. For both the BOLD activity as well as the connectivity analysis, significant results were obtained in the cerebellum indicating an altered relationship of sensory-motor and emotional processing in the presence of chronic pain. Alterations in the thalamus and brain stem (pons) further suggest impaired brain circuits and modulation of nociceptive information. Overall, a reduced cortical connectivity for higher pain states and increased connectivity for low pain states were identified and speak for a general disruption of brain communication supporting the idea that chronic pain patients, suffering from pain over a long period of time, undergo changes in many brain regions of cortical pain processing.

Subject Variability
One of the challenges in chronic pain imaging is the variability within and between patients, as well as the fact that chronic pain has not yet been linked to alterations in single brain regions or networks alone. Through unique combinations of several sensory, cognitive, emotional and motivational processes, each person experiences pain differently, leading to a tremendous individual variability [74]. BOLD activations, as well as functional connectivity patterns vary in both, CBP and CM, patient groups, stating the importance of an assessment of an individual pain signature. This work adds to the functional coupling of brain regions altered in the brain of chronic back pain and chronic migraine patients to enhance and promote individually tailored treatments in medicine [202]. Individual results have so far only been included in a minority of fMRI studies, which all have reported considerable variability [109, 111, 179]. Further investigations are needed to explore whether the current findings on individual pain signatures can be utilized for interventions that aim to directly modulate brain activity, e.g. with a neurofeedback approach [61, 183]. Increased data sets such as collected in this study and larger cohorts can be expected to support the concept that inter-individual variance within patient cohorts needs to be disentangled to better model the diseases, with various patients at different stages of disease progression showing different activation and involvement of brain areas. However, collection of larger cohort sizes is difficult for fMRI data, as different technical equipment and protocols complicate the merging of smaller datasets collected at various scanning sites.

Bigger datasets need to be acquired to increase reproducibility and include ML approaches for objective measures
Even larger amounts of fMRI data than acquired in this study (with four recordings for each patient amounting to a total of more than 100 minutes of pain processing) are needed to identify the true underlying patterns and distinguish them from random fluctuations of neuronal or non-neuronal signals with ML approaches. Although the applied ML algorithms in this work were

not able to accurately predict pain intensity solely based on BOLD activations, first ML studies were mostly able to differentiate between healthy and chronic pain patients [287], as well as between painful and non-painful stimuli [295]. The work presented here lays a methodological groundwork for similar continuous designs [76] to potentially achieve a model-free evaluation of pain intensity levels based on brain activity, but different approaches such as multi-voxel pattern analysis (MVPA)-based on the identification of spatial activity patterns might be better suited for future studies [212]. Without the need to self-report pain intensities an objective measure could be introduced into clinical practice to aid diagnosis and treatment. However, for an involvement of multivoxel pattern analysis or machine/deep learning approaches in a clinical setting, limitations such as the missing knowledge about the exact relationship between fMRI signals, physiological changes modulating the BOLD effect and neuronal activity need to be overcome [50]. Additionally, with such approaches, even larger cohort sizes are needed to provide a robust estimate of the generalisability of the models. The presented work of the ML approach will continue in this direction by additionally analysing EEG recorded data and investigating different ML approaches to increase the prediction accuracy.

Pain areas were identified for future neurofeedback
fMRI methods allow researchers to noninvasively probe the brain during a variety of different tasks and states during the scan, including the brain in pain. In the last few years studies have been emerging which also directly include fMRI for treatment approaches such as real-time fMRI-based neurofeedback [183]. Here, patients are trained with a so-called neurofeedback approach to up- or down-regulate the BOLD response to directly influence the activation of a target brain area. These approaches have shown potential in treating chronic pain patients [61]. Although great variability was found, the presented work here lays early groundwork for such approaches, identifying brain regions corresponding to high/low and increasing/decreasing pain intensities during the spontaneous pain experience, which then can be further targeted in a treatment approach to reduce pain intensity. So far, only pain intensity encoding restricted to periods of increasing pain were investigated in previous studies [25, 185]. Additionally, the interpretation of positive and negative correlations, or 'anticorrelations', in the connectivity analysis must be addressed and clarified in future research, before stable and reliable treatment approaches can be investigated to target specific brain areas or connections. Based on the intra- and inter-individual findings of pain encoding in this study, only an individually tailored neurofeedback approach seems reasonable and future studies must address foremost the stability and reproducibility of pain encoding patterns. The ultimate goal should be a combination of real-time neurofeedback and ML approaches to allow for the identification and targeting of individual pain facilitating processes [183]. Additionally, further research is needed to resolve the involved dynamics of rising and falling pain as well as the overlap between two adjacent events and their influence on each other [211, 241]. Future studies may overcome the lack of temporal resolution of fMRI with combined EEG and MRI techniques to harvest the best of both imaging modalities [207]. As a first step to include multimodal imaging data for a more complete analysis, complementary to this fMRI approach, EEG measurements were taken with the same methodological approach and patient cohorts after or before the fMRI sessions and are currently analysed.

All in all, the comparison with literature as discussed demonstrates that there is still an urgent need for a better understanding of chronic pain diseases - from the transition from acute to the chronic condition, as well as its manifestations and their consequences in the individual

brain. Without the right diagnosis and treatment, the majority of the population diagnosed with a chronic pain disease will endure prolonged suffering with severe financial, social and economic implications. As this work tried to emphasize, individualized medicine, as well as individualized research, appears to be the most promising future direction. Group statistics reported in most manuscripts will only represent the minority or even single individuals.

Overall, the data presented in this thesis added new aspects of chronic pain diseases to the neuroscience research field by demonstrating how brain regions in chronic back pain and chronic migraine patients activate and communicate with respect to different pain intensity levels and rising and falling pain. The powerful combination of a continuous fMRI design, whole-brain analysis plus sliding-window approach in combination with improved machine learning approaches will aid the ongoing research efforts to better understand chronic pain to improve patient healthcare.

11 Appendix

11.1 Sliding-window shift distributions

This section shows the distribution of sliding-window shift vectors for both BOLD (A) and connectivity (B) analysis in sections 9.3 and 9.4, respectively.

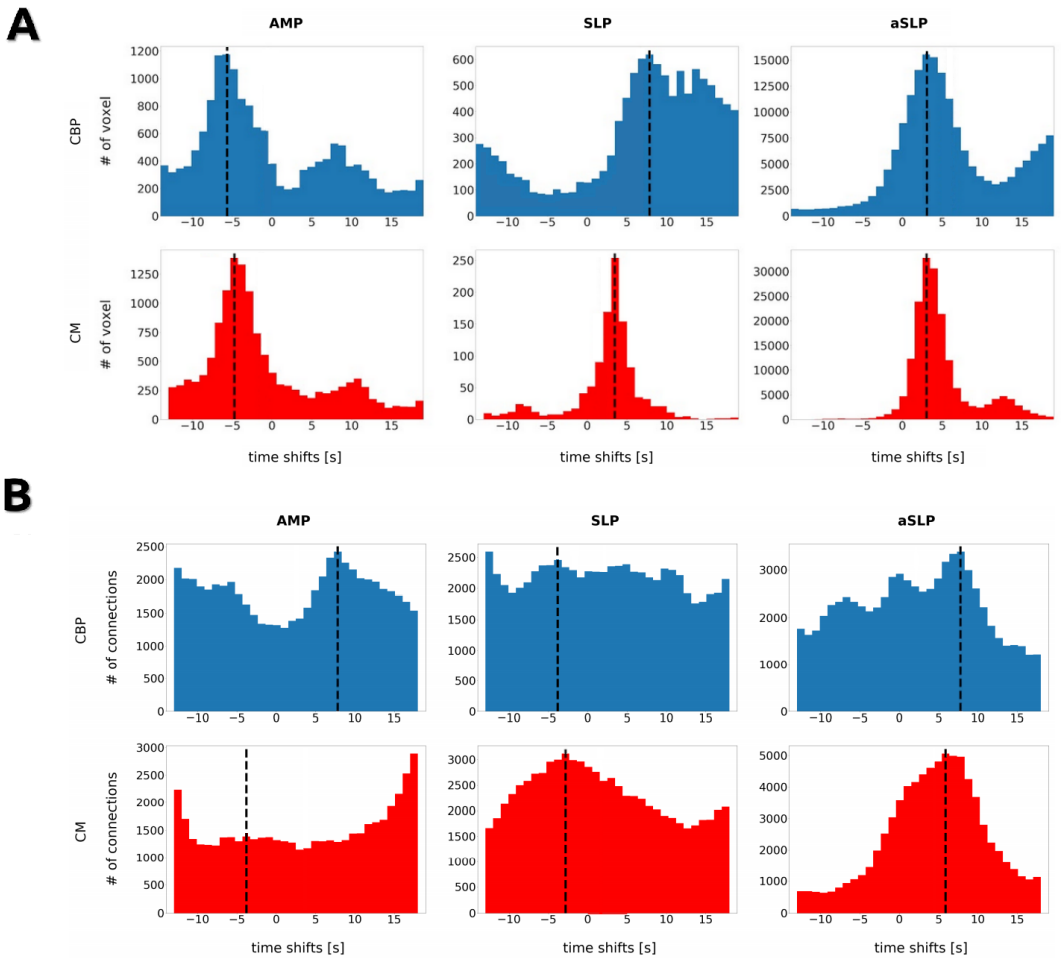

Figure 11.1: Distribution of sliding-window shift vectors for the CBP (blue) and CM (red) group results for AMP, SLP and aSLP; please note the different number of significant voxels for each variable AMP, SLP and aSLP. The maximum between -10 and 15 s is given as a vertical dashed line for each condition. A: BOLD analysis: The maximum for CBP/CM is at -6.3 s/-4.8 s, 7.7 s/3.5 s and 2.7 s/3.0 s for AMP, SLP and aSLP, respectively. B: connectivity analysis: The maximum for CBP/CM is at 7.8 s/-3.8 s, 3.8 s/-2.7 s and 7.9 s/6.0 s for AMP, SLP and aSLP, respectively.

11.2 BOLD analysis additional results

This section contains the detailed BOLD analysis results with Tables 11.1 - 11.6 showing the exact significant anatomical structures (displayed in sections 9.3.2 and 9.3.3), the pain ratings in Figure 11.2 and 11.3 for CBP patients and CM patients, respectively, as well as the patients characteristics and questionnaires in Tables 11.7 - 11.9.

anatomical structure	cluster size	t-value	MNI		
			x	y	z
posterior cingulate cortex, precuneus cortex	3712	-5.5	-1	-54	26
anterior insular cortex, frontal operculum cortex	1862	5.78	-36	15	4
occipital pole	906	-4.22	-2	-86	5
anterior cingulate cortex, paracingulate gyrus	877	-5.23	0	43	-3
lateral occipital cortex	434	-4.34	52	-61	27
pons	403	4.23	-4	-21	-35
frontal orbital cortex, frontal operculum cortex	327	4.23	38	25	0
lateral occipital cortex	318	-4.02	-41	-64	30
hippocampus, parahippocampal gyrus	225	-4.59	27	-27	-15
cerebellum (right VIIb)	170	3.95	31	-62	-49
superior frontal gyrus, middle frontal gyrus	117	-3.51	-27	19	58
inferior frontal gyrus, precentral gyrus (M1)	115	3.97	55	10	4
frontal pole	86	-3.58	-15	42	50
middle temporal gyrus	69	-4.41	-60	-14	-11
cerebellum (left IX)	51	-3.76	-9	-50	-41
occipital fusiform gyrus, lingual gyrus	51	-3.75	24	-70	-6
frontal pole	46	-3.93	-41	57	2
subcallosal cortex	44	-4.02	0	6	-6
superior frontal gyrus	43	-3.34	24	31	50
cerebellum (right IX)	41	-3.01	6	-54	-35
right pallidum	39	3.62	16	-3	7
amygdala	33	-3.71	-11	-10	-14
superior frontal gyrus, middle frontal gyrus	28	-3.51	-23	1	52
frontal pole	24	-3.44	38	61	-5
middle frontal gyrus	23	-3.4	-40	2	49
frontal orbital cortex	18	3.62	-41	25	-21
posterior cingulate cortex	17	-3.57	9	-38	11
parahippocampal gyrus	16	3.22	-23	-32	-28
middle frontal gyrus	13	-3.51	-51	25	25
anterior cingulate cortex	11	3.62	0	20	18
superior frontal gyrus	11	-3	-7	17	67
superior temporal gyrus	11	-2.9	53	-9	-12

Table 11.1: Active brain areas that encode the pain intensity (AMP) across all CBP patients for the BOLD analysis in section 9.3. The size of the active cluster of voxels, the significant t-value and the MNI coordinates of the center of the cluster are given for each anatomical structure.

anatomical structure	cluster size	t-value	MNI		
			x	y	z
frontal operculum cortex, anterior insular cortex	1738	7.74	-38	27	8
precuneus cortex, posterior cingulate cortex	1511	-6.86	4	-56	25
paracingulate gyrus, anterior cingulate cortex	878	-6.43	0	44	-3
frontal operculum cortex, anterior insular cortex	259	5.74	35	28	2
lateral occipital cortex	236	-5.78	49	-59	29
occipital pole	232	-5.93	15	-94	14
occipital pole	176	-5.84	-5	-90	18
parahippocampal gyrus	173	-5.45	-24	-40	-10
brain stem	163	-5.57	4	-26	-41
lateral occipital cortex	144	-6.32	-45	-72	6
parahippocampal gyrus	134	5.35	-30	-42	3
anterior cingulate cortex	132	5.22	0	21	26
subcallosal cortex	103	-6.16	0	8	-4
hippocampus	96	-5.01	29	-23	-17
occipital pole	92	-5.03	-20	-98	0
left caudate	90	4.96	-7	4	7
frontal pole	85	-5.69	23	40	44
posterior cingulate cortex	83	4.64	-1	-26	22
cerebellum (left IX)	82	-6.01	-8	-51	-47
middle frontal gyrus	75	4.95	-36	34	35
subcallosal cortex, anterior cingulate cortex	63	6.28	1	27	1
occipital fusiform gyrus	61	4.96	28	-79	-20
frontal pole	61	4.96	38	61	-7
posterior cingulate cortex	43	4.87	-11	-39	16
lingual gyrus	36	-5.02	-11	-70	-6
precuneus cortex	33	4.84	-10	-72	48
lingual gyrus, occipital pole	31	-4.63	-8	-90	-6
occipital pole	28	-5.21	-28	-93	11
middle temporal gyrus	26	-4.62	-60	-21	-7
brain stem	26	4.45	-8	-20	-41
cerebellum (left IX)	24	4.73	-10	-50	-38
angular gyrus, superior parietal lobule	24	4.57	-38	-52	42
paracingulate gyrus	21	3.55	17	36	-5
supramarginal gyrus	18	4	-54	-42	31
superior frontal gyrus	17	-4.17	24	23	61
occipital pole	16	4.06	17	-94	-7
precuneus cortex	16	-3.79	-18	-51	6
temporal fusiform gyrus	14	3.95	-37	-35	-9
anterior cingulate cortex	13	3.91	-13	34	-5
cerebellum (right VIIb)	13	3.74	25	-73	-49
brain stem	13	3.58	-15	-23	-13
thalamus	13	3.46	18	-6	7
temporal pole, middle temporal gyrus	13	-3.45	-48	2	-31
brain stem	12	4.43	-11	-9	-35
parietal operculum cortex	12	-3.67	-50	-25	15
angular gyrus	11	3.81	-32	-58	23
hippocampus	11	3.42	36	-33	-5

Table 11.2: Active brain areas that encode the change of pain intensity (SLP) across all CBP patients for the BOLD analysis in section 9.3. The size of the active cluster of voxels, the significant t-value and the MNI coordinates of the center of the cluster are given for each anatomical structure.

anatomical structure	cluster size	t-value	MNI		
			x	y	z
supramarginal gyrus		21	-45	-37	43
superior parietal lobule		19.7	-43	-41	48
thalamus, insular cortex	21942	19.4	-10	-18	8
precentral gyrus (M1)		18.8	51	8	23
postcentral gyrus (S1)		18.2	-56	-18	23
occipital pole,		19.7	30	-69	-19
cerebellum (right VI)	4830	18.7	30	-63	-21
superior parietal lobule	4127	19	44	-43	44
occipital pole		20.1	-34	-73	-14
cerebellum (left VI)	3845	17.5	-30	-70	-23
middle frontal gyrus	981	16.2	38	39	27
middle frontal gyrus	772	14.5	-34	39	27
posterior cingulate cortex	512	15.4	-3	-26	32
cerebellum (left VIIb)	432	14.2	-27	-64	-48
parahippocampal gyrus	426	-15.4	-27	-33	-13
hippocampus	370	-13.5	29	-25	-15
precuneus	369	-14.6	-8	-59	20
superior temporal gyrus	285	-14.3	-56	-12	-8
lateral occipital cortex	238	-13.3	-45	-71	33
precuneus	90	-12.2	8	-57	22
posterior cingulate cortex	78	13.2	13	-31	43
superior temporal gyrus	69	-12.6	59	-8	-8
lateral occipital cortex	68	-13.7	52	-67	31
cerebellum (vermis IX)	67	13.7	1	-57	-33
thalamus	62	12.9	24	-26	0
paracingulate gyrus	46	-11.6	-4	48	0
cerebellum (left X)	28	12.3	-21	-38	-41
cerebellum (left crus II)	14	11.8	-7	-75	-39

Table 11.3: Active brain areas that encode processing of motor activity, decision making, and visual change (aSLP) across all CBP patients for the BOLD analysis in section 9.3. The size of the active cluster of voxels, the significant t-value and the MNI coordinates of the center of the cluster are given for each anatomical structure.

anatomical structure	cluster size	t-value	MNI		
			x	y	z
posterior cingulate cortex, precuneus cortex	4995	-4.76	-4	-52	21
anterior cingulate cortex	920	-4.03	-3	34	4
amygdala	674	-3.99	-26	-5	-21
amygdala, hippocampus	375	-3.7	21	-17	-12
superior frontal gyrus	322	-3.19	25	-2	59
subcallosal cortex	306	-3.8	-1	13	-7
cerebellum (right VIIIa)	302	3.52	20	-65	-51
occipital pole	279	-3.5	14	-94	17
frontal pole	254	-3.79	-15	62	16
frontal pole	226	-4.59	22	60	20
frontal orbital cortex	175	3.77	47	20	-8
thalamus	174	-4.2	13	-28	6
temporal fusiform cortex	174	4.05	43	-51	-18
middle temporal gyrus	171	3.42	53	-41	5
cerebellum (right crus I)	103	3.37	49	-63	-42
frontal pole	102	-3.51	34	59	3
lateral occipital cortex	102	-3.34	42	-76	27
cerebellum (left IX)	95	3.31	-8	-57	-51
postcentral gyrus (S1), superior parietal lobule	62	-3.16	25	-40	73
middle temporal gyrus	56	3.44	67	-43	-4
precentral gyrus (M1)	49	-3.03	30	-21	69
middle temporal gyrus	47	-3.44	-58	-55	1
occipital pole	43	-3.5	-3	-98	17
supramarginal gyrus	43	-3.3	36	-49	8
precentral gyrus (M1)	41	3.4	61	6	7
cerebellum (left VIIIa, VIIIb)	40	3.39	-27	-66	-55
middle temporal gyrus	30	3.45	65	-20	-8
parahippocampal gyrus	30	3.3	22	-5	-37
temporal fusiform cortex	27	3.07	-28	-11	-39
temporal fusiform cortex	25	-3.19	-38	-49	-2
lateral occipital cortex	21	-3.08	22	-71	57
intracalcarine cortex	19	-3.03	-6	-83	11
lateral occipital cortex	18	-3.21	52	-65	20
precuneus cortex	18	-2.98	-27	-54	11
precentral gyrus (M1), posterior cingulate cortex	16	-2.94	-4	-30	48
posterior insular cortex	14	-3.12	37	-8	5
middle temporal gyrus	12	3.15	58	-19	-17
occipital pole	11	-2.99	29	-93	13
left caudate	11	-2.96	-16	-15	28

Table 11.4: Active brain areas that encode the pain intensity (AMP) across all CM patients for the BOLD analysis in section 9.3. The size of the active cluster of voxels, the significant t-value and the MNI coordinates of the center of the cluster are given for each anatomical structure.

anatomical structure	cluster size	t-value	MNI		
			x	y	z
lateral occipital cortex	187	-5.77	39	-77	32
occipital pole	148	-5.89	-17	-97	-11
lateral occipital cortex	116	-5.63	12	-80	48
precuneus cortex	79	-6.09	17	-62	24
superior frontal gyrus	71	-5.57	24	4	58
cerebellum (right crus I)	38	5.19	39	-70	-30
angular gyrus, middle temporal gyrus	28	-5.44	55	-55	14
frontal orbital cortex, anterior insular cortex	25	5.28	-37	24	-2
cerebellum (right crus I)	19	4.95	34	-78	-34

Table 11.5: Active brain areas that encode the change of pain intensity (SLP) across all CM patients for the BOLD analysis in section 9.3. The size of the active cluster of voxels, the significant t-value and the MNI coordinates of the center of the cluster are given for each anatomical structure.

anatomical structure	cluster size	t-value	MNI		
			x	y	z
anterior insular cortex		19.7	40	12	2
thalamus	15531	19.3	9	-12	2
pallidum		18.0	-16	-4	1
cerebellum (left crus II, VIIb)	4729	17.2	-12	-63	-31
superior parietal lobule	2455	15.6	47	-39	44
precuneus	1173	-17.7	-4	-56	24
frontal pole	1167	17.1	36	43	24
hippocampus	793	-17.9	-26	-26	-15
paracingulate gyrus	614	-15.1	-2	55	4
cerebellum (right VIIIa, VIIIb)	535	14.7	27	-58	-50
lateral occipital cortex	493	-16.8	-42	-73	34
superior parietal lobule	479	14.7	-36	-44	46
occipital pole	475	15.4	29	-94	-5
hippocampus	461	-16.1	27	-20	-15
posterior cingulate cortex	345	15.3	2	-27	27
middle temporal gyrus	306	13.3	58	-50	4
precentral gyrus (M1)	282	12.9	-33	-9	55
superior frontal gyrus	180	-13.7	-18	34	48
subcallosal cortex	139	-14.7	0	12	-7
occipital pole	125	14	-23	-99	-9
lateral occipital cortex	119	-13.9	49	-64	31
superior temporal gyrus	117	-13.8	-58	-7	-11
precuneus	109	13.8	13	-74	41
precentral gyrus (M1)	95	12.9	-48	1	39
frontal pole	63	12.1	-28	46	21
superior temporal gyrus	57	-13	61	-2	-13
parietal operculum cortex	52	11.9	-51	-24	18
cerebellum (left X)	39	12.6	-23	-41	-40
posterior cingulate cortex	34	11.8	12	-27	40
cerebellum (right crus I,II)	22	-12.1	30	-80	-36
cerebellum (right IX)	19	-13.2	5	-50	-46
supramarginal gyrus	19	11.5	-58	-40	32
precuneus	12	11.5	8	-71	57
intracalcarine cortex	11	11.7	8	-76	13
cerebellum (vermis VIIIa,VIIIb,IX)	11	12.1	0	-58	-35
superior temporal gyrus	10	-12	-48	-35	2
lateral occipital cortex	10	11.7	47	-68	15

Table 11.6: Active brain areas that encode processing of motor activity, decision making, and visual change (aSLP) across all CM patients for the BOLD analysis in section 9.3. The size of the active cluster of voxels, the significant t-value and the MNI coordinates of the center of the cluster are given for each anatomical structure.

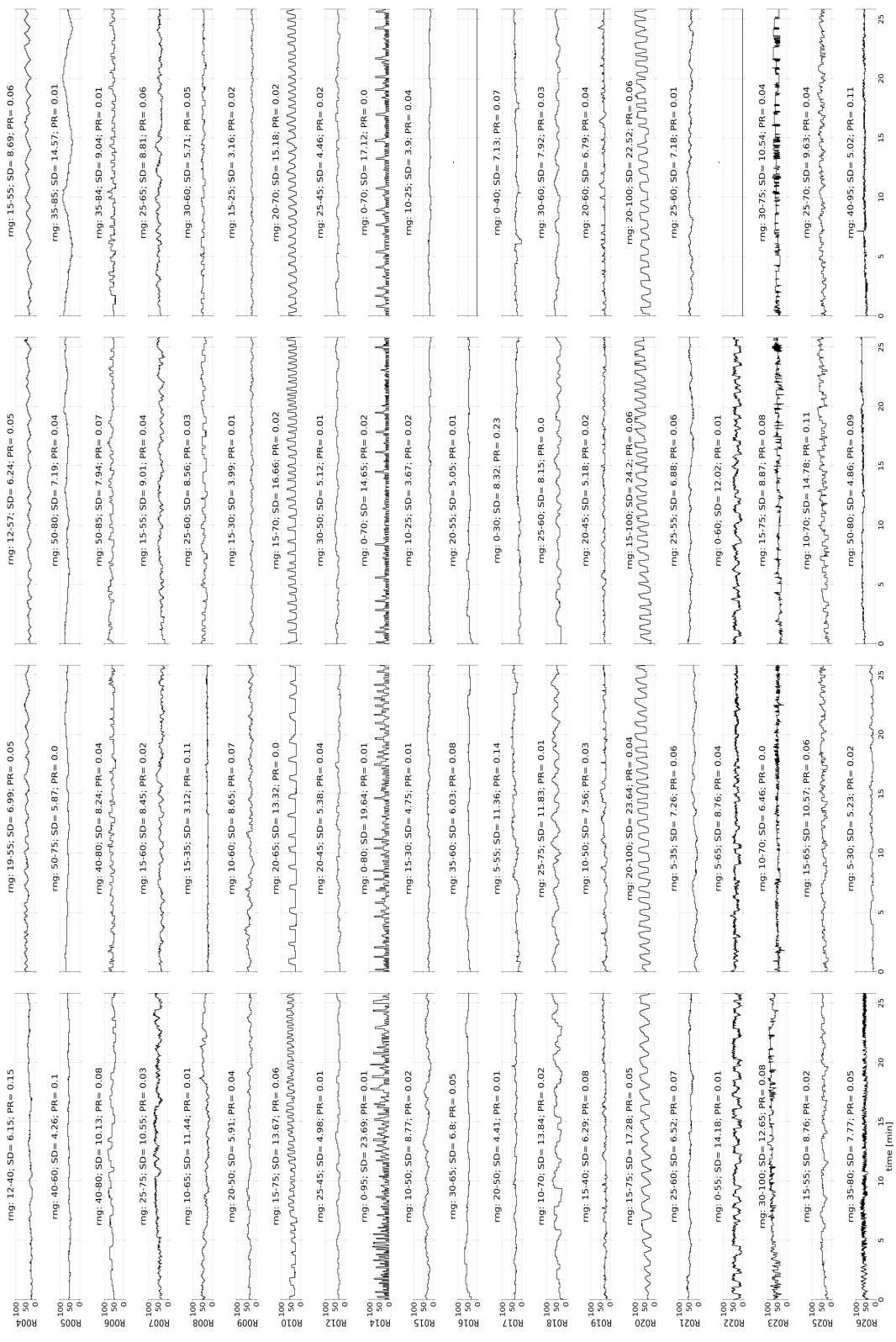

Figure 11.2: CBP pain ratings for all 20 patients and four sessions: the range (rng), the standard deviation (SD) and the parameter (PR) are given for each time course.

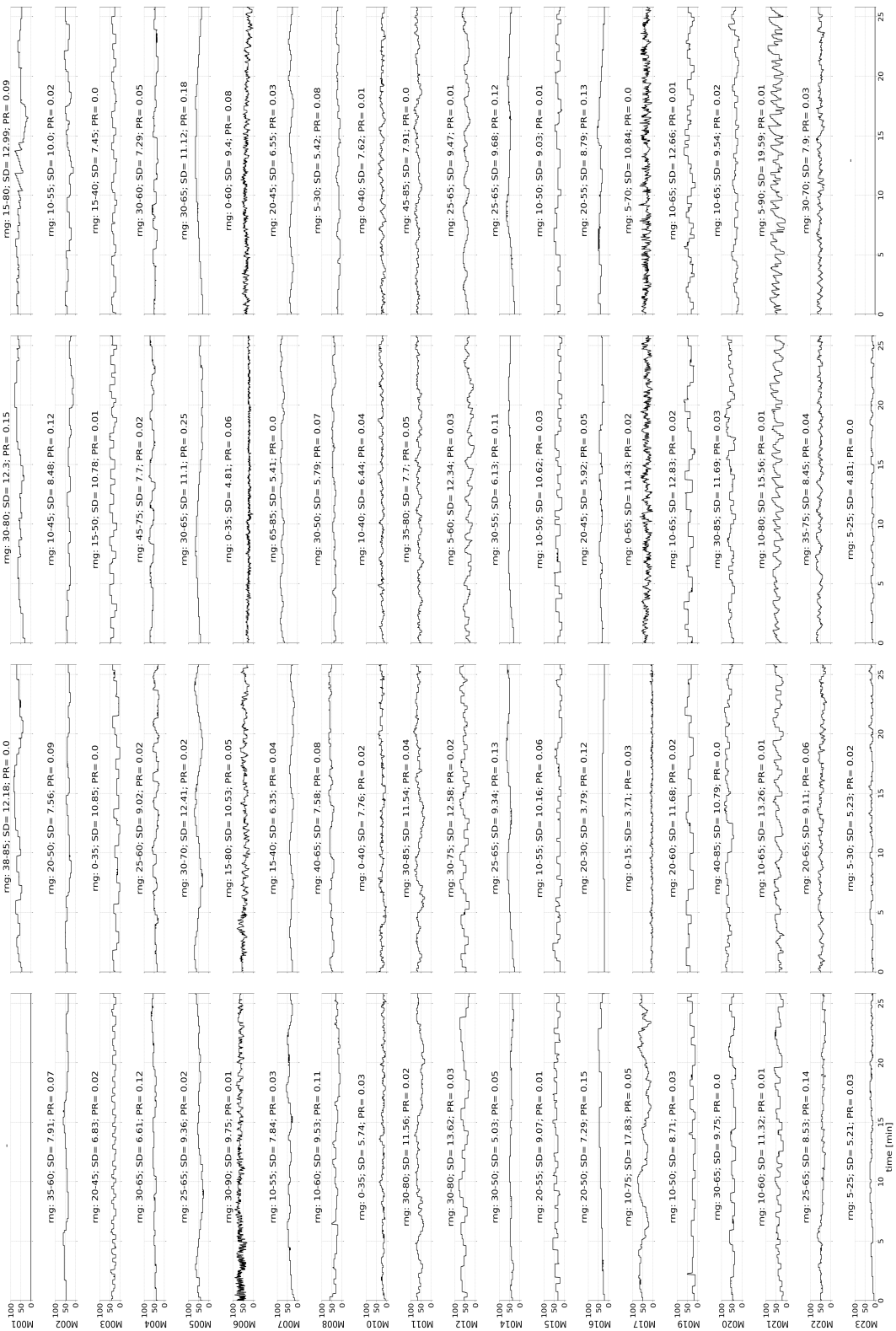

Figure 11.3: CM pain ratings for all 20 patients and four sessions: the range (rng), the standard deviation (SD) and the parameter (PR) are given for each time course.

subj	f/m	age	pain duration	pain location	medication	pain intensity	PCS	d/a/s
1	f	52	32	thoracic	-	4	14	1/4/11
2	m	64	2	lumbar	-	3	22	3/5/7
3	f	39	8	lumbar	Ibuprofen 600 mg (10-12x/month))	4	32	7/9/16
4	f	41	18	lumbar	Fluoxetine 20 mg (daily), Paracetamol 500 mg (2-3x/month), Orphenadrine 100mg (3x/month)	3	33	6/7/11
5	f	60	14	thoracic	Diclofenac 69,82 mg (1x/month)	4	14	2/5/6
6	f	39	3	lumbar	Paracetamol 500mg (2-3x/month), Ibuprofen 400mg (2x/month)	4	13	2/1/1
7	f	48	5	cervical	Ibuprofen 400mg (4x/month)	5	12	4/0/6
8	f	52	11	thoracic/lumbar	Ibuprofen 400mg (5x/month), Metamizole 500mg (2x/month)	4	7	1/2/5
9	f	31	6	lumbar	Ibuprofen 800mg (2-3x/month), Metamizole 1000mg (2-3x/month)	5	1	0/0/1
10	m	26	4	lumbar	-	5	9	0/3/3
11	f	55	16	thoracic/lumbar	Cannabis drops (15x/month)	10	11	5/2/6
12	m	65	8	lumbar	Ibuprofen 600mg (10-15x/month)	4	10	2/2/3
13	f	31	1	cervical/thoracic	Ibuprofen 400mg (18x/month)	3	25	9/6/14
14	m	32	7	thoracic/lumbar	Ibuprofen 600mg (6x/month), Tramadol 100mg (10x/month)	5	22	7/3/5
15	f	26	10	lumbar	Ibuprofen 400mg (1x/month)	4	18	6/3/8
16	f	55	16	cervical/thoracic	Metamizole 500mg (2-3x/month)	5	2	4/0/4
17	f	56	15	lumbar	-	7	36	4/4/13
18	f	42	11	thoracic/lumbar	-	5	10	1/2/6
19	f	30	3	thoracic	Ibuprofen 400mg (3x/month)	4	27	2/4/8
20	f	43	10	cervical/lumbar	Ibuprofen 400mg (5x/month)	7	22	5/4/6

Table 11.7: CBP patient characteristics and questionnaires: male/female; PCS: pain catastrophizing scale; d/a/s: depression/anxiety/stress. The cutoff for depression and stress is 10, for anxiety 6, and for the PCS 30.

subj	f/m	age	pain duration	medication	pain intensity	PCS	d/a/s
1	f	61	50	Sumatriptan 100mg (20x/month)	7	15	0/10/9
2	f	27	7	Metamizole 500mg (2-3x/month), Sumatriptan 50mg (1x/month)	4	5	0/0/2
3	f	50	35	Sumatriptan 100mg (5-7x/month)	4	24	5/0/6
4	f	27	8	Zolmitriptan 20mg (2x/month), Ibuprofen 600mg (7x/month)	7	37	1/1/8
5	m	49	30	Ibuprofen 600mg (7-8x/month), Metamizole 500mg (3-4x/month), Paracetamol 500mg (5-6x/month)	4	3	0/6/1
6	f	52	30	Ibuprofen 400mg (6x/month), Paracetamol 1000mg (2x/month)	5	11	5/10/12
7	f	32	15	Zolmitriptan 5mg (8x/month), Naproxen 500mg (15x/month), Acetylsalicylic Acid(ASA) 250mg (4x/month), Paracetamol 200mg (4x/month), Caffeine 50mg (4x/month)	4	31	5/7/7
8	f	21	7	Sumatriptan 50mg (1x/month)	4	10	2/1/0
9	f	19	7	-	4	35	10/2/6
10	f	46	13	Ibuprofen 800mg (8-10x/month)	6	31	7/10/15
11	f	27	13	Triptan (2-3x/month), Caffeine 50mg (20-25x/month) Paracetamol 250mg (20-25x/month), ASA 250mg (20-25x/month)	4	13	6/1/10
12	m	53	15	Ibuprofen 600mg (10x/month)	6	20	7/2/4
13	f	30	6	Ibuprofen 400mg (4x/month)	4	24	1/1/5
14	f	21	7	Ibuprofen 600mg (4-8x/month), Paracetamol 500mg (4x/month), Zolmitriptan 5mg (1-2x/month)	3	15	2/0/5
15	f	23	8	Ibuprofen 600mg (2-3x/month)	7	24	2/0/3

Table 11.8: CM patient characteristics and questionnaires part 1: male/female; PCS: pain catastrophizing scale; d/a/s: depression/anxiety/stress. The cutoff for depression and stress is 10, for anxiety 6, and for the PCS 30.

subj	f/m	age	pain duration	medication	pain intensity	PCS	d/a/s
16	f	28	7	Ibuprofen 500mg (10x/month)	7	11	0/1/1
17	f	25	5	Ibuprofen 600mg (5x/month), Zolmitriptan 5mg (1x/month)	4	21	5/5/9
18	f	33	20	Paracetamol 500mg (3x/month)	5	32	4/0/4
19	f	21	9	Ibuprofen 400mg (6-10x/month), Rizatriptan 10mg (2x/month)	5	30	1/1/2
20	f	43	10	Ibuprofen 400mg (20x/month), Paracetamol 325 mg (8-10x/month), Naproxen 100 mg (8-10x/month), Caffeine 50 mg (8-10x/month), Drotaverine hydrochloride 40 mg (8-10x/month),) Pheniramine 10 mg (8-10x/month)	4	22	2/3/9

Table 11.9: CM patient characteristics and questionnaires part 2: male/female; PCS: pain catastrophizing scale; d/a/s: depression/anxiety/stress. The cutoff for depression and stress is 10, for anxiety 6, and for the PCS 30.

Bibliography

[1] Asma Hayati Ahmad and Che Badariah Abdul Aziz. "The brain in pain". In: *The Malaysian journal of medical sciences: MJMS* 21.Spec Issue (2014), p. 46.

[2] Arkan Al-Zubaidi et al. "Machine learning based classification of resting-state fMRI features exemplified by metabolic state (hunger/satiety)". In: *Frontiers in human neuroscience* 13 (2019), p. 164.

[3] Sarah Aliko et al. "A naturalistic neuroimaging database for understanding the brain using ecological stimuli". In: *Scientific Data* 7.1 (2020), pp. 1–21.

[4] Elena A Allen et al. "Tracking whole-brain connectivity dynamics in the resting state". In: *Cerebral cortex* 24.3 (2014), pp. 663–676.

[5] Z Alshelh et al. "Disruption of default mode network dynamics in acute and chronic pain states". In: *NeuroImage: Clinical* 17 (2018), pp. 222–231.

[6] Michael Amann, Jochen G Hirsch, and Achim Gass. "A serial functional connectivity MRI study in healthy individuals assessing the variability of connectivity measures: reduced interhemispheric connectivity in the motor network during continuous performance". In: *Magnetic resonance imaging* 27.10 (2009), pp. 1347–1359.

[7] Anders H Andersen, Don M Gash, and Malcolm J Avison. "Principal component analysis of the dynamic response measured by fMRI: a generalized linear systems framework". In: *Magnetic resonance imaging* 17.6 (1999), pp. 795–815.

[8] Jeffrey S Anderson et al. "Reproducibility of single-subject functional connectivity measurements". In: *American journal of neuroradiology* 32.3 (2011), pp. 548–555.

[9] X Michelle Androulakis et al. "Central executive and default mode network intranet work functional connectivity patterns in chronic migraine". In: *Journal of neurological disorders* 6.5 (2018).

[10] X Michelle Androulakis et al. "Modulation of intrinsic resting-state fMRI networks in women with chronic migraine". In: *Neurology* 89.2 (2017), pp. 163–169.

[11] X Michelle Androulakis et al. "Modulation of salience network intranetwork resting state functional connectivity in women with chronic migraine". In: *Cephalalgia* 38.11 (2018), pp. 1731–1741.

[12] A Vania Apkarian, Marwan N Baliki, and Paul Y Geha. "Towards a theory of chronic pain". In: *Progress in neurobiology* 87.2 (2009), pp. 81–97.

[13] A Vania Apkarian, Javeria A Hashmi, and Marwan N Baliki. "Pain and the brain: specificity and plasticity of the brain in clinical chronic pain". In: *Pain* 152.3 Suppl (2011), S49.

[14] A Vania Apkarian et al. "Chronic back pain is associated with decreased prefrontal and thalamic gray matter density". In: *Journal of neuroscience* 24.46 (2004), pp. 10410–10415.

[15] A Vania Apkarian et al. "Human brain mechanisms of pain perception and regulation in health and disease". In: *European journal of pain* 9.4 (2005), pp. 463–484.

[16] A Vania Apkarian et al. "Imaging the pain of low back pain: functional magnetic resonance imaging in combination with monitoring subjective pain perception allows the study of clinical pain states". In: *Neuroscience letters* 299.1-2 (2001), pp. 57–60.

[17] A Vania Apkarian et al. "Prefrontal cortical hyperactivity in patients with sympathetically mediated chronic pain". In: *Neuroscience letters* 311.3 (2001), pp. 193–197.

[18] Mohammad R Arbabshirani et al. "Single subject prediction of brain disorders in neuroimaging: Promises and pitfalls". In: *Neuroimage* 145 (2017), pp. 137–165.

[19] Lauren Y Atlas et al. "Brain mediators of predictive cue effects on perceived pain". In: *Journal of Neuroscience* 30.39 (2010), pp. 12964–12977.

[20] Baptiste Auguie. *gridExtra: Miscellaneous Functions for "Grid" Graphics*. R package version 2.3. 2017. URL: `https://CRAN.R-project.org/package=gridExtra`.

[21] Sheena K Aurora and Mitchell F Brin. "Chronic migraine: an update on physiology, imaging, and the mechanism of action of two available pharmacologic therapies". In: *Headache: The Journal of Head and Face Pain* 57.1 (2017), pp. 109–125.

[22] Frederico AC Azevedo et al. "Equal numbers of neuronal and nonneuronal cells make the human brain an isometrically scaled-up primate brain". In: *Journal of Comparative Neurology* 513.5 (2009), pp. 532–541.

[23] *BOLD Contrast Mechanism*. http://www.mriquestions.com/bold-contrast.html. Accessed: 2021-06-25. 2021.

[24] Pablo Balenzuela et al. "Modular organization of brain resting state networks in chronic back pain patients". In: *Frontiers in neuroinformatics* 4 (2010), p. 116.

[25] Marwan N Baliki, Alex T Baria, and A Vania Apkarian. "The cortical rhythms of chronic back pain". In: *Journal of Neuroscience* 31.39 (2011), pp. 13981–13990.

[26] Marwan N Baliki et al. "Beyond feeling: chronic pain hurts the brain, disrupting the default-mode network dynamics". In: *Journal of Neuroscience* 28.6 (2008), pp. 1398–1403.

[27] Marwan N Baliki et al. "Brain morphological signatures for chronic pain". In: *PloS one* 6.10 (2011), e26010.

[28] Marwan N Baliki et al. "Chronic pain and the emotional brain: specific brain activity associated with spontaneous fluctuations of intensity of chronic back pain". In: *Journal of Neuroscience* 26.47 (2006), pp. 12165–12173.

[29] Marwan N Baliki et al. "Corticostriatal functional connectivity predicts transition to chronic back pain". In: *Nature neuroscience* 15.8 (2012), pp. 1117–1119.

[30] Marwan N Baliki et al. "Functional reorganization of the default mode network across chronic pain conditions". In: *PloS one* 9.9 (2014), e106133.

[31] Marwan N Baliki et al. "Predicting value of pain and analgesia: nucleus accumbens response to noxious stimuli changes in the presence of chronic pain". In: *Neuron* 66.1 (2010), pp. 149–160.

[32] Meredith J Barad et al. "Complex regional pain syndrome is associated with structural abnormalities in pain-related regions of the human brain". In: *The Journal of Pain* 15.2 (2014), pp. 197–203.

[33] André M Bastos and Jan-Mathijs Schoffelen. "A tutorial review of functional connectivity analysis methods and their interpretational pitfalls". In: *Frontiers in systems neuroscience* 9 (2016), p. 175.

[34] Christian F Beckmann, Mark Jenkinson, and Stephen M Smith. "General multilevel linear modeling for group analysis in FMRI". In: *Neuroimage* 20.2 (2003), pp. 1052–1063.

[35] Henrik Bengtsson. *A Unifying Framework for Parallel and Distributed Processing in R using Futures*. 2020. arXiv: 2008.00553 [cs.DC]. URL: https://arxiv.org/abs/2008.00553.

[36] Sara E Berger et al. "Hippocampal morphology mediates biased memories of chronic pain". In: *Neuroimage* 166 (2018), pp. 86–98.

[37] Jorge L Bernal-Rusiel et al. "Statistical analysis of longitudinal neuroimage data with linear mixed effects models". In: *Neuroimage* 66 (2013), pp. 249–260.

[38] Jeff Bezanson et al. "Julia: A fresh approach to numerical computing". In: *SIAM review* 59.1 (2017), pp. 65–98.

[39] ME Bigal et al. "Prevalence and characteristics of allodynia in headache sufferers: a population study". In: *Neurology* 70.17 (2008), pp. 1525–1533.

[40] Başar Bilgiç et al. "Volumetric differences suggest involvement of cerebellum and brainstem in chronic migraine". In: *Cephalalgia* 36.4 (2016), pp. 301–308.

[41] Rasmus M Birn et al. "The effect of scan length on the reliability of resting-state fMRI connectivity estimates". In: *Neuroimage* 83 (2013), pp. 550–558.

[42] David Borsook, Simona Sava, and Lino Becerra. "The pain imaging revolution: advancing pain into the 21st century". In: *The Neuroscientist* 16.2 (2010), pp. 171–185.

[43] George EP Box et al. *Time series analysis: forecasting and control*. John Wiley & Sons, 2015.

[44] Leo Breiman et al. *Classification and regression trees*. Routledge, 2017.

[45] Kay H Brodersen et al. "Decoding the perception of pain from fMRI using multivariate pattern analysis". In: *Neuroimage* 63.3 (2012), pp. 1162–1170.

[46] Jonathan Brooks and Irene Tracey. "From nociception to pain perception: imaging the spinal and supraspinal pathways". In: *Journal of anatomy* 207.1 (2005), pp. 19–33.

[47] Justin E Brown et al. "Towards a physiology-based measure of pain: patterns of human brain activity distinguish painful from non-painful thermal stimulation". In: *PloS one* 6.9 (2011), e24124.

[48] Rachelle Buchbinder et al. "Placing the global burden of low back pain in context". In: *Best Practice & Research Clinical Rheumatology* 27.5 (2013), pp. 575–589.

[49] Randy L Buckner. "Event-related fMRI and the hemodynamic response". In: *Human brain mapping* 6.5-6 (1998), pp. 373–377.

[50] Randy L Buckner, Fenna M Krienen, and BT Thomas Yeo. "Opportunities and limitations of intrinsic functional connectivity MRI". In: *Nature neuroscience* 16.7 (2013), pp. 832–837.

[51] Rami Burstein, Rodrigo Noseda, and David Borsook. "Migraine: multiple processes, complex pathophysiology". In: *Journal of Neuroscience* 35.17 (2015), pp. 6619–6629.

[52] DC Buse et al. "Sociodemographic and comorbidity profiles of chronic migraine and episodic migraine sufferers". In: *Journal of Neurology, Neurosurgery & Psychiatry* 81.4 (2010), pp. 428–432.

[53] M Catherine Bushnell, Marta Čeko, and Lucie A Low. "Cognitive and emotional control of pain and its disruption in chronic pain". In: *Nature Reviews Neuroscience* 14.7 (2013), pp. 502–511.

[54] Richard B Buxton. "The physics of functional magnetic resonance imaging (fMRI)". In: *Reports on Progress in Physics* 76.9 (2013), p. 096601.

[55] Richard B Buxton, Eric C Wong, and Lawrence R Frank. "Dynamics of blood flow and oxygenation changes during brain activation: the balloon model". In: *Magnetic resonance in medicine* 39.6 (1998), pp. 855–864.

[56] Paul T Callaghan. *Principles of nuclear magnetic resonance microscopy*. Oxford University Press on Demand, 1993.

[57] Daniel Callan et al. "A tool for classifying individuals with chronic back pain: using multivariate pattern analysis with functional magnetic resonance imaging data". In: *PloS one* 9.6 (2014), e98007.

[58] HR Casser et al. "Deutscher schmerzfragebogen (DSF) und standardisierte dokumentation mit KEDOQ-schmerz". In: *Der Schmerz* 26.2 (2012), pp. 168–175.

[59] Guillermo A Cecchi et al. "Predictive dynamics of human pain perception". In: *PLoS Comput Biol* 8.10 (2012), e1002719.

[60] Catie Chang and Gary H Glover. "Time–frequency dynamics of resting-state brain connectivity measured with fMRI". In: *Neuroimage* 50.1 (2010), pp. 81–98.

[61] Heather Chapin, Epifanio Bagarinao, and Sean Mackey. "Real-time fMRI applied to pain management". In: *Neuroscience letters* 520.2 (2012), pp. 174–181.

[62] Gang Chen et al. "Linear mixed-effects modeling approach to FMRI group analysis". In: *Neuroimage* 73 (2013), pp. 176–190.

[63] Jingyuan E Chen and Gary H Glover. "Functional magnetic resonance imaging methods". In: *Neuropsychology review* 25.3 (2015), pp. 289–313.

[64] Tianqi Chen and Carlos Guestrin. "Xgboost: A scalable tree boosting system". In: *Proceedings of the 22nd acm sigkdd international conference on knowledge discovery and data mining*. 2016, pp. 785–794.

[65] Zhiye Chen et al. "Altered functional connectivity of amygdala underlying the neuromechanism of migraine pathogenesis". In: *The journal of headache and pain* 18.1 (2017), pp. 1–8.

[66] Zhiye Chen et al. "Volume of hypothalamus as a diagnostic biomarker of chronic migraine". In: *Frontiers in neurology* 10 (2019), p. 606.

[67] Rastko Ciric et al. "Benchmarking of participant-level confound regression strategies for the control of motion artifact in studies of functional connectivity". In: *Neuroimage* 154 (2017), pp. 174–187.

[68] Rastko Ciric et al. "Mitigating head motion artifact in functional connectivity MRI". In: *Nature Protocols* 13.12 (2018), pp. 2801–2826.

[69] Jens Claassen et al. "Cerebellum is more concerned about visceral than somatic pain". In: *Journal of Neurology, Neurosurgery & Psychiatry* 91.2 (2020), pp. 218–219.

[70] Gianluca Coppola et al. "Aberrant interactions of cortical networks in chronic migraine: a resting-state fMRI study". In: *Neurology* 92.22 (2019), e2550–e2558.

[71] Gianluca Coppola et al. "Cerebral gray matter volume in patients with chronic migraine: correlations with clinical features". In: *The journal of headache and pain* 18.1 (2017), pp. 1–9.

[72] Gianluca Coppola et al. "Resting state connectivity between default mode network and insula encodes acute migraine headache". In: *Cephalalgia* 38.5 (2018), pp. 846–854.

[73] Adele Cutler, D Richard Cutler, and John R Stevens. "Tree-based methods". In: *High-Dimensional Data Analysis in Cancer Research*. Springer, 2009, pp. 1–19.

[74] Karen D Davis et al. "Brain imaging tests for chronic pain: medical, legal and ethical issues and recommendations". In: *Nature Reviews Neurology* 13.10 (2017), p. 624.

[75] Timothy L Davis et al. "Calibrated functional MRI: mapping the dynamics of oxidative metabolism". In: *Proceedings of the National Academy of Sciences* 95.4 (1998), pp. 1834–1839.

[76] Bettina Deak et al. "Intrinsic Network Activity Reflects the Fluctuating Experience of Tonic Pain". In: *bioRxiv* (2021).

[77] Marie Denuelle et al. "Hypothalamic activation in spontaneous migraine attacks". In: *Headache: The Journal of Head and Face Pain* 47.10 (2007), pp. 1418–1426.

[78] Martin Diers et al. "Central processing of acute muscle pain in chronic low back pain patients: an EEG mapping study". In: *Journal of clinical neurophysiology* 24.1 (2007), pp. 76–83.

[79] David W Dodick. "A phase-by-phase review of migraine pathophysiology". In: *Headache: the journal of head and face pain* 58 (2018), pp. 4–16.

[80] Yuhui Du, Zening Fu, and Vince D Calhoun. "Classification and prediction of brain disorders using functional connectivity: promising but challenging". In: *Frontiers in neuroscience* 12 (2018), p. 525.

[81] R.R. Edelman and J.R. Hesselink. *Clinical Magnetic Resonance Imaging*. Saunders, 1990. ISBN: 9780721622415. URL: https://books.google.de/books?id=gMk1c_KXVsoC.

[82] Robert R Edwards. "Individual differences in endogenous pain modulation as a risk factor for chronic pain". In: *Neurology* 65.3 (2005), pp. 437–443.

[83] Oscar Esteban et al. "fMRIPrep: a robust preprocessing pipeline for functional MRI". In: *Nature methods* 16.1 (2019), pp. 111–116.

[84] Alan C Evans et al. "3D statistical neuroanatomical models from 305 MRI volumes". In: *1993 IEEE conference record nuclear science symposium and medical imaging conference*. IEEE. 1993, pp. 1813–1817.

[85] *FMRI Experimental Design*. https://afni.nimh.nih.gov/pub/dist/HOWTO/howto/ht03_stim/html/stim_background.html. Accessed: 2021-06-25. 2004.

[86] *FSL Motion Outliers*. https://fsl.fmrib.ox.ac.uk/fsl/fslwiki/FSLMotionOutliers. Accessed: 2021-07-02. 2018.

[87] Victoria Fasick et al. "The hippocampus and TNF: Common links between chronic pain and depression". In: *Neuroscience & Biobehavioral Reviews* 53 (2015), pp. 139–159.

[88] Massimo Filippi and Roberta Messina. "The chronic migraine brain: what have we learned from neuroimaging?" In: *Frontiers in neurology* 10 (2020), p. 1356.

[89] Bruce Fischl et al. "High-resolution intersubject averaging and a coordinate system for the cortical surface". In: *Human brain mapping* 8.4 (1999), pp. 272–284.

[90] Pär Flodin et al. "Intrinsic brain connectivity in chronic pain: a resting-state fMRI study in patients with rheumatoid arthritis". In: *Frontiers in human neuroscience* 10 (2016), p. 107.

[91] Elia Formisano, Federico De Martino, and Giancarlo Valente. "Multivariate analysis of fMRI time series: classification and regression of brain responses using machine learning". In: *Magnetic resonance imaging* 26.7 (2008), pp. 921–934.

[92] Nicholas J Foti and Emily B Fox. "Statistical model-based approaches for functional connectivity analysis of neuroimaging data". In: *Current opinion in neurobiology* 55 (2019), pp. 48–54.

[93] Karl J Friston et al. "Mixed-effects and fMRI studies". In: *Neuroimage* 24.1 (2005), pp. 244–252.

[94] Karl J Friston et al. "Nonlinear event-related responses in fMRI". In: *Magnetic resonance in medicine* 39.1 (1998), pp. 41–52.

[95] Karl J Friston et al. "Nonlinear responses in fMRI: the Balloon model, Volterra kernels, and other hemodynamics". In: *NeuroImage* 12.4 (2000), pp. 466–477.

[96] Karl J Friston et al. "Spatial registration and normalization of images". In: *Human brain mapping* 3.3 (1995), pp. 165–189.

[97] Ikuko Funatogawa and Takashi Funatogawa. *Longitudinal data analysis: Autoregressive linear mixed effects models*. Springer, 2018.

[98] Pierre Geurts, Alexandre Irrthum, and Louis Wehenkel. "Supervised learning with decision tree-based methods in computational and systems biology". In: *Molecular Biosystems* 5.12 (2009), pp. 1593–1605.

[99] Ali Gholipour et al. "Brain functional localization: a survey of image registration techniques". In: *IEEE transactions on medical imaging* 26.4 (2007), pp. 427–451.

[100] T Giesecke et al. "Central pain processing in chronic low back pain. Evidence for reduced pain inhibition". In: *Schmerz (Berlin, Germany)* 20.5 (2006), pp. 411–4.

[101] Thorsten Giesecke et al. "Evidence of augmented central pain processing in idiopathic chronic low back pain". In: *Arthritis & Rheumatism: Official Journal of the American College of Rheumatology* 50.2 (2004), pp. 613–623.

[102] Joshua I Glaser et al. "The roles of supervised machine learning in systems neuroscience". In: *Progress in neurobiology* 175 (2019), pp. 126–137.

[103] Matthew F Glasser et al. "A multi-modal parcellation of human cerebral cortex". In: *Nature* 536.7615 (2016), pp. 171–178.

[104] Gary H Glover. "Overview of functional magnetic resonance imaging". In: *Neurosurgery Clinics* 22.2 (2011), pp. 133–139.

[105] Rainer Goebel, Fabrizio Esposito, and Elia Formisano. "Analysis of functional image analysis contest (FIAC) data with brainvoyager QX: From single-subject to cortically aligned group general linear model analysis and self-organizing group independent component analysis". In: *Human brain mapping* 27.5 (2006), pp. 392–401.

[106] Michael S Gold and Gerald F Gebhart. "Nociceptor sensitization in pain pathogenesis". In: *Nature medicine* 16.11 (2010), pp. 1248–1257.

[107] Randy L Gollub et al. "A functional neuroimaging study of expectancy effects on pain response in patients with knee osteoarthritis". In: *The Journal of Pain* 19.5 (2018), pp. 515–527.

[108] Nina Goossens et al. "Association between sensorimotor impairments and functional brain changes in patients with low back pain: a critical review". In: *American journal of physical medicine & rehabilitation* 97.3 (2018), pp. 200–211.

[109] Evan M Gordon et al. "Precision functional mapping of individual human brains". In: *Neuron* 95.4 (2017), pp. 791–807.

[110] Richard H Gracely et al. "Functional magnetic resonance imaging evidence of augmented pain processing in fibromyalgia". In: *Arthritis & Rheumatism* 46.5 (2002), pp. 1333–1343.

[111] Deanna J Greene et al. "Integrative and network-specific connectivity of the basal ganglia and thalamus defined in individuals". In: *Neuron* 105.4 (2020), pp. 742–758.

[112] Ludovica Griffanti et al. "ICA-based artefact removal and accelerated fMRI acquisition for improved resting state network imaging". In: *Neuroimage* 95 (2014), pp. 232–247.

[113] Débora Bevilaqua Grossi et al. "Pressure pain threshold in the craniocervical muscles of women with episodic and chronic migraine: a controlled study". In: *Arquivos de neuro-psiquiatria* 69 (2011), pp. 607–612.

[114] E Mark Haacke et al. *Magnetic resonance imaging: physical principles and sequence design*. Vol. 82. Wiley-liss New York: 1999.

[115] Daniel A Handwerker et al. "Periodic changes in fMRI connectivity". In: *Neuroimage* 63.3 (2012), pp. 1712–1719.

[116] Lars G Hanson. *Introduction to magnetic resonance imaging techniques*. `http://eprints.drcmr.dk/37/1/MRI_English_a4.pdf`. 2009.

[117] Lars G Hanson. "Is quantum mechanics necessary for understanding magnetic resonance?" In: *Concepts in Magnetic Resonance Part A: An Educational Journal* 32.5 (2008), pp. 329–340.

[118] Javeria A Hashmi et al. "Brain networks predicting placebo analgesia in a clinical trial for chronic back pain". In: *PAIN®* 153.12 (2012), pp. 2393–2402.

[119] Javeria A Hashmi et al. "Lidocaine patch (5%) is no more potent than placebo in treating chronic back pain when tested in a randomised double blind placebo controlled brain imaging study". In: *Molecular pain* 8 (2012), pp. 1744–8069.

[120] Javeria A Hashmi et al. "Shape shifting pain: chronification of back pain shifts brain representation from nociceptive to emotional circuits". In: *Brain* 136.9 (2013), pp. 2751–2768.

[121] Trevor Hastie, Robert Tibshirani, and Jerome Friedman. *The elements of statistical learning: data mining, inference, and prediction*. Springer Science & Business Media, 2009.

[122] Henry Head and Gordon Holmes. "Sensory disturbances from cerebral lesions". In: *Brain* 34.2-3 (1911), pp. 102–254.

[123] Charles R Henderson. "Estimation of variance and covariance components". In: *Biometrics* 9.2 (1953), pp. 226–252.

[124] Luke A Henderson et al. "Chronic pain: lost inhibition?" In: *Journal of Neuroscience* 33.17 (2013), pp. 7574–7582.

[125] Lionel Henry and Hadley Wickham. *purrr: Functional Programming Tools*. R package version 0.3.4. 2020. URL: `https://CRAN.R-project.org/package=purrr`.

[126] Rikkert Hindriks et al. "Can sliding-window correlations reveal dynamic functional connectivity in resting-state fMRI?" In: *Neuroimage* 127 (2016), pp. 242–256.

[127] Francis Houde et al. "Perturbing the activity of the superior temporal gyrus during pain encoding prevents the exaggeration of pain memories: A virtual lesion study using single-pulse transcranial magnetic stimulation". In: *Neurobiology of learning and memory* 169 (2020), p. 107174.

[128] Scott A Huettel. "Event-related fMRI in cognition". In: *Neuroimage* 62.2 (2012), pp. 1152–1156.

[129] Scott A Huettel, Allen W Song, Gregory McCarthy, et al. *Functional magnetic resonance imaging*. Vol. 1. Sinauer Associates Sunderland, MA, 2004.

[130] R Matthew Hutchison et al. "Dynamic functional connectivity: promise, issues, and interpretations". In: *Neuroimage* 80 (2013), pp. 360–378.

[131] Chloe Hutton et al. "Image distortion correction in fMRI: a quantitative evaluation". In: *Neuroimage* 16.1 (2002), pp. 217–240.

[132] *Implementing Real-Time Trending Topics with a Distributed Rolling Count Algorithm in Storm*. `https://www.michael-noll.com/blog/2013/01/18/implementing-real-time-trending-topics-in-storm/`. Accessed: 2021-05-31. 2013.

[133] Martin Ingvar. "Pain and functional imaging". In: *Philosophical Transactions of the Royal Society of London. Series B: Biological Sciences* 354.1387 (1999), pp. 1347–1358.

[134] Mark Jenkinson et al. “Fsl”. In: *Neuroimage* 62.2 (2012), pp. 782–790.

[135] Mark Jenkinson et al. “Improved optimization for the robust and accurate linear registration and motion correction of brain images”. In: *Neuroimage* 17.2 (2002), pp. 825–841.

[136] Mark Jenkinson et al. “Short introduction to the general linear model for neuroimaging”. In: *Retrieved August* 29 (2019).

[137] Tom Johnstone et al. “Motion correction and the use of motion covariates in multiple-subject fMRI analysis”. In: *Human brain mapping* 27.10 (2006), pp. 779–788.

[138] David T Jones et al. “Non-stationarity in the "resting brain's" modular architecture”. In: *PloS one* 7.6 (2012), e39731.

[139] Zaza Katsarava et al. “Defining the differences between episodic migraine and chronic migraine”. In: *Current pain and headache reports* 16.1 (2012), pp. 86–92.

[140] Robert E Kelly Jr et al. “Visual inspection of independent components: defining a procedure for artifact removal from fMRI data”. In: *Journal of neuroscience methods* 189.2 (2010), pp. 233–245.

[141] Christoph Kern, Thomas Klausch, and Frauke Kreuter. “Tree-based machine learning methods for survey research”. In: *Survey research methods*. Vol. 13. 1. NIH Public Access. 2019, p. 73.

[142] Meenakshi Khosla et al. “Machine learning in resting-state fMRI analysis”. In: *Magnetic resonance imaging* 64 (2019), pp. 101–121.

[143] Jong Hyun Kim et al. “Regional grey matter changes in patients with migraine: a voxel-based morphometry study”. In: *Cephalalgia* 28.6 (2008), pp. 598–604.

[144] Seong-Gi Kim and Peter A Bandettini. “Principles of functional MRI”. In: *BOLD fMRI*. Springer, 2010, pp. 3–22.

[145] Arno Klein et al. “Evaluation of 14 nonlinear deformation algorithms applied to human brain MRI registration”. In: *Neuroimage* 46.3 (2009), pp. 786–802.

[146] Yoshitaka Kobayashi et al. “Augmented cerebral activation by lumbar mechanical stimulus in chronic low back pain patients: an FMRI study”. In: *Spine* 34.22 (2009), pp. 2431–2436.

[147] Jian Kong et al. “S1 is associated with chronic low back pain: a functional and structural MRI study”. In: *Molecular pain* 9 (2013), pp. 1744–8069.

[148] Jennifer Kornelsen et al. “Default mode network functional connectivity altered in failed back surgery syndrome”. In: *The Journal of Pain* 14.5 (2013), pp. 483–491.

[149] Florian Krause et al. “Active head motion reduction in magnetic resonance imaging using tactile feedback”. In: *Human brain mapping* 40.14 (2019), pp. 4026–4037.

[150] Jeroen Kregel et al. “Structural and functional brain abnormalities in chronic low back pain: A systematic review”. In: *Seminars in arthritis and rheumatism*. Vol. 45. 2. Elsevier. 2015, pp. 229–237.

[151] Anil Kuchinad et al. “Accelerated brain gray matter loss in fibromyalgia patients: premature aging of the brain?” In: *Journal of Neuroscience* 27.15 (2007), pp. 4004–4007.

[152] Aaron Kucyi and Karen D Davis. “The dynamic pain connectome”. In: *Trends in neurosciences* 38.2 (2015), pp. 86–95.

[153] Aaron Kucyi, Tim V Salomons, and Karen D Davis. “Mind wandering away from pain dynamically engages antinociceptive and default mode brain networks”. In: *Proceedings of the National Academy of Sciences* 110.46 (2013), pp. 18692–18697.

[154] Max Kuhn. *caret: Classification and Regression Training*. R package version 6.0-86. 2020. URL: `https://CRAN.R-project.org/package=caret`.

[155] Max Kuhn, Kjell Johnson, et al. *Applied predictive modeling*. Vol. 26. Springer, 2013.

[156] Michel Lang, Patrick Schratz, and Raphael Sonabend. *mlr3viz: Visualizations for 'mlr3'*. R package version 0.5.1. 2021. URL: `https://CRAN.R-project.org/package=mlr3viz`.

[157] Michel Lang et al. “mlr3: A modern object-oriented machine learning framework in R”. In: *Journal of Open Source Software* (2019). DOI: `10.21105/joss.01903`. URL: `https://joss.theoj.org/papers/10.21105/joss.01903`.

[158] Michel Lang et al. *mlr3learners: Recommended Learners for 'mlr3'*. R package version 0.4.3. 2020. URL: `https://CRAN.R-project.org/package=mlr3learners`.

[159] Mi Ji Lee et al. “Increased connectivity of pain matrix in chronic migraine: a resting-state functional MRI study”. In: *The journal of headache and pain* 20.1 (2019), pp. 1–10.

[160] Steven Lemm et al. “Introduction to machine learning for brain imaging”. In: *Neuroimage* 56.2 (2011), pp. 387–399.

[161] Nora Leonardi and Dimitri Van De Ville. “On spurious and real fluctuations of dynamic functional connectivity during rest”. In: *Neuroimage* 104 (2015), pp. 430–436.

[162] Fleur Lerebours et al. "Functional connectivity of hypothalamus in chronic migraine with medication overuse". In: *Cephalalgia* 39.7 (2019), pp. 892–899.

[163] Janelle E Letzen and Michael E Robinson. "Negative mood influences default mode network functional connectivity in chronic low back pain patients: Implications for functional neuroimaging biomarkers". In: *Pain* 158.1 (2017), p. 48.

[164] Martin A Lindquist and Amanda Mejia. "Zen and the art of multiple comparisons". In: *Psychosomatic medicine* 77.2 (2015), p. 114.

[165] Martin A Lindquist et al. "Modeling the hemodynamic response function in fMRI: efficiency, bias and mismodeling". In: *Neuroimage* 45.1 (2009), S187–S198.

[166] Elena von der Lippe et al. "Prävalenz von Rücken-und Nackenschmerzen in Deutschland. Ergebnisse der Krankheitslast-Studie BURDEN 2020". In: (2021).

[167] Donna Lloyd et al. "Differences in low back pain behavior are reflected in the cerebral response to tactile stimulation of the lower back". In: *Spine* 33.12 (2008), pp. 1372–1377.

[168] Oleg V Lobanov et al. "Frontoparietal mechanisms supporting attention to location and intensity of painful stimuli". In: *PAIN®* 154.9 (2013), pp. 1758–1768.

[169] Marco L Loggia et al. "Default mode network connectivity encodes clinical pain: an arterial spin labeling study". In: *PAIN®* 154.1 (2013), pp. 24–33.

[170] Peter F Lovibond and Sydney H Lovibond. "The structure of negative emotional states: Comparison of the Depression Anxiety Stress Scales (DASS) with the Beck Depression and Anxiety Inventories". In: *Behaviour research and therapy* 33.3 (1995), pp. 335–343.

[171] Michael Luchtmann et al. "Structural brain alterations in patients with lumbar disc herniation: a preliminary study". In: *PLoS One* 9.3 (2014), e90816.

[172] *Machine Learning FAQ*. `https://sebastianraschka.com/faq/docs/evaluate-a-model.html`. Accessed: 2021-07-07. 2021.

[173] Kristoffer H Madsen et al. "Perspectives on machine learning for classification of schizotypy using fMRI data". In: *Schizophrenia bulletin* 44.suppl_2 (2018), S480–S490.

[174] *Magnete, Spins und Resonanzen*. Accessed: 2021-08-25. URL: `http://www.horbiradio.de/Dokumente%20MTRA/Magnete,Spins%20u.%20Resonanzen.pdf`.

[175] Abdelhak Mahmoudi et al. "Multivoxel pattern analysis for FMRI data: a review". In: *Computational and mathematical methods in medicine* 2012 (2012).

[176] Meena M Makary et al. "Loss of nucleus accumbens low-frequency fluctuations is a signature of chronic pain". In: *Proceedings of the National Academy of Sciences* 117.18 (2020), pp. 10015–10023.

[177] Sanna Malinen et al. "Aberrant temporal and spatial brain activity during rest in patients with chronic pain". In: *Proceedings of the National Academy of Sciences* 107.14 (2010), pp. 6493–6497.

[178] AR Mansour et al. "Chronic pain: the role of learning and brain plasticity". In: *Restorative neurology and neuroscience* 32.1 (2014), pp. 129–139.

[179] Scott Marek et al. "Spatial and temporal organization of the individual human cerebellum". In: *Neuron* 100.4 (2018), pp. 977–993.

[180] Michael Markl and Jochen Leupold. "Gradient echo imaging". In: *Journal of Magnetic Resonance Imaging* 35.6 (2012), pp. 1274–1289.

[181] Andre Marquand et al. "Quantitative prediction of subjective pain intensity from whole-brain fMRI data using Gaussian processes". In: *Neuroimage* 49.3 (2010), pp. 2178–2189.

[182] Katherine T Martucci and Sean C Mackey. "Imaging pain". In: *Anesthesiology clinics* 34.2 (2016), pp. 255–269.

[183] Katherine T Martucci, Pamela Ng, and Sean Mackey. "Neuroimaging chronic pain: what have we learned and where are we going?" In: *Future neurology* 9.6 (2014), pp. 615–626.

[184] Arne May and Laura H Schulte. "Chronic migraine: risk factors, mechanisms and treatment". In: *Nature Reviews Neurology* 12.8 (2016), pp. 455–464.

[185] Elisabeth S May et al. "Prefrontal gamma oscillations reflect ongoing pain intensity in chronic back pain patients". In: *Human brain mapping* 40.1 (2019), pp. 293–305.

[186] David J Mayer and Donald D Price. "Central nervous system mechanisms of analgesia". In: *Pain* 2.4 (1976), pp. 379–404.

[187] Astrid Mayr et al. *Chronic Pain Patients Exhibit Individually Unique Cortical Signatures of Pain*. `https://doi.org/10.1101/2020.09.05.284117`. 2020.

[188] Astrid Mayr et al. *Individually Unique Dynamics of Cortical Connectivity Reflect the Ongoing Intensity of Chronic Pain*. `https://doi.org/10.1101/2021.06.30.450553`. 2021.

[189] Martin J McKeown, Lars Kai Hansen, and Terrence J Sejnowsk. "Independent component analysis of functional MRI: what is signal and what is noise?" In: *Current opinion in neurobiology* 13.5 (2003), pp. 620–629.

[190] Martin J McKeown et al. "Analysis of fMRI data by blind separation into independent spatial components". In: *Human brain mapping* 6.3 (1998), pp. 160–188.

[191] Ronald Melzack. "Phantom limbs and the concept of a neuromatrix". In: *Trends in neurosciences* 13.3 (1990), pp. 88–92.

[192] Ronald Melzack, Patrick D Wall, et al. "Pain mechanisms: a new theory". In: *Science* 150.3699 (1965), pp. 971–979.

[193] Harold Merskey. "Pain terms: a list with definitions and notes on usage. Recommended by the IASP Subcommittee on Taxonomy". In: *Pain* 6 (1979), pp. 249–252.

[194] Harold Merskey and Nikolai Bogduk. "Classification of chronic pain, IASP Task Force on Taxonomy". In: *Seattle, WA: International Association for the Study of Pain Press (Also available online at www. iasp-painorg)* (1994).

[195] Tahmineh Mokhtari, Yiheng Tu, and Li Hu. "Involvement of the hippocampus in chronic pain and depression". In: *Brain Science Advances* 5.4 (2019), pp. 288–298.

[196] Martin M Monti. "Statistical analysis of fMRI time-series: a critical review of the GLM approach". In: *Frontiers in human neuroscience* 5 (2011), p. 28.

[197] Orla Moriarty, Brian E McGuire, and David P Finn. "The effect of pain on cognitive function: a review of clinical and preclinical research". In: *Progress in neurobiology* 93.3 (2011), pp. 385–404.

[198] Debbie L Morton, Javin S Sandhu, and Anthony KP Jones. "Brain imaging of pain: state of the art". In: *Journal of pain research* 9 (2016), p. 613.

[199] Eric A Moulton et al. "The cerebellum and pain: passive integrator or active participator?" In: *Brain research reviews* 65.1 (2010), pp. 14–27.

[200] Jeanette A Mumford and Thomas Nichols. "Modeling and inference of multisubject fMRI data". In: *IEEE Engineering in Medicine and Biology Magazine* 25.2 (2006), pp. 42–51.

[201] Jeanette A Mumford and Russell A Poldrack. "Modeling group fMRI data". In: *Social cognitive and affective neuroscience* 2.3 (2007), pp. 251–257.

[202] Chung Jung Mun et al. "Investigating intraindividual pain variability: methods, applications, issues, and directions". In: *Pain* 160.11 (2019), pp. 2415–2429.

[203] Kevin Murphy et al. "The impact of global signal regression on resting state correlations: are anti-correlated networks introduced?" In: *Neuroimage* 44.3 (2009), pp. 893–905.

[204] Amelia A Mutso et al. "Abnormalities in hippocampal functioning with persistent pain". In: *Journal of Neuroscience* 32.17 (2012), pp. 5747–5756.

[205] Alican Nalci, Bhaskar D Rao, and Thomas T Liu. "Nuisance effects and the limitations of nuisance regression in dynamic functional connectivity fMRI". In: *NeuroImage* 184 (2019), pp. 1005–1031.

[206] Vitaly Napadow et al. "Intrinsic brain connectivity in fibromyalgia is associated with chronic pain intensity". In: *Arthritis & Rheumatism* 62.8 (2010), pp. 2545–2555.

[207] Elizabeth A Necka et al. "Applications of dynamic functional connectivity to pain and its modulation". In: *Pain reports* 4.4 (2019).

[208] Lars Neeb et al. "Structural gray matter alterations in chronic migraine: implications for a progressive disease?" In: *Headache: The Journal of Head and Face Pain* 57.3 (2017), pp. 400–416.

[209] Thomas Nichols and Satoru Hayasaka. "Controlling the familywise error rate in functional neuroimaging: a comparative review". In: *Statistical methods in medical research* 12.5 (2003), pp. 419–446.

[210] David M Niddam et al. "Neurochemical changes in the medial wall of the brain in chronic migraine". In: *Brain* 141.2 (2018), pp. 377–390.

[211] Douglas C Noll and Alberto Vazquez. "Temporal BOLD Characteristics and Non-Linearity". In: ().

[212] Kenneth A Norman et al. "Beyond mind-reading: multi-voxel pattern analysis of fMRI data". In: *Trends in cognitive sciences* 10.9 (2006), pp. 424–430.

[213] *Nuclear Magnetic Resonance*. `https://home.uni-leipzig.de/energy/pdf/freuse4.pdf`. Accessed: 2021-06-25. 2006.

[214] Seiji Ogawa et al. "Brain magnetic resonance imaging with contrast dependent on blood oxygenation". In: *proceedings of the National Academy of Sciences* 87.24 (1990), pp. 9868–9872.

[215] Jes Olesen. "The international classification of headache disorders". In: *Headache: The Journal of Head and Face Pain* 48.5 (2008), pp. 691–693.

[216] Hernando Ombao et al. *Handbook of neuroimaging data analysis*. CRC Press, 2016.

[217] Michael H Ossipov, Gregory O Dussor, Frank Porreca, et al. "Central modulation of pain". In: *The Journal of clinical investigation* 120.11 (2010), pp. 3779–3787.

[218] Rémi Patriat, Richard C Reynolds, and Rasmus M Birn. "An improved model of motion-related signal changes in fMRI". In: *Neuroimage* 144 (2017), pp. 74–82.

[219] William D Penny et al. *Statistical parametric mapping: the analysis of functional brain images*. Elsevier, 2011.

[220] Caleb Perry et al. "The role of hippocampus and amygdala morphology in memory bias of learned fear in youth with chronic pain". In: *The Journal of Pain* 22.5 (2021), p. 604.

[221] Jörg Pfannmöller and Martin Lotze. "Review on biomarkers in the resting-state networks of chronic pain patients". In: *Brain and cognition* 131 (2019), pp. 4–9.

[222] Ceri J Phillips. "The cost and burden of chronic pain". In: *Reviews in pain* 3.1 (2009), pp. 2–5.

[223] Alvaro Planchuelo-Gomez et al. "Structural connectivity alterations in chronic and episodic migraine: A diffusion magnetic resonance imaging connectomics study". In: *Cephalalgia* 40.4 (2020), pp. 367–383.

[224] Markus Ploner et al. "Pain suppresses spontaneous brain rhythms". In: *Cerebral cortex* 16.4 (2006), pp. 537–540.

[225] Russell A Poldrack, Jeanette A Mumford, and Thomas E Nichols. *Handbook of functional MRI data analysis*. Cambridge University Press, 2011.

[226] Jean-Baptiste Poline and Matthew Brett. "The general linear model and fMRI: does love last forever?" In: *Neuroimage* 62.2 (2012), pp. 871–880.

[227] Frank Porreca, Michael H Ossipov, and GF Gebhart. "Chronic pain and medullary descending facilitation". In: *Trends in neurosciences* 25.6 (2002), pp. 319–325.

[228] Michael Porst et al. "Migräne und Spannungskopfschmerz in Deutschland. Prävalenz und Erkrankungsschwere im Rahmen der Krankheitslast-Studie BURDEN 2020". In: (2020).

[229] Jonathan D Power et al. "Methods to detect, characterize, and remove motion artifact in resting state fMRI". In: *Neuroimage* 84 (2014), pp. 320–341.

[230] Jonathan D Power et al. "Spurious but systematic correlations in functional connectivity MRI networks arise from subject motion". In: *Neuroimage* 59.3 (2012), pp. 2142–2154.

[231] Donald D Price. "Psychological and neural mechanisms of the affective dimension of pain". In: *Science* 288.5472 (2000), pp. 1769–1772.

[232] Jingyu Qian et al. "Positive connectivity predicts the dynamic intrinsic topology of the human brain network". In: *Frontiers in systems neuroscience* 12 (2018), p. 38.

[233] *RS-fMRI Analysis*. `http://mriquestions.com/analyze-rs-fmri.html`. Accessed: 2021-07-08. 2021.

[234] Jagath C Rajapakse et al. "Modeling hemodynamic response for analysis of functional MRI time-series". In: *Human brain mapping* 6.4 (1998), pp. 283–300.

[235] Marianne C Reddan and Tor D Wager. "Modeling pain using fMRI: from regions to biomarkers". In: *Neuroscience bulletin* 34.1 (2018), pp. 208–215.

[236] Maximilian F Reiser, Wolfhard Semmler, and Hedvig Hricak. *Magnetic resonance tomography*. Springer Science & Business Media, 2007.

[237] Baxter P Rogers et al. "Assessing functional connectivity in the human brain by fMRI". In: *Magnetic resonance imaging* 25.10 (2007), pp. 1347–1357.

[238] Maria Joao Rosa and Ben Seymour. "Decoding the matrix: benefits and limitations of applying machine learning algorithms to pain neuroimaging". In: *Pain* 155.5 (2014), pp. 864–867.

[239] Paulo N Rosa, Patricia Figueiredo, and Carlos J Silvestre. "On the distinguishability of HRF models in fMRI". In: *Frontiers in computational neuroscience* 9 (2015), p. 54.

[240] Antonio Russo et al. "Pain perception and migraine". In: *Frontiers in neurology* 9 (2018), p. 576.

[241] Ziad S Saad et al. "Analysis and use of FMRI response delays". In: *Human brain mapping* 13.2 (2001), pp. 74–93.

[242] Ünal Sakoğlu et al. "A method for evaluating dynamic functional network connectivity and task-modulation: application to schizophrenia". In: *Magnetic Resonance Materials in Physics, Biology and Medicine* 23.5-6 (2010), pp. 351–366.

[243] Gholamreza Salimi-Khorshidi et al. "Automatic denoising of functional MRI data: combining independent component analysis and hierarchical fusion of classifiers". In: *Neuroimage* 90 (2014), pp. 449–468.

[244] Jürgen Sandkühler and Jonathan Lee. "How to erase memory traces of pain and fear". In: *Trends in neurosciences* 36.6 (2013), pp. 343–352.

[245] Alex Novaes Santana et al. "Using Deep Learning and Resting-State fMRI to Classify Chronic Pain Conditions". In: *Frontiers in neuroscience* 13 (2019), p. 1313.

[246] Theodore D Satterthwaite et al. "An improved framework for confound regression and filtering for control of motion artifact in the preprocessing of resting-state functional connectivity data". In: *Neuroimage* 64 (2013), pp. 240–256.

[247] Antonis D Savva, Georgios D Mitsis, and George K Matsopoulos. "Assessment of dynamic functional connectivity in resting-state fMRI using the sliding window technique". In: *Brain and behavior* 9.4 (2019), e01255.

[248] Alexander Schaefer et al. "Local-global parcellation of the human cerebral cortex from intrinsic functional connectivity MRI". In: *Cerebral cortex* 28.9 (2018), pp. 3095–3114.

[249] Robert F Schmidt et al. *Fundamentals of neurophysiology*. Springer Science & Business Media, 2012.

[250] Frank Schneider, Gereon R Fink, et al. *Funktionelle MRT in psychiatrie und neurologie*. Springer, 2013.

[251] Thomas Schreiber and Andreas Schmitz. "Improved surrogate data for nonlinearity tests". In: *Physical review letters* 77.4 (1996), p. 635.

[252] Laura H Schulte, Angie Allers, and Arne May. "Hypothalamus as a mediator of chronic migraine: evidence from high-resolution fMRI". In: *Neurology* 88.21 (2017), pp. 2011–2016.

[253] Laura H Schulte and Arne May. "The migraine generator revisited: continuous scanning of the migraine cycle over 30 days and three spontaneous attacks". In: *Brain* 139.7 (2016), pp. 1987–1993.

[254] Enrico Schulz et al. "Decoding an individual's sensitivity to pain from the multivariate analysis of EEG data". In: *Cerebral cortex* 22.5 (2012), pp. 1118–1123.

[255] Enrico Schulz et al. "Prefrontal gamma oscillations encode tonic pain in humans". In: *Cerebral cortex* 25.11 (2015), pp. 4407–4414.

[256] Enrico Schulz et al. "Strategy-dependent modulation of cortical pain circuits for the attenuation of pain". In: *Cortex* 113 (2019), pp. 255–266.

[257] Enrico Schulz et al. "Ultra-high-field imaging reveals increased whole brain connectivity underpins cognitive strategies that attenuate pain". In: *Elife* 9 (2020), e55028.

[258] Todd J Schwedt. "Multisensory integration in migraine". In: *Current opinion in neurology* 26.3 (2013), p. 248.

[259] Todd J Schwedt et al. "Accurate classification of chronic migraine via brain magnetic resonance imaging". In: *Headache: The Journal of Head and Face Pain* 55.6 (2015), pp. 762–777.

[260] Todd J Schwedt et al. "Atypical resting-state functional connectivity of affective pain regions in chronic migraine". In: *Headache: The Journal of Head and Face Pain* 53.5 (2013), pp. 737–751.

[261] Todd J Schwedt et al. "Enhanced pain-induced activity of pain-processing regions in a case-control study of episodic migraine". In: *Cephalalgia* 34.12 (2014), pp. 947–958.

[262] Todd J Schwedt et al. "Episodic and chronic migraineurs are hypersensitive to thermal stimuli between migraine attacks". In: *Cephalalgia* 31.1 (2011), pp. 6–12.

[263] Todd J Schwedt et al. "Functional MRI of migraine". In: *The Lancet Neurology* 14.1 (2015), pp. 81–91.

[264] Philip Seeman and Bertha Madras. *Imaging of the human brain in health and disease*. Elsevier, 2013.

[265] David A Seminowicz et al. "Effective treatment of chronic low back pain in humans reverses abnormal brain anatomy and function". In: *Journal of Neuroscience* 31.20 (2011), pp. 7540–7550.

[266] Sadia Shakil, Chin-Hui Lee, and Shella Dawn Keilholz. "Evaluation of sliding window correlation performance for characterizing dynamic functional connectivity and brain states". In: *Neuroimage* 133 (2016), pp. 111–128.

[267] Wei Shen et al. "Visual network alterations in brain functional connectivity in chronic low back pain: A resting state functional connectivity and machine learning study". In: *NeuroImage: Clinical* 22 (2019), p. 101775.

[268] Howard S Smith. *Current therapy in pain*. Elsevier Health Sciences, 2009.

[269] Stephen M Smith et al. "Network modelling methods for FMRI". In: *Neuroimage* 54.2 (2011), pp. 875–891.

[270] Christopher D Smyser et al. "Longitudinal analysis of neural network development in preterm infants". In: *Cerebral cortex* 20.12 (2010), pp. 2852–2862.

[271] T Spisák et al. "Individual functional statistical parametric networks related to interictal epileptic EEG discharges: a dynamic sliding-window study". In: European Congress of Radiology-ECR 2014. 2014.

[272] A Stankewitz, E Schulz, and A May. "Neuronal correlates of impaired habituation in response to repeated trigemino-nociceptive but not to olfactory input in migraineurs: an fMRI study". In: *Cephalalgia* 33.4 (2013), pp. 256–265.

[273] Anne Stankewitz et al. "Trigeminal nociceptive transmission in migraineurs predicts migraine attacks". In: *Journal of Neuroscience* 31.6 (2011), pp. 1937–1943.

[274] Roland Staud. "Abnormal endogenous pain modulation is a shared characteristic of many chronic pain conditions". In: *Expert review of neurotherapeutics* 12.5 (2012), pp. 577–585.

[275] Paul Suetens. *Fundamentals of medical imaging*. Cambridge university press, 2017.

[276] Michael JL Sullivan, Scott R Bishop, and Jayne Pivik. "The pain catastrophizing scale: development and validation." In: *Psychological assessment* 7.4 (1995), p. 524.

[277] Enzo Tagliazucchi et al. "Brain resting state is disrupted in chronic back pain patients". In: *Neuroscience letters* 485.1 (2010), pp. 26–31.

[278] Jean Talairach and Pierre Tournoux. "Co-planar stereotaxic atlas of the human brain Thieme". In: *New York* (1988).

[279] James Theiler et al. "Testing for nonlinearity in time series: the method of surrogate data". In: *Physica D: Nonlinear Phenomena* 58.1-4 (1992), pp. 77–94.

[280] BT Thomas Yeo et al. "The organization of the human cerebral cortex estimated by intrinsic functional connectivity". In: *Journal of neurophysiology* 106.3 (2011), pp. 1125–1165.

[281] Christopher G Thomas, Richard A Harshman, and Ravi S Menon. "Noise reduction in BOLD-based fMRI using component analysis". In: *Neuroimage* 17.3 (2002), pp. 1521–1537.

[282] Stephen L Thorp et al. "Functional connectivity alterations: novel therapy and future implications in chronic pain management". In: *Pain physician* 21.1 (2018), E207–14.

[283] Robert Tibshirani. "Regression shrinkage and selection via the lasso". In: *Journal of the Royal Statistical Society: Series B (Methodological)* 58.1 (1996), pp. 267–288.

[284] Adam Todd et al. "The European epidemic: pain prevalence and socioeconomic inequalities in pain across 19 European countries". In: *European Journal of Pain* 23.8 (2019), pp. 1425–1436.

[285] Irene Tracey and Patrick W Mantyh. "The cerebral signature for pain perception and its modulation". In: *Neuron* 55.3 (2007), pp. 377–391.

[286] Rolf-Detlef Treede et al. "A classification of chronic pain for ICD-11". In: *Pain* 156.6 (2015), p. 1003.

[287] Hoameng Ung et al. "Multivariate classification of structural MRI data detects chronic low back pain". In: *Cerebral cortex* 24.4 (2014), pp. 1037–1044.

[288] Etienne Vachon-Presseau et al. "Multiple faces of pain: effects of chronic pain on the brain regulation of facial expression". In: *Pain* 157.8 (2016), p. 1819.

[289] Koene RA Van Dijk, Mert R Sabuncu, and Randy L Buckner. "The influence of head motion on intrinsic functional connectivity MRI". In: *Neuroimage* 59.1 (2012), pp. 431–438.

[290] Koene RA Van Dijk et al. "Intrinsic functional connectivity as a tool for human connectomics: theory, properties, and optimization". In: *Journal of neurophysiology* 103.1 (2010), pp. 297–321.

[291] Nuutti Vartiainen et al. "Cortical reorganization in primary somatosensory cortex in patients with unilateral chronic pain". In: *The Journal of Pain* 10.8 (2009), pp. 854–859.

[292] Davis Vaughan and Matt Dancho. *furrr: Apply Mapping Functions in Parallel using Futures*. R package version 0.2.3. 2021. URL: `https://CRAN.R-project.org/package=furrr`.

[293] Guillaume Viejo, Thomas Cortier, and Adrien Peyrache. "Brain-state invariant thalamo-cortical coordination revealed by non-linear encoders". In: *PLoS computational biology* 14.3 (2018), e1006041.

[294] Tor D Wager et al. "Accounting for nonlinear BOLD effects in fMRI: parameter estimates and a model for prediction in rapid event-related studies". In: *NeuroImage* 25.1 (2005), pp. 206–218.

[295] Tor D Wager et al. "An fMRI-based neurologic signature of physical pain". In: *New England Journal of Medicine* 368.15 (2013), pp. 1388–1397.

[296] Tor D Wager et al. "Placebo-induced changes in FMRI in the anticipation and experience of pain". In: *Science* 303.5661 (2004), pp. 1162–1167.

[297] Huifang E Wang et al. "A systematic framework for functional connectivity measures". In: *Frontiers in neuroscience* 8 (2014), p. 405.

[298] Ajay D Wasan et al. "Neural correlates of chronic low back pain measured by arterial spin labeling". In: *The Journal of the American Society of Anesthesiologists* 115.2 (2011), pp. 364–374.

[299] Hadley Wickham. *ggplot2: Elegant Graphics for Data Analysis*. Springer-Verlag New York, 2016. ISBN: 978-3-319-24277-4. URL: `https://ggplot2.tidyverse.org`.

[300] Hadley Wickham et al. *dplyr: A Grammar of Data Manipulation*. R package version 1.0.3. 2021. URL: `https://CRAN.R-project.org/package=dplyr`.

[301] Matthias J Wieser and Paul Pauli. "Neuroscience of pain and emotion". In: *Neuroscience of Pain, Stress, and Emotion*. Elsevier, 2016, pp. 3–27.

[302] Gagan S Wig, Bradley L Schlaggar, and Steven E Petersen. "Concepts and principles in the analysis of brain networks". In: *Annals of the New York Academy of Sciences* 1224.1 (2011), pp. 126–146.

[303] GN Wilkinson and CE Rogers. "Symbolic description of factorial models for analysis of variance". In: *Journal of the Royal Statistical Society: Series C (Applied Statistics)* 22.3 (1973), pp. 392–399.

[304] Anderson M Winkler et al. "Non-parametric combination and related permutation tests for neuroimaging". In: *Human brain mapping* 37.4 (2016), pp. 1486–1511.

[305] Anderson M Winkler et al. "Permutation inference for the general linear model". In: *Neuroimage* 92 (2014), pp. 381–397.

[306] Joel S Winston et al. "Relative valuation of pain in human orbitofrontal cortex". In: *Journal of Neuroscience* 34.44 (2014), pp. 14526–14535.

[307] Viktor Witkovskỳ. "Estimation, testing, and prediction regions of the fixed and random effects by solving the Henderson's mixed model equations". In: *arXiv preprint arXiv:1212.5669* (2012).

[308] Choong-Wan Woo et al. "Building better biomarkers: brain models in translational neuroimaging". In: *Nature neuroscience* 20.3 (2017), p. 365.

[309] Roger P Woods et al. "Automated image registration: I. General methods and intrasubject, intramodality validation". In: *Journal of computer assisted tomography* 22.1 (1998), pp. 139–152.

[310] Clifford J Woolf. "Central sensitization: implications for the diagnosis and treatment of pain". In: *Pain* 152.3 (2011), S2–S15.

[311] Mark W Woolrich, Timothy EJ Behrens, and Stephen M Smith. "Constrained linear basis sets for HRF modelling using Variational Bayes". In: *NeuroImage* 21.4 (2004), pp. 1748–1761.

[312] *XGBoost Parameters*. `https://xgboost.readthedocs.io/en/latest/parameter.html`. Accessed: 2021-06-13. 2020.

[313] Mun Fei Yam et al. "General pathways of pain sensation and the major neurotransmitters involved in pain regulation". In: *International journal of molecular sciences* 19.8 (2018), p. 2164.

[314] Chao-Gan Yan et al. "A comprehensive assessment of regional variation in the impact of head micromovements on functional connectomics". In: *Neuroimage* 76 (2013), pp. 183–201.

[315] Seoyon Yang and Min Cheol Chang. "Chronic pain: structural and functional changes in brain structures and associated negative affective states". In: *International journal of molecular sciences* 20.13 (2019), p. 3130.

[316] Zhengshi Yang et al. "Robust motion regression of resting-state data using a convolutional neural network model". In: *Frontiers in neuroscience* 13 (2019), p. 169.

[317] Jacqueline N Zadelaar et al. "Are individual differences quantitative or qualitative? An integrated behavioral and fMRI MIMIC approach". In: *NeuroImage* 202 (2019), p. 116058.

[318] Achim Zeileis and Gabor Grothendieck. "zoo: S3 Infrastructure for Regular and Irregular Time Series". In: *Journal of Statistical Software* 14.6 (2005), pp. 1–27. DOI: `10.18637/jss.v014.i06`.

[319] Yuan Zhong et al. "Detecting functional connectivity in fMRI using PCA and regression analysis". In: *Brain topography* 22.2 (2009), pp. 134–144.

List of Figures

List of Tables

Acknowledgement

I would like to thank the following people, without whom I would not have been able to complete my thesis:

First, I want to thank Prof. Dr. Straube for giving me the opportunity to pursue my doctorate at the Department of Neurology at the Ludwig-Maximilians-University Hospital, Munich.

Special thanks to Prof. Dr. rer. nat. Olaf Dietrich for the supervision of my thesis. I am very grateful for the interesting discussions and the always helpful advice.

I would like to thank Dr. Enrico Schulz for the consistent support and guidance throughout this project as well as the trust in my abilities.

Many thanks to Dr. Andreas Bender for the support and patience throughout our online meetings.

Furthermore, I would like to thank the 'MRI-Team' Pauline and Bettina as well as the 'EEG-Team' Sophie and Iege for a great working environment in the office and all the hours we spent together in the MRI as well as applying EEG electrodes! Thanks to Alex for all the great lunch discussions!

Lastly, I would like to thank my brother and my parents for always supporting me!

LMU LUDWIG-MAXIMILIANS-UNIVERSITÄT MÜNCHEN

Promotionsbüro
Medizinische Fakultät

MMRS

Eidesstattliche Versicherung

Mayr Astrid

Name, Vorname

Ich erkläre hiermit an Eides statt, dass ich die vorliegende Dissertation mit dem Titel:

Analysis of Pain Intensity Encoding in Chronic Pain Patients using Functional Magnetic Resonance Imaging

selbständig verfasst, mich außer der angegebenen keiner weiteren Hilfsmittel bedient und alle Erkenntnisse, die aus dem Schrifttum ganz oder annähernd übernommen sind, als solche kenntlich gemacht und nach ihrer Herkunft unter Bezeichnung der Fundstelle einzeln nachgewiesen habe.

Ich erkläre des Weiteren, dass die hier vorgelegte Dissertation nicht in gleicher oder in ähnlicher Form bei einer anderen Stelle zur Erlangung eines akademischen Grades eingereicht wurde.

München, 06.06.22

Ort, Datum

Astrid Mayr

Unterschrift Doktorandin bzw. Doktorand